ISSN : 2800-1729 **Edition : Vol 5. Num 1 (2026)**

Biopolymer Applications Journal

Editor in chief:
Pr. HAMMICHE Dalila

UNIVERSITÉ ABDERRAHMANE MIRA - BEJAIA
FACULTÉ DE TECHNOLOGIE

Table of content

Biopolymer Applications Journal ***Samia SLIMANI et al. Vol 5. N°1, 2026, pp. 01-08***
e-ISSN: 2800-1729

SILICONE INSULATION TILT ANGLE IMPACT ON ITS PERFORMANCE UNDER 1000 h OF SALT FOG AGING AND AC VOLTAGE

Samia SLIMANI[1*]; Wolfgang MANZKE[1]; Steffen VON DER AU[1]; Stefan KORNHUBER[2]; Abdallah MEDJDOUB[3]; Athmane BOUZIDI[3]
1: FGH Engineering & Test GmbH, Hallenweg 40 - 68219 Mannheim (Germany)
2: University of Applied Sciences Zittau/Görlitz, Theodor-Koerner-Allee 16, 02763, (Germany)
3: Laboratory of Electrical Engineering, University of Bejaia, 06000 Bejaia, Algeria
**Corresponding author email: samia.slimani@kema.com*
Received: 25 october 2025; Accepted: 24 December 2025; Published: 08 January 2026;

Abstract

The investigation focusses on the impact of the inclination angle with respect to the horizontal of hydrophobic elastomer silicone insulation on its performance during aging under salt fog and high AC voltage. The objective of this study is to quantify the leakage current along the surface of silicone insulation as a function of its inclination angle and duration of exposure to salt fog over 1000 hours ageing period. Upon completion of the ageing process, the silicone elastomer samples were characterized through surface roughness measurements, visual inspection of surface morphology, and evaluation of their hydrophobicity.
The results indicated that no burn marks or surface erosion was observed on the insulation after exposure to salt fog. Furthermore, the hydrophobic properties of silicone insulation were effectively retained over time under salt fog conditions, particularly at high inclinations. These findings suggest that increasing the tilt angle contributes to improving insulation performance during 1000 h of salt fog exposure.

Keywords: *Silicone insulation, Salt Fog, Inclination angle, Ageing, AC Voltage.*

I. Introduction

Over recent decades, polymeric insulators have become a preferred choice for outdoor insulation in electrical power distribution and transmission lines due to their excellent performance. Their lightweight nature, ease of handling and installation, along with their strong hydrophobic properties, make them highly advantageous compared to traditional insulating materials [1-3].
Under rain, fog or condensation, water droplets form on the surface of these insulators, due to their excellent hydrophobicity [4,5]. As a result, conductive contamination dissolved in water is discontinuous, leading to the limitation of leakage currents and the reduction of electrical discharges even under severe pollution conditions [6].
Despite their numerous advantages, the performance of polymeric insulators can be compromised under electrical stress due to the presence of water droplets on their surfaces. These droplets disturb the electric field distribution, promoting the initiation of surface discharges. Such discharges progressively degrade hydrophobicity, alter the surface morphology, and accelerate material deterioration. This effect is particularly pronounced when the water contains salt particles, as in salt fog conditions, which intensify erosion and ageing processes in silicone insulation materials [7-9].
The influence of salt spray on silicone insulators has attracted a great deal of attention from scientific researchers and industry experts. Investigations are focused on the study of insulator ageing and surface degradation, caused by circulation of leakage currents on their surfaces under the effect of accelerated aggressive atmospheric conditions such as simulated salt spray in the laboratory [10-13]. However, the effect of any shed's inclination of such insulators on their ageing under salt spray has not been sufficiently investigated and requires further research. This is one of the obvious reasons why we have analyzed this parameter in this paper.

This study presents a laboratory-based investigation into the impact of varying the inclination angle of hydrophobic silicone insulation surfaces on their performance under alternating current (AC) voltage in the presence of salt spray. The leakage current was monitored as a function of both the inclination angle with respect to the horizontal and the duration of exposure to the salt fog environment. Additionally, changes in the chemical and physical properties of the insulating surfaces such as erosion, hydrophobicity loss, and surface roughness were systematically analyzed. The findings provide valuable insights into the operational behavior of silicone insulators and offer an experimental foundation for the design and selection of robust, high-performance outdoor insulation systems.

II. Material and methods

II. 1 Sample preparation and experimental set-up

Silicone elastomer samples (POWERSIL XLR 600 A/B) were used in this investigation. For each inclination angle (0°, 30°, 45°, 90°) of the insulation with respect to the horizontal, the analysis was carried out on 4 flat specimens (S_1, S_2, S_3, S_4) of dimensions (10 * 5 * 0.6) cm^3 (Figure. 1). This type of material was chosen for its resistance to ageing, UV rays and chemicals, making it suitable for use in harsh environments conditions. POWERSIL XLR 600 also has excellent hydrophobic properties, and its static contact angle with a 5 µl drop of water measured in the laboratory using a goniometer is equal to 110°.

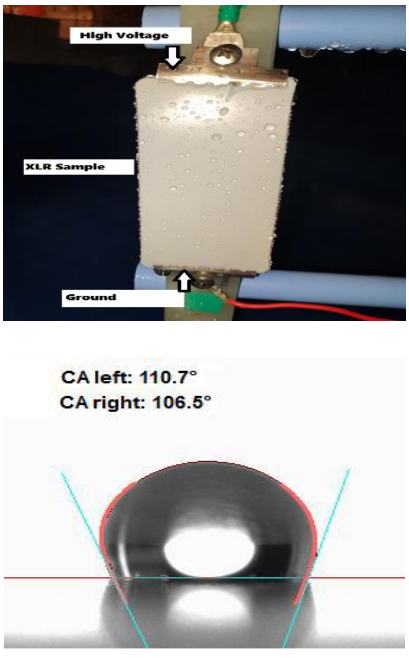

Figure 1. XLR600 sample attached to a device inclined at 90° with respect to the horizontal

Samples are attached to a device that allows the variation of the tilt angle from 0° to 90° (Figure 1). It is made of metal and tinted with several layers of insulating tint to prevent corrosion that could be caused by contact with the saline solution. This device is placed in the middle of the fog chamber. For each tilt angle α (0°, 30°, 45°, 90°), the insulation is exposed to salt spray for a period of up to 1000 h.

II. 2 Salt solution

The electrical conductivity of the sprayed contaminant solution was 1.78 mS/cm. It is obtained by adding a quantity of Magnesium Nitrate (Mg (NO3)2) to a volume of tap water with a concentration of 1Kg/m^3 (1g/L) according to the standard: IEC 62217.

II. 3 Fog chamber and leakage current measurement

The fog chamber is 1.6 m * 1.6 m * 2.5 m in size. Its walls are made of PVC, transparent and allow visual inspection of the samples tested inside. The chamber is equipped with a plexiglass door, allowing access to its interior when not in operation for sample installation or removal, system adjustments, and post-analysis cleaning. Two type D 505 atomizers (Defensor AG, Pfäffikon, CH) are installed in opposite corners of the chamber to ensure a uniform distribution of salt fog. The atomizers are regulated to maintain the precipitation rate specified in Table 2 of IEC 62217, with a spray rate set at 1.5 ± 0.5 ml/h.

Figure 2. Fog chamber

The insulation was subjected to 1 kV AC voltage and exposed to salt spray for a maximal period of 1000 h. The maximum leakage current that can flow and short-circuit the samples surface should not exceed the leakage current threshold set at 2 mA for 2 seconds. Beyond this value, the voltage switches off automatically. These leakage currents are measured during the entire analysis period using NextView®4 software. The results of the leakage current measurements collected are of order of 176,000 values for each hour of testing, over the period of exposure to the salt fog.

II. 4 Hydrophobicity measurement

The hydrophobicity of our samples is determined and measured using the static contact angle method. This method involves measuring the static contact angle of a 5 µl drop of water deposited on the insulation surface before and after exposure to salt spray, using an optical contact angle measurement and contour analysis system OCA35 (Goniometer), in accordance with DIN IEC/TS62073, VDE 0674-276.

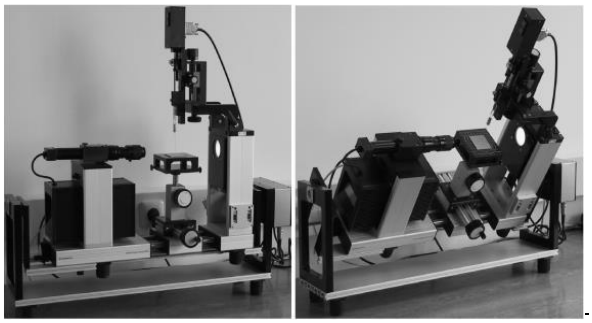

Figure 3. Hydrophobicity measurement with Goniometer

Five measurement points at different locations along the insulating surface are taken for each sample. The value considered at the end is the calculated arithmetic mean of these 5 static contact angle values for each sample.

II. 5 Roughness measurement

Roughness measurement of our samples before and after exposure to salt spray under AC voltage is carried out according to the norm ISO 4287, using a numeric microscope. After cleaning and conditioning the samples at a temperature of (23±2) ° and a humidity of (45 ± 5) %, they are immediately examined under the microscope, and the value of the Average surface roughness (Ra) is directly indicated and given.
Five measurements in different areas of the sample surface were taken to obtain a representative average of surface roughness.

III. Results and discussion

III.1 Visual inspection of samples after ageing

At the end of the ageing process, the samples removed from the fog chamber were subjected to a visual inspection to study the condition of their surfaces after exposure to salt spray for up to 1000 hrs. This inspection revealed no erosion, burns or cracks on any of the insulating surfaces. A slight discoloration of the samples was noted, which is usual for polymer insulators after ageing [14,15], this is caused by several mechanisms such as oxidation, chemical reactions and migration of the pigments responsible for material coloration. This is attributed to the effect of moisture and salts present in the salt fog, which penetrates the material's structure and promotes oxidation and undesirable chemical reactions. These reactions may lead to the breakdown of chemical bonds and alterations in the material's structure. Furthermore, high humidity and reactive salts can interact with the functional groups of the material, forming chemical compounds that may dissolve or modify the pigment particles.

III.2 Morphology and surface roughness

The performance of an insulation is strongly influenced by its surface morphology [16]. Ageing of silicone insulation under salt spray and AC voltage can lead to surface roughness. This can be caused by the formation of microcracks and pores, which can accumulate pollutants and salts from the environment. This leads to the formation of a thin conductive layer and the appearance of electrical discharges on the insulating surface.
Figure 4 shows the evolution of surface roughness samples S_1, S_2, S_3 and S_4 for each inclination angle α (0°, 30°, 45°, 90°), after ageing in a salt spray and AC voltage environment. This shows that all aged samples present a slight increase in surface roughness compared to a virgin sample (S_{virg}), regardless of their inclination. This small increase is due to the low voltage applied to the samples as roughness increases with the rise in applied voltage [17] and as the voltage applied in this study did not exceed 1 kV only a small increase in roughness was observed.

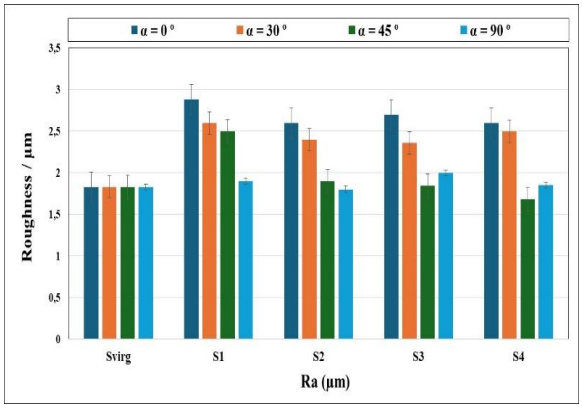

Figure 4. Surface roughness of inclined samples at different inclination angles

Although surface roughness is not directly related to the inclination angle, the variation in α has a significant impact on surface wettability. A low inclination angle leads to high surface wetting, which increases the frequency of occurrence and circulation of electrical discharges. This leads to the appearance of cracks and an increase in surface roughness and the opposite was observed for a high inclination (Figure 5).
The 2D images presented in Figure 5 were captured using a microscope on the surfaces of the samples after ageing, at various inclination angles α. To better visualize the morphology and appearance of the samples, the ImageJ software was used to generate 3D representations from these 2D images. This method is reliable for qualitative and comparative analysis of surface morphology. It can serve as a useful preliminary or complementary tool for more advanced techniques.
Figure 5 shows that, even when exposed to salt spray for a long period (1000 h), the insulation in the vertical

position was able to resist ageing without significantly affecting its roughness. On the other hand, when the insulation is in the horizontal position (α = 0°), its surface becomes rougher due to the formation of salt deposits which can create asperities on these surfaces and accelerate the degradation of the insulation, resulting in their flashover after a short period of exposure to salt spray (maximum 192 h) and thus reducing its electrical performance and operating life.

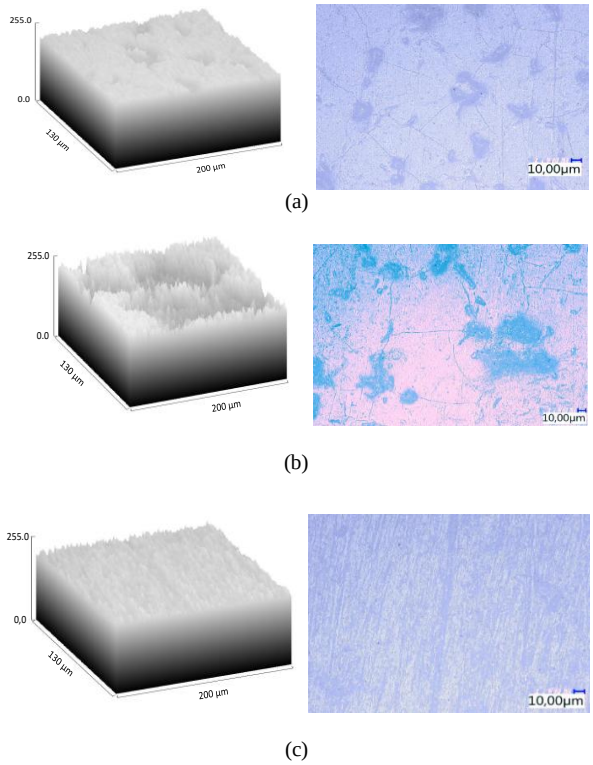

Figure 5. Surface morphology before and after ageing, represented by a 2D image captured with a microscope (left) and a 3D generated using ImageJ (right), (a): Virgin sample, (b): α = 0°, (c): α = 90

III.3 Hydrophobicity of aged insulation

Figure 6 shows a comparison of the static contact angle measured on sample surface before and after ageing when it is tilted at 90° and subjected to alternating voltage.

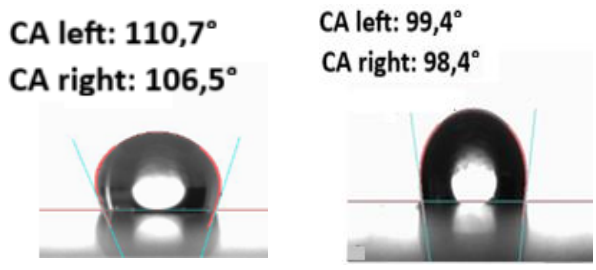

Figure 6. Static contact angle before and after insulation exposure to salt spray, α = 90°

Figures 7, 8, 9 and 10 illustrate the different static contact angles of the sample surfaces before and after exposure to salt fog, corresponding to inclination angles α of 0°, 30°, 45° and 90º, respectively. A decrease in static contact angle was observed on all samples regardless of their inclination relative to the horizontal, as should also be noted that the exposure time (T_{exp}) to the salt fog is limited by the deactivation criterion (threshold current) and it differs from one sample to another.

This drop in contact angle measured after ageing is mainly due to electrical discharges occurring on the insulating surface of the sample in the presence of moisture when subjected to alternating voltage during ageing in a salt fog environment [18]. These electrical discharges release a large amount of energy, which can break the chemical bonds within the polymer molecules. This leads to a reduction in hydrophobic groups and an increase in the precipitation of hydrophilic groups due to salts cementing the surface of the insulator. As a result, the static contact angle decreases [19], which may increase the electrical conductivity of the insulator and consequently reduce its flashover voltage.

It can be seen from figures 8 and 9 that the insulating surfaces inclined at 30° and 45° reached a nearly similar reduction in hydrophobicity, despite being exposed to the salt fog for different durations. The samples inclined at 45° were subjected to a slightly longer exposure period than those at 30°, indicating that the dielectric performance of the insulation at 45° is comparable to that at α = 30°.

According to figure 7, sample S_1 was removed from the salt fog chamber after only a few hours of exposure. This was due to leakage currents exceeding the predetermined threshold, caused by the degradation of the surface hydrophobicity. This degradation continued the other samples and became increasingly significant as the ageing duration increased. The highest dielectric strength was observed in sample S_4, which maintained its electrical insulation properties for an exposure period to the salt fog not exceeding 192 hours. This can be explained by the fact that, in the horizontal position of the insulation, the samples become more humid due to the accumulation and coalescence of water droplets on their surfaces. This promotes the occurrence of many successive and repeated electrical discharges over a short period of time. These discharges, along with leakage currents, accelerate ageing of sample surfaces, leading to a rapid degradation of their hydrophobic properties, failure of samples, and a reduction in their service life.

As shown in Figure 10, the static contact angle measured for S_1, S_2, S_3, et S_4 was in the range of 92 to 98.The highest measured static contact angles compared to others inclined samples with α = 0º, 30º and 45º.This indicates that, despite the hydrophobicity

reduction after 1000 hours of ageing, the samples in vertical position still retained their hydrophobic properties.

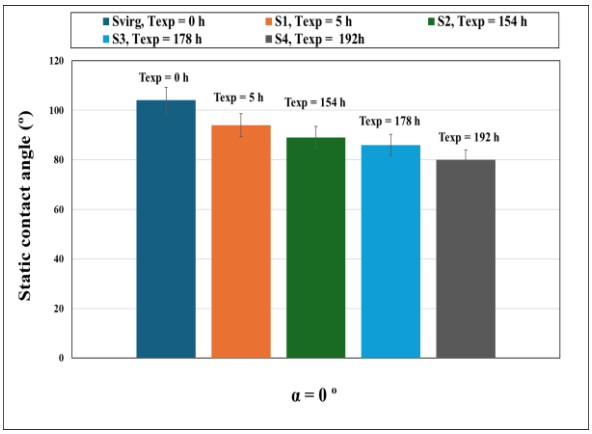

Figure 7. Static contact angle after exposure of insulation to salt fog, α = 0°

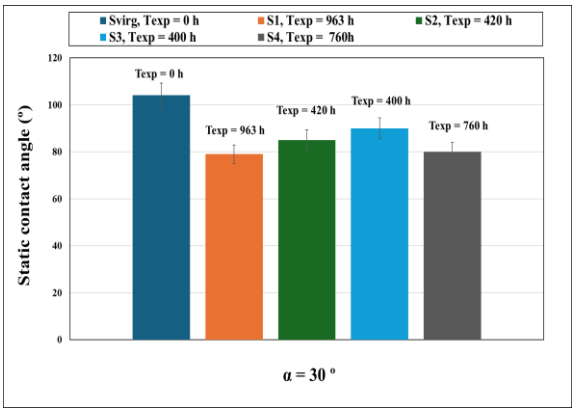

Figure 8. Static contact angle after exposure of insulation to salt fog, α = 30°

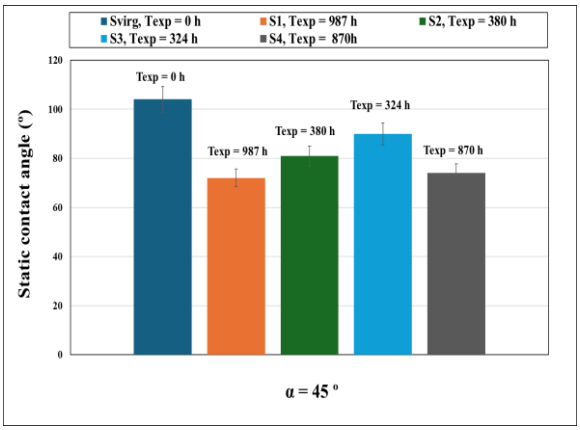

Figure 9. Static contact angle after exposure of insulation to salt fog, α = 45°

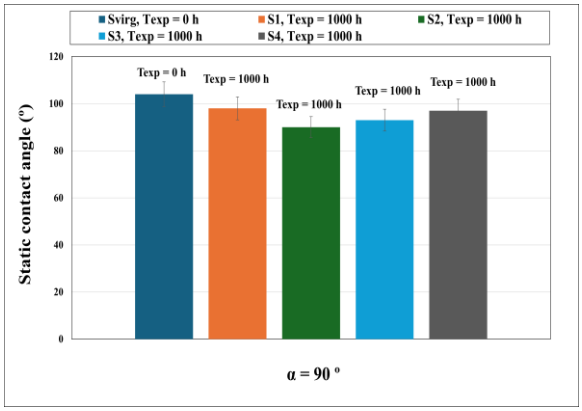

Figure 10. Static contact angle after exposure of insulation to salt fog, α = 90°

III.4 Leakage current flowing on insulating surfaces

The leakage current flowing along the surface of the samples was measured to investigate their ageing behavior as a function of exposure time to salt spray under AC voltage.

These measurements were performed on all samples; each fixed at different inclination angles α ranging from 0° to 90°. For every inclination angle, four samples (S_1, S_2, S_3, and S_4) were tested throughout the salt spray ageing period.

For each sample, highly precise measurements of the maximum leakage current (I_{max}) and minimum leakage current (I_{min}) were taken every 0.02 seconds and recorded every 15 minutes throughout the entire ageing period.

The corresponding results are presented in figures 11, 12, 13, and 14.

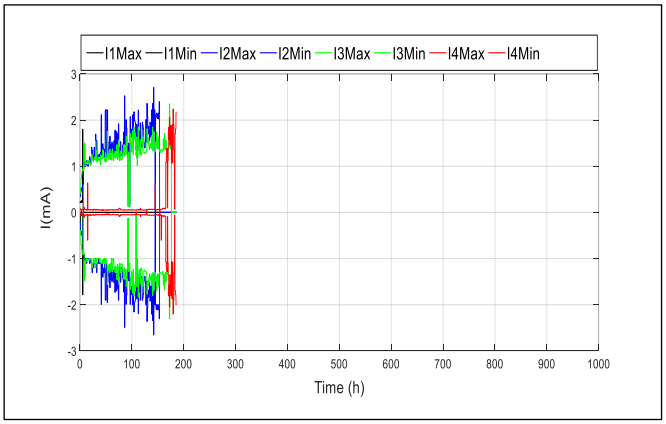

Figure 11. Leakage current flowing on S_1, S_2, S_3, S_4, α = 0° for 190 h

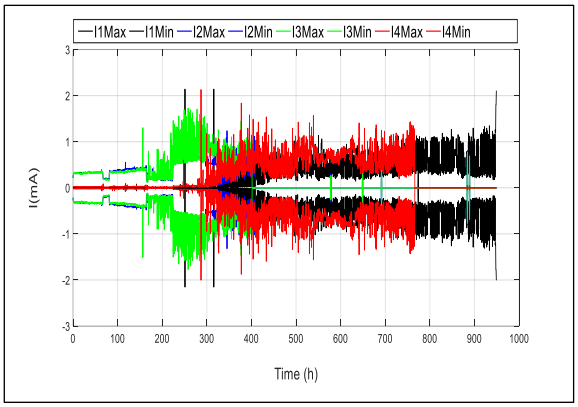

Figure 12. Leakage current flowing on S_1, S_2, S_3, S_4, α = 30° for 963 h

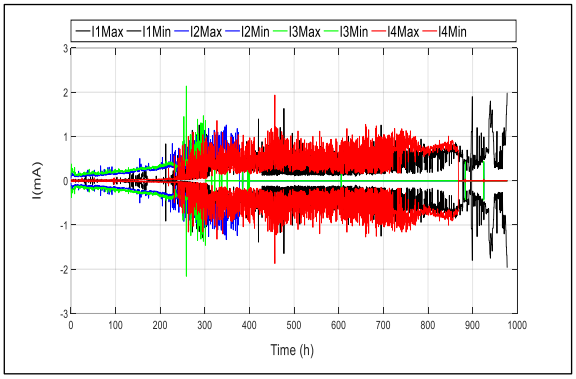

Figure 13. Leakage current flowing on S_1, S_2, S_3, S_4, α = 45° for 987 h

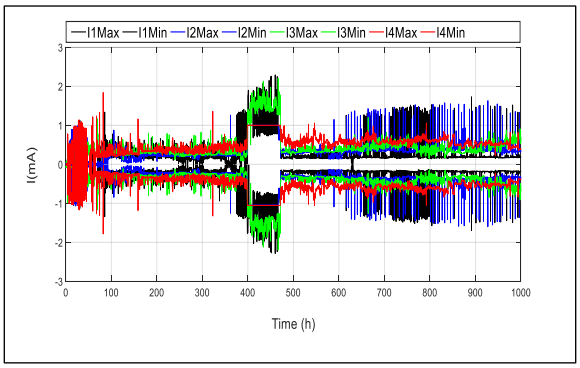

Figure 14. Leakage current flowing on S_1, S_2, S_3, S_4, α=90° for 1000 h

The results indicate that all samples exhibit a progressive increase in leakage current with increasing exposure time to the salt spray environment under AC voltage. Once the leakage current reaches the threshold value of 2 mA sustained for 2 seconds, the sample is considered to have failed and is consequently withdrawn from service. The time required to reach this critical value varies depending on the inclination angle of the sample. For the horizontally positioned sample, failure occurs after only 192 hours of exposure. This duration increases to 963 and 987 hours for inclination angles between 30° and 45° and exceeds 1000 hours for samples inclined at 90°.

The leakage current curves illustrated in figures 11, 12, 13, and 14 can be divided into three distinct regions [20]. The first region, referred to as the *early ageing period*, corresponds to the initial phase of testing. It is characterized by a slow and gradual increase in leakage current, indicating progressive sample degradation while maintaining surface hydrophobicity. During this phase, the leakage current waveform usually shows periodic discharge patterns. As the exposure time to the salt spray environment increases, the leakage current may reach a stable value, suggesting a temporary stabilization of the degradation process.

The second region is marked by a significant rise in leakage current, indicating the onset of hydrophobicity loss and advanced material degradation. This leads to the coalescence of water droplets on the sample surface. At this stage, the leakage current waveform displays increasingly frequent peaks and impulse discharges. This region represents the *transitional ageing period*.
In the third region, known as the *late ageing period*, the leakage current becomes substantially higher and increases rapidly until it reaches or exceeds the predefined threshold level. Water droplets adhere more strongly to the sample surface due to severe degradation and complete loss of hydrophobicity, forming a continuous conductive path between electrodes. This results in the formation of a thin moisture layer on the surface. Under the influence of Joule heating caused by the leakage current, this moisture layer evaporates, leading to the formation of dry bands and continuous surface discharges. These phenomena can ultimately result in complete sample failure [21].

It should be noted that the duration of the initial ageing period differs from one sample (S_1, S_2, S_3, S_4) to another for the same inclination and from one insulation to another depending on its inclination angle α (0°, 30°, 45°, 90°).
The longest initial ageing period, around 340 hrs was recorded when the insulation was in a vertical position. However, the shortest one (4 hrs) was recorded when the insulation was in a horizontal position.
The initial ageing period duration of polymeric insulators under salt fog conditions is a key indicator of their erosion resistance and ability to maintain electrical performance.

An extended duration of the initial ageing period observed in leakage current curves indicates superior insulation quality and enhanced resistance to erosion. Samples positioned vertically (α = 90°) show the longest duration of this phase, reflecting greater ageing

resistance and reliability. As the inclination angle decreases, this duration shortens, suggesting decreased performance and increased susceptibility to environmental stress.

IV. Conclusion

The investigation of the impact of a silicone insulation tilt angle on its performance when subjected to combined ageing under salt fog and alternating voltage led to the following key points:

- A decrease in the hydrophobicity of silicone insulation was observed as a function of its inclination angle with respect to the horizontal and its exposure duration to the salt fog environment.
- The results of surface roughness measurements performed on the samples before and after ageing indicate a slight increase in roughness across all surfaces, which increases as its angle of inclination α increases.
- A progressive increase in leakage current was recorded for all samples as exposure time to the salt fog increased, eventually reaching a threshold value that led to their deactivation.
- The time required to reach the leakage current threshold varies from one sample to another, depending on its inclination angle with respect to the horizontal.
- The development of leakage current occurs in three distinct periods: the early aging period, the transition period, and the late aging period.
- A leakage current curve characterized by an extended early ageing period indicates good insulation quality. However, a short early ageing period suggests poor insulation quality and low resistance to erosion.

Acknowledgment

The authors would like to express their deepest gratitude to all the members of the HV laboratory Zittau, Germany and the authors are also extremely grateful to the members of the laboratory of HV in Bejaia, Algeria

References:

1. Nan, J.; Li, H.; Wan, X.; Huo, F.; Lin, F. "Pollution Flashover Characteristics of Composite Crossarm Insulator with a Large Diameter". Energies, 14, 20, 2021.

2. Qiao, X.; Zhang, Z.; Sundararajan, R.; Jiang, X.; Hu, J.; Fang, Z. "AC Breakdown Characteristics of Polluted 10-kV Post Insulator with Concentric Externally Gapped Line Arrester". IEEE Trans. Power Deliv. 37, 59–66, 2022.

3.Zhao, X.; Yang, X.; Hu, J.; Wang, H.; Yang, H.; Li, Q.; He, J.; Xu, Z.; Li, X. "Grading of electric field distribution of AC polymeric outdoor insulators using field grading material". IEEE Trans. Dielectr. Electr. Insul. 26, 1253–1260 ,2019.

4. A. Ren, H. Liu, J. Wei and Q. Li, "Natural Contamination and Surface Flashover on Silicone Rubber Surface under Haze-Fog Environment", Energies, 10, 1580, pp. 1-18, 2017.

5.T. Sakoda, K. Tabira, T. Miyake, N. Hayashi, K. Haji,Y. Aka, T. Anjiki, T. Fukano, "Discharge behavior and dielectric performance of artificially polluted hydrophobic silicone rubber", Journal of Electrostatics 93, pp. 97–103, 2018.

6. S. Slimani, A. Medjdoub, S. Kornhuber "Humidification Degree Effect under Rain of Inclined Silicone Insulation on its Electric Performance" Periodica Polytechnica Electrical Engineering and Computer Science, 68(1), pp. 94–106, 2024.

7.T. Belhoul, R. Boudissa, K.D. Haim, "Comparison of the Performance of Silicone and Glass Barriers under Direct Current and Very Severe Conditions of Pollution", IEEE Transactions on Dielectrics and Electrical Insulation, Vol. 24, Issue n° 1, pp. 471-482, 2017.

8. IEC-TS 62073, "Guidance on the measurement of hydrophobicity of insulator surfaces", 2016.

9. IEC 62631-2-1:, "Dielectric and resistive properties of solid insulating materials - Part 2-1: Relative permittivity-Technical Frequencies (0,1 Hz - 10 MHz) - AC Methods". 2018.

10. Chen, L.; Guo, F.; Yang, T.; Hu, T.; Bennett, P.; Yang, Q.; Liu, D. "Aging characteristics and self-healing properties of laser-textured superhydrophobic silicone rubber for composite insulators". Polym. Degrad. Stab., 192, 109693,2021.

11. Jiao, J.; Li, L.; Wu, B.; He, C. "Novel capacitive proximity sensors for assessing the aging of composite insulators". Sens. Actuators A 253, 75–84,2017.

12. Homma, T.; Kumada, A.; Fujii, T; Oishi, Y. "Depth profiling of surface degradation of silicone rubber composite insulators by remote laser-induced breakdown spectroscopy". Spectrochim. Acta Part B 180, 106206,2021,.

13. Francis, U.U.; Philip, A.N. "Degradation of epoxy reinforced Banana fibers and eggshell particles hybrid composite high-voltage

insulators via accelerated UV aging processes". Chem. Data Collect., 38, 100842, 2022.

14.C. Baer, R. Bärsch, A. Hergert, J. Kindersberger,''Evaluation of the Retention and Recovery of the hydrophobicity of Insulating Materials in High Voltage Outdoor Applications under AC and DC Stresses with the Dynamic Drop Test", IEEE Transactions on Dielectrics and Electrical Insulation, Vol. 23, Issue n° 1, pp. 294-303, 2015.

15. T. Tanaka, "Aging of polymeric and composite insulating materials. Aspects of interfacial performance in aging," IEEE Transactions on Dielectrics and Electrical Insulation, vol. 9, pp. 704-716, 2002.

16. D. A. Swift, C. Spellman and A. Haddad, ''Hydrophobicity Transfer from Silicone Rubber to Adhering Pollutants and its Effect on Insulator Performance", IEEE Transaction on Dielectrics and Electrical Insulation, Vol. 13, No. 4, pp. 820-829, 2006.

17. D. Ghosh, D. Khastgir,"Degradation and Stability of Polymeric High-Voltage Insulators and Prediction of Their Service Life through Environmental and Accelerated Aging Processes", ACS Omega 2018, 3, 11317−11330 DOI: 10.1021/acsomega.8b01560 ACS Omega, 3, 11317−1133011319, 2018.

18.Zhijin, Z.; Tian, L.; Xingliang, J.; Chen, L.; Shenghuan, Y.; Yi, Z. "Characterization of Silicone Rubber Degradation Under Salt-Fog Environment with AC Test Voltage". IEEE Access 7, 66714–66724, 2019.

19.A. Tuteja, W. Choi, J. M. Mabry, G. H. McKinley, and R. E. Cohen, "Robust omniphobic surfaces," Proceedings of the National Academy of Sciences, vol. 105, no. 47, pp. 18200-18205, 2008.

20.A. H. El-Hag, A. N. Jahromi, M. Sanaye-Pasand," Prediction of leakage current of non-ceramic insulators in early aging period", Electric Power Systems Research 78, 1686–1692, 2008.

21.Y. Kurimoto, Y. Tashiro, Y. Murakami, H. Homma and M. Nagao, 'Variation of Leakage Current Caused by Hydrophobicity Loss of Silicone Rubber in Dynamic Drop Test', Proceedings of 2008 International Symposium on Electrical Insulating Materials, September 7-11, 2008, Yokkaichi, Mie, Japan.

Biopolymer Applications Journal **Vikram Uttam Pandit**. ***Vol 5. N°1, 2026, pp. 09-16***
e-ISSN : 2800-1729

Advances in Polymer Nanocomposites for Efficient Photocatalytic Dye Degradation: Synthesis, Mechanisms, and Environmental Applications

Vikram Uttam Pandit*
Department of Chemistry, Haribhai V. Desai College of Arts, Science and Commerce (Autonomous), Pune-411002, Maharashtra, India
Corresponding author: vikramupandit@gmial.com, vikram.pandit@hvdesaicollege.edu.in*
Received: 04 November 2025; Accepted: 21 December 2025; Published: 12 January 2026

Abstract

The discharge of synthetic dyes from various industrial activities poses a severe environmental threat due to their high stability, toxicity, and resistance to biodegradation. Polymer nanocomposites, which integrate functional polymers with semiconductor nanoparticles, have emerged as promising materials for the photocatalytic degradation of organic dyes under ultraviolet and visible light irradiation. This review comprehensively examines recent progress in the development of polymer nanocomposite photocatalysts, focusing on their synthesis methodologies, structural attributes, and underlying degradation mechanisms. The synergistic interactions within these hybrid systems facilitate improved charge separation, extended light absorption, and enhanced dye adsorption, leading to superior photocatalytic performance. Various classes of polymer nanocomposites, including polymer–metal oxide, conducting polymer-based, biopolymer-based, and hybrid composites, are discussed with respect to their functional roles in dye degradation and wastewater remediation. Furthermore, the review addresses recyclability, long-term stability, and practical applicability in real effluent systems. Future perspectives emphasize the advancement of green, biodegradable, and multifunctional polymer nanocomposites with enhanced durability, scalability, and environmental compatibility for sustainable wastewater treatment processes.
Keywords: *Polymer nanocomposites, dye removal, polymer-metal conducting polymers, wastewater treatment, biodegradable polymers*

I. Introduction

Water pollution caused by the discharge of synthetic dyes from various industrial sectors such as textiles, leather, paper, and pharmaceuticals has become a serious environmental concern worldwide [1–3]. Dyes constitute one of the largest groups of pollutants due to their complex aromatic structures, which resist degradation and persist in aquatic environments, causing toxicity to aquatic life and health hazards to humans [4–5]. The presence of colored effluents also decreases light penetration in water bodies, adversely impacting photosynthetic organisms and disrupting aquatic ecosystems [6–8]. Conventional dye removal techniques, including coagulation, sedimentation, adsorption on activated carbon, and chemical oxidation, have limitations such as incomplete degradation, generation of secondary pollutants, high operating costs, and sludge disposal issues [9–11]. Therefore, there is a pressing need to develop efficient, cost-effective, and sustainable methods to treat dye-contaminated wastewater [12–13].

Photocatalytic degradation, an environmentally benign approach, utilizes semiconductor materials to harness light energy to generate reactive oxygen species (ROS) capable of breaking down complex dye molecules into harmless mineral end-products like CO_2 and H_2 O. However, pure semiconductor photocatalysts often suffer from rapid recombination of photogenerated electron-hole pairs, limited visible light absorption, and agglomeration, which restrict their practical applications [15–16]. To overcome these challenges, polymer nanocomposites combining functional polymers with photocatalytic nanoparticles have garnered significant attention in recent years [17–20]. The polymer matrix enhances the dispersibility and stability of nanoparticles, provides adsorption sites for dye molecules, and facilitates efficient charge separation, reducing recombination losses as shown in figure 1 [21–25].

Moreover, conducting polymers like polyaniline and polypyrrole can extend light absorption into the visible region and act as electron mediators to boost photocatalytic activity [26–33].

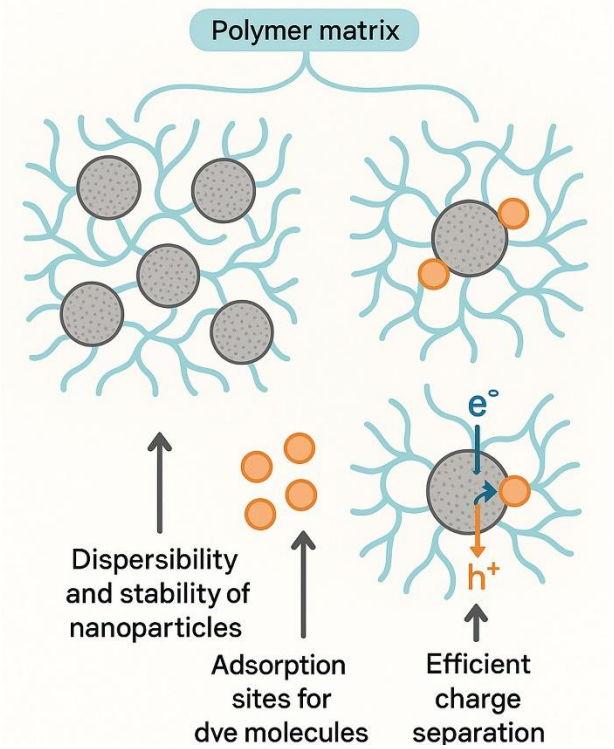

Figure 1: Photocatalytic mechanism of polymer matrix

This mini review focuses on polymer nanocomposites engineered for the degradation of organic dyes in wastewater. It discusses the types of polymer nanocomposites, synthesis strategies, degradation mechanisms involving ROS, and recent advancements demonstrating enhanced performance under visible or UV light. The review further highlights practical applications, recyclability, and the challenges faced in scaling up these nanocomposites for real-world wastewater treatment. Finally, it outlines future research directions to develop green and multifunctional polymer nanocomposite photocatalysts for sustainable environmental remediation.

Types of Polymer Nanocomposites

Polymer-metal oxide nanocomposites are the most widely studied nanocomposites, where semiconductor metal oxide nanoparticles, such as TiO2, ZnO, Fe3O4, NiO, are embedded within or coated by polymer matrices [34–36]. The polymers used include conducting polymers like polyaniline (PANI), polypyrrole (PPy), and other synthetic or natural polymers like chitosan and polyethylene glycol [37–40]. Key features include enhanced charge separation due to polymer interaction that reduces electron-hole recombination and improved adsorption of dye molecules on the polymer surface [41–42]. TiO2-based nanocomposites modified with graphene, graphene oxide, or metal doping show improved visible light absorption and photocatalytic efficiency [43–45]. Conducting polymer nanocomposites consist of conducting polymers such as polyaniline, polypyrrole, or polythiophene combined with nanoparticles or other nanomaterials. They are known for their π-conjugated system allowing good electronic conductivity and light absorption properties, leading to effective electron donor-acceptor processes in photocatalysis [47–48]. Notably, composites like ZnO2/polypyrrole uniquely degrade dyes both under light and in the dark by generating reactive oxygen species without additional reagents relying on synergistic physiochemical properties [49–50]. Biopolymer-based nanocomposites are natural polymers like chitosan, sodium alginate, or cellulose combined with metal oxide nanoparticles are gaining attention due to their biodegradability, biocompatibility, and environmental friendliness [51–53]. These biopolymers provide abundant functional groups for dye adsorption and can encapsulate nanoparticles to prevent aggregation, thereby improving photocatalytic stability and reusability [54–55]. Hybrid and multi-component nanocomposites involves combining more than two components, such as polymers with mixed metal oxides or doped nanoparticles. Hybrid nanocomposites are engineered to broaden light absorption range, increase active sites, and enhance photocatalytic efficiency through multi-functional synergistic effects [57–59]. For example, polymeric composites incorporating nanosheets (like hexagonal boron nitride), graphene derivatives, or noble metal nanoparticles (Au, Ag) in combination with metal oxides have shown superior dye degradation performance [60–61]. Magnetic polymer nanocomposites are loaded with magnetic nanoparticles (e.g., Fe3O4) not only exhibit photocatalytic properties but also enable facile magnetic recovery and recyclability, making them attractive for practical wastewater treatment processes [62–63].

Synthesis and Mechanisms of Polymer Nanocomposites for Dye Degradation

Polymer nanocomposites for photocatalytic dye degradation are synthesized using various methods that combine polymers with nanoparticles to enhance surface properties, stability, and photocatalytic efficiency [64].

Chemical Polymerization: Polymers like polyaniline (PANI) or polypyrrole (PPy) are chemically polymerized in the presence of nanoparticles such as TiO2, ZnO, or Fe3O4. This approach provides good control over polymer-nanoparticle interactions and particle dispersion. [65-66]

Sol-Gel Method: Involves hydrolysis and condensation of metal alkoxides to form metal oxide nanoparticles embedded in polymer matrices. This mild synthesis enables excellent homogeneity and nano-scale dispersion. [67-70]

Hydrothermal and Solvothermal Synthesis: High temperature and pressure conditions favor crystalline nanoparticle growth within polymers. This technique often produces nanocomposites with enhanced crystallinity and photocatalytic activity. [71]

In Situ Polymerization: Polymers are formed in the presence of nanoparticles, leading to strong interfacial bonding and stable composites that help prevent nanoparticle aggregation. [72]

Solution Casting and Sonication: Nanoparticles are dispersed in polymer solutions by sonication and then cast into films or powders, allowing for easy scale-up preparation.

These methods produce nanocomposites with distinct morphologies and porosities that influence their photocatalytic performance. Functionalization of polymer matrices offers additional adsorption sites for dye molecules and improves catalyst stability [73].

Photocatalysis in polymer nanocomposites involves the activation of semiconductor nanoparticles by light with energy equal or higher than their band gap, generating electron-hole pairs. Key steps include:
Photoexcitation: Absorption of UV or visible light excites electrons from the valence band to the conduction band of the semiconductor, creating holes in the valence band. [74]
Charge Separation: Polymers assist in separating and transporting these charge carriers, reducing electron-hole recombination. Conducting polymers can act as electron donors or acceptors, enhancing charge mobility. [74-75]
Generation of Reactive Oxygen Species (ROS): Electrons reduce adsorbed oxygen molecules to superoxide radicals ($O_2^{(\cdot-)}$), while holes oxidize water or hydroxyl ions forming hydroxyl radicals (-OH), both of which are strong oxidizers responsible for degrading dye molecules. [76]
Adsorption and Degradation: The polymer matrix adsorbs dye molecules near active sites, where ROS attack the dye's chromophoric groups inducing molecular breakdown into non-toxic end products such as CO2 and H2O. Effect of Parameters: Factors like pH, catalyst loading, light intensity, and dye concentration significantly affect degradation rates. The nanocomposite morphology also influences light absorption and active site availability [77]. Overall, polymer nanocomposites improve photocatalytic efficiency by integrating adsorption, light harvesting, and charge transfer functionalities, making them excellent candidates for environmental remediation applications [78].
Performance and Applications:
Polymer nanocomposites have demonstrated remarkable performance in photocatalytic degradation of various organic dyes, showcasing their potential as effective materials for wastewater treatment. The synergy between polymer matrices and semiconductor nanoparticles facilitates enhanced photocatalytic activity, compared to pure components.
Photocatalytic Efficiency:
Nanocomposites such as chitosan-ZnO/Fe3O4 have achieved degradation efficiencies above 99% for methyl orange and over 90% for rhodamine B under visible light irradiation. The narrow bandgap (~2.8 eV) and porous nanostructure enable greater light absorption and dye access to active sites. TiO2-based polymer composites exhibit improved photocatalytic degradation through reduced electron-hole pair recombination facilitated by conducting polymers or doped materials. Some nanocomposites can degrade dyes like rhodamine B and methylene blue even in dark conditions via advanced oxidation processes, demonstrating versatile catalytic capabilities beyond light activation. [79-82]
Stability and Reusability:
These nanocomposites generally maintain high photocatalytic activity over multiple cycles, with slight decreases in efficiency attributed to catalyst surface fouling or loss during recovery. Magnetic nanocomposites such as Fe3O4-containing polymers offer easy recovery and reuse through magnetic separation, enhancing practical utility for wastewater treatment. [83]
Influencing Parameters:
pH plays a crucial role, with neutral or slightly basic conditions often favored for maximum degradation. Catalyst dose, initial dye concentration, and irradiation time directly affect degradation kinetics, often following Langmuir–Hinshelwood isotherm and pseudo-first order kinetics. Electrostatic interactions, hydrogen bonding between dye molecules and functional polymer groups improve adsorption and degradation rates. [84]
Applications:
Effective treatment of textile industry effluents containing azo dyes, methylene blue, rhodamine B, and other harmful dyes. Potential integration into advanced oxidation processes and membrane filtration for comprehensive wastewater remediation. Antibacterial properties of certain polymer nanocomposites add an advantage for treating biologically contaminated water. [85-86]
Challenges and Limitations:
Despite promising photocatalytic performance, polymer nanocomposites for dye degradation face several challenges and limitations that restrict their broader application.
Photodegradation and Structural Stability: Polymer components may undergo photodegradation under prolonged light exposure, leading to a loss of structural integrity and reduced ability to facilitate efficient charge transfer. Photocorrosion of semiconductor nanoparticles can also deteriorate catalyst stability and lifespan. [87-94] Nanoparticle Aggregation and Dispersion: Achieving homogeneous dispersion of nanoparticles within polymer matrices remains difficult. Aggregation of nanoparticles reduces available active sites and surface area, thereby decreasing photocatalytic efficiency. Limited Visible Light Absorption: Many polymer-metal oxide nanocomposites primarily absorb UV light due to wide bandgap semiconductors like TiO2, limiting solar light utilization. Strategies to extend absorption to the visible range, such as metal doping or polymer functionalization, add complexity to synthesis. [95] Recyclability and Catalyst Recovery: While magnetic polymer nanocomposites aid recovery, many nanocomposites face challenges in catalyst separation after treatment, impacting reusability. Loss of catalyst mass and activity over multiple cycles is commonly observed. Scalability and Practical Implementation: Difficulties in large-scale synthesis that maintain reproducibility and controlled properties limit commercialization. Stability in complex real wastewater matrices, which contain multiple pollutants and variable pH, remains insufficiently explored. [96-99]
Environmental and Health Concerns: Potential toxicity of free nanoparticles or degradation by-products must be carefully evaluated. Sustainable and green synthesis routes for polymer nanocomposites are still under development to reduce environmental footprint. Addressing these challenges through advanced material design, green chemistry approaches, and pilot-scale studies is critical for realizing the practical deployment of polymer nanocomposite technologies in wastewater treatment [100-115].

II. Conclusions

Polymer nanocomposites have demonstrated significant potential as efficient, stable, and versatile photocatalysts for

the degradation of synthetic dyes in contaminated water systems. Their hybrid structures provide a unique combination of adsorption capacity, photoactivity, and charge-transfer efficiency, enabling effective mineralization of complex organic pollutants. Incorporation of conducting and biopolymeric components has further enhanced visible light utilization, photostability, and reusability, underscoring their superiority over conventional semiconductor photocatalysts. Nevertheless, persistent challenges such as nanoparticle agglomeration, photodegradation of polymer matrices, limited visible light absorption, and scalability constraints must be addressed to facilitate real-world application. Future research should prioritize the rational design of biodegradable, magnetically recoverable, and structurally robust nanocomposites, along with the adoption of environmentally benign synthesis approaches. Advanced hybrid architectures utilizing doped semiconductors, conductive polymers, and biopolymer supports are expected to accelerate the transition of these materials from laboratory-scale studies to practical wastewater treatment technologies, contributing substantially to sustainable environmental remediation.

A. Acknowledgment*:*
Dr. Vikram Uttam Pandit would like to take this opportunity to dedicate this work to Professor Dr. Shivajirao Pandit on the occasion of his retirement on 31st May 2025, which will mark the culmination of a distinguished teaching career in the field of chemistry that spanned 35 years. He conveys his profound appreciation for the fact that you are a consistent source of motivation. In addition, Dr. Pandit would like to express his deepest gratitude to Shri Rajeshbhai Shah, Chairman of The PGK Mandal, Shri Hemantbhai Maniar, Secretary, and Joint Secretary Shri Dilipbhai Jagad for their assistance in providing laboratory facilities. One other distinguished personality who deserves special recognition is Shri Rajendra Gurao, who serves as the Principal of the Haribhai V. Desai College of Arts, Science, and Commerce (Autonomous) in Pune, India. He has provided invaluable assistance and support throughout this process.

***References**:*

1. Rehman J, et al. Interconnects for Flexible and Printed Electronic Applications. IEEE International Conference on Flexible and Printable Sensors and Systems (FLEPS) 2019:1–

2. Wang Z, et al. Application of MOFs driven by various energy sources for degradation the organic pollutants in water: A review. Coord Chem Rev 2024; 499:215506.

3. Farid MF, et al. In situ synthesis of manganese oxide/iron oxide/polyaniline composite catalyst for oxygen evolution reaction. J Mater Res 2024:1–11.

4. Gusain R, et al. Adsorptive removal and photocatalytic degradation of organic pollutants using metal oxides and their composites: A comprehensive review. Adv Colloid Interface Sci 2019;272:102009.

5. Carvalho M, et al. Assessment of the biodegradability of a monosulfonated azo dye and aromatic amines. Int Biodeter Biodegr 2008;62(2):96–103.

6. Safri AA, et al. Bacterial Disinfection Using Polymer Based Hybrids. Key Eng Mater 2018;778:331–5.

7. Guerra FD, et al. Nanotechnology for environmental remediation: materials and applications. Molecules 2018;23(7):1760.

8. Couto SR. Dye removal by immobilised fungi. Biotechnol Adv 2009;27(3): 227–35.

9. Hussain I, Amara U, Bibi F, Hanan A, Lakhan MN, Soomro IA, et al. Mo-based MXenes: Synthesis, properties, and applications. Adv Colloid Interface Sci 2024: 103077.

10. Shaheen I, Ali I, Bibi F, Hanan A, Ahmad M, Hussain I, et al. Integrating 1D/2D nanostructure based on Ni–Co-oxalate for energy storage applications. Ceram Int 2023.

11. ur Rehman J, et al. Conventional versus Flexible Substrates for Dye Sensitized and Perovskite Type Photo Voltaic Solar Cells. IEEE International Conference on Flexible and Printable Sensors and Systems (FLEPS) 2019:1–3.

12. Fei T, Ahmad T, Usman M, Ahmad A, Saleem A, Hanif MB, et al. Zn-doped Cr2O3 oxides boosted the electrochemical performance of aqueous hybrid supercapacitor. Electrochim Acta 2024;476:143673.

13. Mehran MT, Khan MZ, Song RH, Lim TH, Naqvi M, Raza R, et al. A comprehensive review on durability improvement of solid oxide fuel cells for commercial stationary power generation systems. Appl Energy 2023;352:121864.

14. Ali HG, Khan K, Hanif MB, Khan MZ, Hussain I, Javed MS, et al. Advancements in two-dimensional materials as anodes for lithium-ion batteries: Exploring composition-structure-property relationships emerging trends, and future perspective. J Energy Storage 2023;73:108980.

15. Shaheen I, Hussain I, Zahra T, Javed MS, Shah SSA, Khan K, et al. Recent advancements in metal oxides for energy storage materials: design, classification, and electrodes configuration of supercapacitor. J Energy Storage 2023;72: 108719.

16. Ekeoma BC, et al. Recent advances in the biocatalytic mitigation of emerging pollutants: a comprehensive review. J Biotechnol 2023.

17. Akhter P, et al. TiO2 decorated CNTs nanocomposite for efficient photocatalytic degradation of methylene blue. Diam Relat Mater 2024;141:110702.

18. Mondal S. Methods of dye removal from dye house effluent—an overview. Environ Eng Sci 2008;25(3):383–96.

19. Oladoye PO, et al. Methylene blue dye: Toxicity and potential technologies for elimination from (waste) water. Results Eng 2022:100678.

20. Titchou FE, et al. Removal of cationic dye from aqueous solution using Moroccan pozzolana as adsorbent: isotherms, kinetic studies, and application on real textile wastewater treatment. Groundw Sustain Dev 2020;11:100405.

21. Haruna A, Abdulkadir I, Idris SO. Visible light induced photodegradation of methylene blue in sodium doped bismuth barium ferrite nanoparticle synthesized by sol-gel method. Avicenna J Environ Health Eng 2018;5(2):120–6.

22. Haruna A, Abdulkadir I, Idris SO. Effect of annealing temperature on the synthesis and photocatalytic properties of Bi0.65K0.2Ba0.15FeO3 perovskite-like nanoparticle synthesized by sol-gel method. Beni-Suef Univ J Basic Appl Sci 2020; 9(1):1–8.

23. Ding Z, et al. Magnetically recyclable Ag/TiO2 co-decorated magnetic silica composite for photodegradation of dibutyl phthalate with fluorescent lamps. Water Sci Technol 2020; 81(4):790–800.

24. Latif Z, et al. Carbon quantum dots (CQDs) modified polymers: a mini review of non-optical applications. Nanoscale 2024.

25. Rashid AB, et al. Nanotechnology-enhanced fiber-reinforced polymer composites: Recent advancements on processing techniques and applications. Heliyon 2024.

26. Sen Gupta R, Samantaray PK, Bose S. Going beyond cellulose and chitosan: synthetic biodegradable membranes for drinking water, wastewater, and oil- water remediation. ACS Omega 2023;8(28):24695–717.

27. Chadha U, et al. A review of the function of using carbon nanomaterials in membrane filtration for contaminant removal from wastewater. Mater Res Express 2022;9(1):012003.

28. Abuhantash F, et al. Hydrophilic, oleophilic and switchable Janus mixed matrix membranes for oily wastewater treatment: A review. J Water Process Eng 2023; 56:104310.

29. Mautner A, et al. Nitrate removal from water using a nanopaper ion-exchanger. Environ Sci Water Res Technol 2016;2(1):117–24.

30. Nouri A, et al. Polymer-based nanocomposites for environmental remediation. In: Functional hybrid nanomaterials for environmental remediation. The Royal Society of Chemistry; 2021. p. 101–32.

31. Nasrollahzadeh M, et al. Recent developments in palladium (nano) catalysts supported on polymers for selective and sustainable oxidation processes. Coord Chem Rev 2019;397:54–75.

32. Li J, et al. Cu supported on polymeric carbon nitride for selective CO 2 reduction into CH 4: a combined kinetics and thermodynamics investigation. J Mater Chem A 2019;7(28):17014–21.

33. Haruna A, Abdulkadir I, Idris S. Photocatalytic activity and doping effects of BiFeO3 nanoparticles in model organic dyes. Heliyon 2020;6(1).

34. Gaur A, et al. Degradation of organic dyes by utilizing CaCu3Ti4O12 (CCTO) nanoparticles via tribocatalysis process. J Ind Eng Chem 2024;129:341–51. 16 S. Muzammal et al. Energy Conversion and Management: X 22 (2024) 100547

35. Gao J, Hanif MB, Zhang H, Motola M, Li C. X. Recent advances in microstructural control via thermal spraying for solid oxide fuel cells. Chem Eng J 2023:147352.

36. Hayat M, Zhou Y, Shah MZU, Hanif MB, Hou H, Arif U, et al. Exploring the electrochemical properties of CuSe-decorated NiSe2 nanocubes for battery- supercapacitor hybrid devices. Chemosphere 2023;340:139720.

37. Liapun V, Hanif MB, Sihor M, Vislocka X, Pandiaraj S, Unnikrishnan VK, et al. Versatile application of BiVO4/TiO2 S-scheme photocatalyst: Photocatalytic CO2 and Cr (VI) reduction. Chemosphere 2023;337:139397.

38. Thirunavukkarasu GK, Hanif MB, Liapun V, Hensel K, Kupˇcík J, Lorincik J, et al. Decrypting the growth of anodic TiO2 nanotube layers in eco-friendly fluoride- free nitrate-based electrolyte for enhanced photocatalytic degradation of organic pollutants. Mater Res Bull 2023;165:112322.

39. Hanif MB, Thirunavukkarasu GK, Liapun V, Makarov H, Gregor M, Roch T, et al. Fluoride-free synthesis of anodic TiO2 nanotube layers: A promising environmentally friendly method for efficient photocatalysts. Nanoscale 2022;14 (32):11703–9.

40. Sihor M, Hanif MB, Thirunavukkarasu GK, Liapun V, Edelmannova MF, Roch T, et al. Anodization of large area

Ti: a versatile material for caffeine photodegradation and hydrogen production. Cat Sci Technol 2022;12(16): 5045–52.

41. Hanif MB, Rauf S, Qayyum S, ˇ Sihor M, Motola M. Investigating the effect of rGO on microstructural and electrical properties of La 0.9 Sr 0.1 Ga 0.8 Mg 0.2 O 3 in intermediate temperature SOFCs. Sustainable Energy Fuel 2022;6(14):3465–76.

42. Thirunavukkarasu GK, Bacova J, Monfort O, Dworniczek E, Paluch E, Hanif MB, et al. Critical comparison of aerogel TiO2 and P25 nanopowders: Cytotoxic properties, photocatalytic activity and photoinduced antimicrobial/antibiofilm performance. Appl Surf Sci 2022;579:152145.

43. Khan K, Fu B, Xin H, Beshiwork BA, Hanif MB, Wu J, Wu M. Composite polymer electrolyte incorporating WO3 nanofillers with enhanced performance for dendrite-free solid-state lithium battery. Ceram Int 2023;49(3):4473–81.

44. Cheema DA, Danial MO, Hanif MB, Alghamdi AS, Ramadan M, Khaliq A, et al. Intrinsic properties and future perspective of HfO2/V2O5/HfO2 multi-layer thin f ilms via E-beam evaporation as a transparent heat mirror. Coatings 2022;12(4): 448.

45. Bai H, et al. MgAl2O4 incorporated catalytic ceramic membrane for catalytic ozonation of organic pollutants. Appl Catal B 2024;343:123527.

46. Mageshwari K, et al. Template-free synthesis of MgO nanoparticles for effective photocatalytic applications. Powder Technol 2013;249:456–62.

47. Salehifar N, Zarghami Z, Ramezani M. A facile, novel and low-temperature synthesis of MgO nanorods via thermal decomposition using new starting reagent and its photocatalytic activity evaluation. Mater Lett 2016;167:226–9.

48. Peng Q, et al. High-efficiency catalysis of peroxymonosulfate by MgO for the degradation of organic pollutants. Minerals 2019;10(1):2. [49] Raveesha H, et al. The electrochemical behavior, antifungal and cytotoxic activities of phytofabricated MgO nanoparticles using Withania somnifera leaf extract. J Sci: Adv Mater Devices 2019;4(1):57–65.

50. Giahi M, Rahbar A, Mehdizadeh K. Photochemical degradation of an environmental pollutant by pure ZnO and MgO doped ZnO nanocatalysts. Iran J Chem Chem Eng 2021;40(1):83–91.

51. Berradi M, et al. Textile finishing dyes and their impact on aquatic environs. Heliyon 2019;5(11).

52. Khalid N, et al. Enhanced photocatalytic activity of graphene–TiO2 composite under visible light irradiation. Curr Appl Phys 2013;13(4):659–63.

53. Khalid N, et al. TiO2-graphene-based composites: Synthesis, characterization, and application in photocatalysis of organic pollutants. Micro Nanomanuf 2018, 95–122.

54. Lee E, et al. Synthesis of TiO2 nanorod-decorated graphene sheets and their highly efficient photocatalytic activities under visible-light irradiation. J Hazard Mater 2012;219:13–8.

55. Yasasve M, et al. Unravelling the emerging carcinogenic contaminants from industrial waste water for prospective remediation by electrocoagulation–a review. Chemosphere 2022:136017.

56. Han T, et al. Comprehensive insights into core microbial assemblages in activated sludge exposed to textile-dyeing wastewater stress. Sci Total Environ 2021;791: 148145.

57. Tran UNT, et al. Characterization of self-dyed silk yarn with Rhodamine B dye for fashion applications. Int J Cloth Sci Technol 2023;35(3):477–92.

58. Khalid N, et al. Synergistic effects of Fe and graphene on photocatalytic activity enhancement of TiO2 under visible light. Appl Surf Sci 2012;258(15):5827–34.

59. Nasir A, et al. Review on the progress and future of TiO2/graphene photocatalysts. Energies 2022;15:6248. Note: MDPI stays neutral with regard to jurisdictional claims in published ….

60. Hou C, Hu B, Zhu J. Photocatalytic degradation of methylene blue over TiO2 pretreated with varying concentrations of NaOH. Catalysts 2018;8(12):575.

61. Balarak D, et al. Application of surfactant-modified bentonite for methylene blue adsorption from aqueous solution. Orient J Chem 2020;36(2):293.

62. Arias Arias F, et al. The adsorption of methylene blue on eco-friendly reduced graphene oxide. Nanomaterials 2020;10(4):681.

63. Siddeeg SM, et al. Iron oxide/chitosan magnetic nanocomposite immobilized manganese peroxidase for decolorization of textile wastewater. Processes 2019;8 (1):5.

64. Manimohan M, et al. Synthesis and characterisation of novel Cu (II)-anchored biopolymer complexes as reusable materials for the photocatalytic degradation of methylene blue. RSC Adv 2020;10(31):18259–79.

65. Giannakopoulou PP, et al. Does the methylene blue test give equally satisfactory results in all studied igneous rocks relative to the identification of swelling clay minerals? Minerals 2020;10(3):283.

66. Dante RC, et al. Methylene blue-carbon nitride system as a reusable air-sensor. Mater Chem Phys 2019;231:351–6.

67. Khan K, et al. Design of efficient and durable symmetrical protonic ceramic fuel cells at intermediate temperatures via B-site doping of Ni in BaCe0.56Zr0.2Ni0.04Y0.2O3–δ. Ceramics International 2023;49(11):16826–35.

68. Bayomie OS, et al. Novel approach for effective removal of methylene blue dye from water using fava bean peel waste. Sci Rep 2020;10(1):7824.

69. Sun L, et al. Oxidative degradation of methylene blue via PDS-based advanced oxidation process using natural pyrite. Int J Environ Res Public Health 2019;16 (23):4773.

70. Contreras M, et al. Bio-removal of methylene blue from aqueous solution by Galactomyces geotrichum KL20A. Water 2019;11(2):282.

71. Yaqub A, et al. Activated carbon derived from Dodonaea Viscosa into beads of calcium-alginate for the sorption of methylene blue (MB): Kinetics, equilibrium and thermodynamics. J Environ Manage 2023;327:116925.

72. Gillman P. Methylene blue implicated in potentially fatal serotonin toxicity. Anaesthesia 2006;61(10):1013–4.

73. Shakoor S, Nasar A. Adsorptive treatment of hazardous methylene blue dye from artificially contaminated water using cucumis sativus peel waste as a low-cost adsorbent. Groundw Sustain Dev 2017;5:152–9.

74. Setiadi T, Andriani Y, Erlania M. Treatment of textile wastewater by a combination of anaerobic and aerobic processes: A denim processing plant case. Proc Southeast Asian Water Environ 2006;1.

75. Hassan MM, Carr CM. A critical review on recent advancements of the removal of reactive dyes from dyehouse effluent by ion-exchange adsorbents. Chemosphere 2018;209:201–19.

76. Imran M, et al. Microbial biotechnology for decolorization of textile wastewaters. Rev Environ Sci Bio/technol 2015;14:73–92.

77. Li J, Wu N. Semiconductor-based photocatalysts and photoelectrochemical cells for solar fuel generation: a review. Cat Sci Technol 2015;5(3):1360–84.

78. Gershon T, et al. The role of sodium as a surfactant and suppressor of non- radiative recombination at internal surfaces in Cu2ZnSnS4. Adv Energy Mater 2015;5(2):1400849.

79. Nethercot Jr AH. Prediction of Fermi energies and photoelectric thresholds based on electronegativity concepts. Phys Rev Lett 1974;33(18):1088.

80. Fujishima A, Zhang X. Titanium dioxide photocatalysis: present situation and future approaches. C R Chim 2006;9(5–6):750–60.

81. Luo J, et al. Reveal Brønsted–Evans–Polanyi relation and attack mechanisms of reactive oxygen species for photocatalytic H2O2 production. Appl Catal B 2022; 301:120757.

82. Khan ZUH, et al. Removal of organic pollutants through hydroxyl radical-based advanced oxidation processes. Ecotoxicol Environ Saf 2023;267:115564.

83. Grela M, Coronel M, Colussi A. Quantitative spin-trapping studies of weakly illuminated titanium dioxide sols. Implications for the mechanism of photocatalysis. J Phys Chem 1996;100(42):16940–6.

84. McCormick WJ, et al. Enhanced monitoring of photocatalytic reactive oxygen species: using electrochemistry for rapid sensing of hydroxyl radicals formed during the degradation of coumarin. Chem A Eur J 2023.

85. Khan H, Shah MUH. Modification strategies of TiO2 based photocatalysts for enhanced visible light activity and energy storage ability: a review. J Environ Chem Eng 2023:111532.

86. Dufner L, et al. Immobilization of TiO2 photocatalysts for water treatment in geopolymer based coatings. Catalysts 2023;13(5):898.

87. Dong K, et al. Noble-metal-free electrocatalysts toward H2O2 production. J Mater Chem A 2020;8(44):23123–41.

88. Lousada CM, et al. Mechanism of H2O2 decomposition on transition metal oxide surfaces. J Phys Chem C 2012;116(17):9533–43.

89. Wang Y, et al. Singlet oxygen: Properties, generation, detection, and environmental applications. J Hazard Mater 2023:132538.

90. Nosaka Y, et al. Singlet oxygen formation in photocatalytic TiO 2 aqueous suspension. PCCP 2004;6(11):2917–8.

91. Konaka R, et al. Ultraviolet irradiation of titanium dioxide in aqueous dispersion generates singlet oxygen. Redox Rep 2001;6(5):319–25.

92. Bashir F. The detection, elimination and damaging effect of singlet oxygen in the photosynthetic apparatus of plants and microalgae. Hungary: Szegedi Tudomanyegyetem; 2021.

93. Khan SB, et al. Morphological influence of TiO2 nanostructures (nanozigzag, nanohelics and nanorod) on photocatalytic degradation of organic dyes. Appl Surf Sci 2017;400:184–93.

94. Mohamed MM, et al. Zinc oxide incorporated carbon nanotubes or graphene oxide nanohybrids for enhanced sonophotocatalytic degradation of methylene blue dye. Appl Surf Sci 2019;487:539–49.

95. Musmade S, et al. Synthesis of shape controlled Cu2O and Cu2O/TiO2-QD composite for degradation of Congo red dye under visible-light irradiation. J Water Environ Nanotechnol 2023;8(4):406–16.

96. Sun K, et al. Fabrication of α-Fe2O3@ rGO/PAN nanofiber composite membrane for photocatalytic degradation of organic dyes. Adv Mater Interfaces 2017;4(24): 1700845.

97. Kaushal S, et al. Photocatalytic degradation of tetracycline antibiotic and organic dyes using biogenic synthesized CuO/Fe2O3 nanocomposite: Pathways and mechanism insights. Environ Sci Pollut Res 2023;30(13):37092–104.

98. Taourati R, et al. Facile one-step synthesis of highly efficient single oxide nanoparticles for photocatalytic application. Sci Afr 2020;8:e00305. 17 S. Muzammal et al. Energy Conversion and Management: X 22 (2024) 100547

99. Chankhanittha T, et al. Performance of solvothermally grown Bi2MoO6 photocatalyst toward degradation of organic azo dyes and fluoroquinolone antibiotics. Mater Lett 2020;258:126764. [100] Chauhan M, et al. Proficient photocatalytic and sonocatalytic degradation of organic pollutants using CuO nanoparticles. J Nanomater 2020;2020:1–15.

101. Saravan RS, et al. Evaluation of the photocatalytic efficiency of cobalt oxide nanoparticles towards the degradation of crystal violet and methylene violet dyes. Optik 2020;207:164428.

102. Ikram M, et al. Graphene oxide-doped MgO nanostructures for highly efficient dye degradation and bactericidal action. Nanoscale Res Lett 2021;16:1–11.

103. Seidi F, et al. Synthesis of hybrid materials using graft copolymerization on non- cellulosic polysaccharides via homogenous ATRP. Prog Polym Sci 2018;76:1–39.

104. Qamar SA, et al. Alginate-based nano-adsorbent materials–Bioinspired solution to mitigate hazardous environmental pollutants. Chemosphere 2022;288:132618.

105. Jayakumar R, et al. Sulfated chitin and chitosan as novel biomaterials. Int J Biol Macromol 2007;40(3):175–81.

106. Woggum T, Sirivongpaisal P, Wittaya T. Properties and characteristics of dual- modified rice starch based biodegradable films. Int J Biol Macromol 2014;67: 490–502.

107. Lone IH, Kowsalya E, Rebecca LJ. Alginate fiber from brown algae. Pharm Lett 2016;8(8):68–71.

108. Moran JI, Vazquez A, Cyras VP. Bio-nanocomposites based on derivatized potato starch and cellulose, preparation and characterization. J Mater Sci 2013;48: 7196–203.

109. Loos M. Carbon nanotube reinforced composites: CNT Polymer Science and Technology. Elsevier; 2014.

110. Fang W, et al. Manufacture and application of lignin-based carbon fibers (LCFs) and lignin-based carbon nanofibers (LCNFs). Green Chem 2017;19(8):1794–827.

111. Wypych A. Databook of plasticizers. Elsevier; 2023.

112. Fei T, et al. Effective recovery of poly-β-hydroxybutyrate (PHB) biopolymer from C upriavidus necator using a novel and environmentally friendly solvent system. Biotechnol Prog 2016;32(3):678–85.

113. V. R. Uttam Pandit, G. K. Parshuram Jadhav, V. M. Sakharam Jawale, R. Dubepatil, R. Gurao and D. J. Late, RSC Adv., 2024, 14, 29099–29105.

114. V. Jawale, G. Gugale, M. Chaskar, S. Pandit, R. Pawar, S. Suryawanshi, V. Pandit, G. Umarji and S. Arbuj, J. Mater. Res., 2021, 36, 1573–1583.

115. V. U. Pandit, S. S. Arbuj, U. P. Mulik and B. B. Kale, Environ. Sci. Technol., 2014, 48, 4178–4183.

Biopolymer Applications Journal
e-ISSN: 2800-1729

Bahia MEGHLAOUI et al. Vol 5. N°1, 2026, pp. 17-21

Flexural properties of the composites polystyrene/fiber natural Alfa treated.

Bahia MEGHLAOUI[1*]; Mohand OULD OUALI[1]; Hocine SMAIN [2].

1: Laboratory Elaboration and Characterization of Materials and Modeling (LEC2M), Mouloud Mammeri of Tizi-Ouzou's university. Algeria

2: Laboratory Applied Chemistry and Chemical Engineering (LCAGC), Mouloud Mammeri of Tizi-Ouzou's university. Algeria

**Corresponding author*: bahia.meghlaoui@ummto.dz*

Received: 11 November 2025; Accepted: 25 December 2025; Published: 14 January 2026;

Abstract

The influence of chemical treatment on the flexural properties of Polystyrene/plant fiber composites has been studied. The Alfa fiber is used as reinforcement after been treated with a NaOH aqueous solution 3% for 24, 48 and 72 hours at 25°C. The results obtained show that the chemical modification of the Alfa fiber affects the mechanical properties of the composites. The flexural strength and flexural modulus were clearly improved with the treatment compared to the composites with the untreated fiber. In addition, an increase of the mechanical properties is observed with the increase of the treatment time. This improvement in the flexural properties is attributed to the good adhesion between the matrix and the reinforcement. SEM results show that treated Alfa fiber with 3% NaOH for 72 h makes the fiber surface smooth after removal of the non-cellulosic components and the water absorption rate decreases with the during treatment. This decrease is due to the reduction of hydroxyl groups in the fiber, following the removal of amorphous compounds.

Keywords: *Chemical treatment, plant Alfa, Polystyrene, Flexural properties.*

I. Introduction

Currently, scientific and technological efforts are focused on minimizing the environmental impacts associated with the use of polymer materials. Therefore, attention is increasingly being focused on biodegradable composite materials such as those based on polystyrene, polypropylene, etc., with natural fillers such as cellulose, starch, and plant fibers.

The use of plant-based fillers as reinforcements for composite materials offers numerous advantages due to their biodegradability, low cost, and mechanical properties. However, the adhesion between the hydrophilic surface of the fillers and the hydrophobic polymer used as a matrix is weak, which reduces the reinforcement capacity [1] – [3].

However, incorporating natural fibers sach as Alfa [4] into polymer materials creates compatibility issues du to the hydrophilic nature of the fibers and the hydrophobic character of the polymer matrix. We often use various methods, including as acetylation [5], alkali treatment [6,7], and methylation [8], to alter the matrix or the natural fiber in order to compensate for this issue [9]. Alkali treatment is the most popular method for treating natural fibers [4]. Natural fibers are impacted by alkalinization, which offers distinct performance. Hemicelluloses, lignin, and impurities including wax and lipids are extracted using this treatment [10].

.

The primary aim of this study is to examine the mechanical characteristics of polystyrene (PS) composites strengthened by Alfa natural fibers sourced from Alfa stalks. Alfa fibers have undergone chemical modification with sodium hydroxide solution to improve their affinity and adhesion to the polystyrene matrix. This approach would enable the development of a novel and eco-friendly composite material that poses no threat to the environment. To enhance the Alfa fibers-matrix interface, the effects of aqueous sodium hydroxide concentration and treatment duration have been examined. This study focuses on the development of the characteristics of composites made with PS as the matrix and both treated and untreated natural Alfa fibers. The experimental program consists of a series of texture assessments using FTIR, scanning electron microscopy (SEM) evaluations, water absorption and mechanical testing.

II. Material and methods

II.1 Materials

The polymer used in this work is polystyrene in the form of translucent granules. It was obtaining from the National Industrial Company (E.N.I.E.M), Algeria. It's melt index >12g/10min (200°C/5g) and the density of 1.05g/cm^3.

The alfa fiber is obtained from the alfa stem, from Djelfa, which underwent several preparation steps, consisting of a pretreatment in saline water for 24 hours at 60°C. This treatment aims to remove surface impurties sach as dust, waxes and soluble hemicelluloses, while also reducing the internal moisture content of the Alfa fibers [11]. The saline water increase the fiber roughness and improve wettability by the polymer matrix. As a result, the fiber-matrix interfacial

adhesion is Enhanced, leading to improved mechanical performance of the composite.

Followed by rinsing with distilled water and air-drying for 48h. subsequently, the Alfa fibers were subjected to alkaline treatment using a 3% sodium hydroxide (NaOH)solution during 24, 48 and 72 h at 25°C. After treatment, the Alfa fibers were neutralized with an acetic acid solution after being cleaned with distilled water. The fibers were dried for six hours at 60 °C.

II.2 Methods

Sample preparation

The treated and untreated alfa fiber of 5% to 30% (by weight) is mechanically mixed with polystyrene by a single-screw extruder TOSHIBA IS 150 E of 150 TONNES and then injected into molds to obtain plates. The samples for flexural testing are cut by a manual press.

Fourier transform infrared spectroscopy (FTIR) analysis

Fourier transform infrared spectroscopy (FTIR) analysis was performed to investigate the effect of the alkaline treatment on the Alfa fibers. The infrared spectra of the samples treated and untreated Alfa fiber were recorded using a vertex 70 spectrophotometer in ATR mode with a resolution of 2 cm^{-1}, in the region 4000 cm^{-1} to 400 cm^{-1}. The samples to be analysed are prepared in pellets form. This consists of a mixture of 0.001 g of previously groung fiber (treated or untreated) and 0.2 g of potassium bromide (KBr).

Scanning Electron Microscopy (SEM)

The morphology of the treated and untreated fibers by NaOH is observed by the Philips ESEM XL (tungsten filament) scanning electron microscope coupled to a complete energy dispersive microanalysis (EDS X) system.

Water absorption test

The water absorption test involves placing the sample in an oven at 70°C for 24 hours, then allowing them ton cool to room temperature in a desiccator. Next, they are weighed using a precision balance. After weighing, the samples are placed in distilled water at room temperature. According to ASTM D570, the changes in water absorption over time is modified. After wiping the samples with absorbent paper (to remove excess water in the surface), their weight is measured each time until saturation (in constant weight). Water absorption rate is determined by the following relation :

$$\text{Water absorption rate} = \frac{M_t - M_0}{M_0} * 100 \quad (1)$$

Where : M_t : the mass of the sample at time « t » (g).

M_0 : the mass of the sample at time « 0 » (g).

Flexural tests

The flexural properties of the composites, three-point bending tests were performed according to the NF T51-001 standard using dedicated mechanical testing setup.

The samples were tested using a Zwick/Roell Z 2.5 Machine (3mm/min). Flexural strength (Sf) and flexural modulus (Ef) were then obtained using the expressions :

$$s_f = \frac{3PL}{2bd^2} \quad (2)$$

$$E_f = \frac{ML^3}{4bd^3} \quad (3)$$

Where: **P:** The maximum load.
M: The slope of the initial straight-line portion of the load-displacement curve.
b and **d** are, respectively, the width and the thickness of the specimen.
L: The support span.

III. Results and discussion

III.1 Fourier transform infrared spectroscopy (FTIR) analysis

The changes in the surface structure of alfa fibers under alkaline treatment are observed using the infrared spectrum "**Figure 1**". The disappearance of the peak at 1735 cm-1, corresponding to the C=O carbonyl groups, is also observed due to the partial hydrolysis of hemicelluloses in an alkaline medium. The symmetrical and asymmetrical stretching vibrations corresponding to the C-H bonds of the (-CH2) groups of the cellulose and lignin segments are observed near 2924 cm-1, which are affected by the treatment.

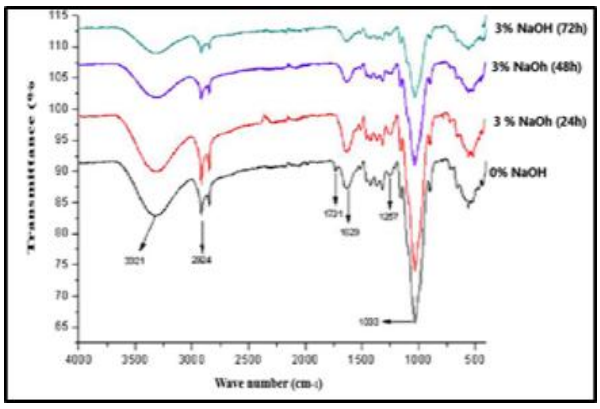

Figure 1. Infrared spectra in ATR mode of untreated alfa fibers and those treated with 3% NaOH for 24, 48 and 72 hours at 25°C.

III.2 Scanning Electron Microscopy (SEM)

Figure 2 shows the micrographs of fibers surface before and after treatment in 3% of aqueous caustic soda (NaOH) during 72 h. The change in the morphology of Alfa fibers during alkali treatment is very important.
We observe that the surface of untreated Alfa fibers surface is rough **(Figure 2(a))**. This can be referred to non-cellulosic components (waxy substances, oils and impurities) contained in these fibers [2]. The treated Alfa fibers (3% NaOH during 72h), surface becomes smooth after removal of the non-cellulosic components (**Figure 2(b)**).

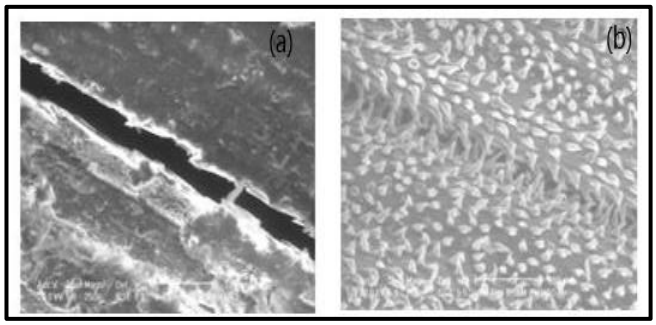

Figure 2. Different morphology of fiber Alfa :(a) untreated, (b) treated in aqueous caustic soda (3% NaOH during 72h).

III.3 Water absorption test

The evolution of the absorption rate of treated PS/Alfa fiber composites was studied. **Figure 3** present the results obtained with the materials immersed in water, with fiber contents of 5%, 15% and 25%. According to this figure, it is also observed the composites with untreated Alfa fiber that the water absorption rate increases with an increasing with proportion of Alfa fiber in PS matrix. This increase is linked to the macromolecular structure of Alfa fiber, which are rich hydroxyl groups (-OH). These groups form hydrogen bonds with water molecules.
Therefore, a greater fiber content leads to an increased concentration of hydroxyl groups, resulting in a higher of water absorption rate. These results are consistent with those found by Bessadok and al [12] and Pasquini and al [13].
Then, we observe that for the same treated Alfa fiber content, the water absorption rate decreases with the concentration and during treatment. This decrease is due to the reduction of hydroxyl groups in the fiber, following the removal of amorphous compounds.

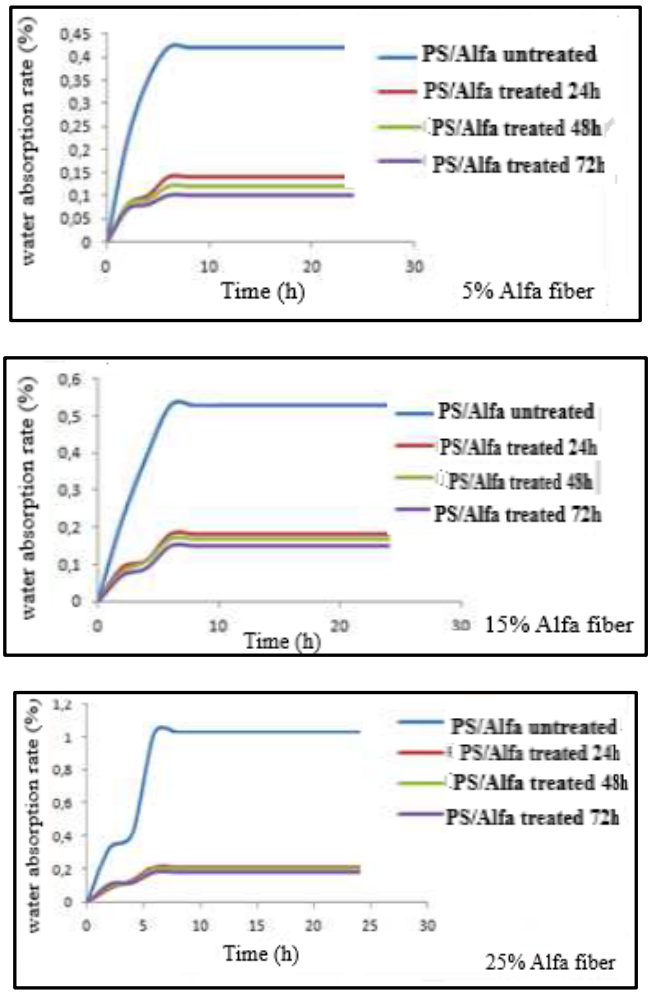

Figure 3. Evolution of the water absorption rate of PS/ Alfa fiber composites.

III.4 Flexural tests

The effect of fibers treatment with 3% NaOH for 24, 48, and 72 h at 25 ° C, that the flexural modulus and flexural strength can be seen in **Figure 4** and **Figure 5** respectively. Results show that mechanical properties are changed with fibers treatment. Figure 4 shows that the flexural modulus increased with the increase of the concentration of Alfa fibers treated varying from 5% to 30% (by weight) compared to the composites with untreated fibers. The increase in flexural strength is shown in Figure 5. It can be explained by a better fiber-matrix interaction [4]. Thus the mechanical properties are better with 3% NaOH for 72 h. The superior performance of 72h-treated fibers may result from more complete removal of surface impurities, leading to stronger interfacial bonding.
The results obtained indicate an improvement in the flexural properties of the composites developed, reinforced by fibers treated with sodium hydroxide [14].

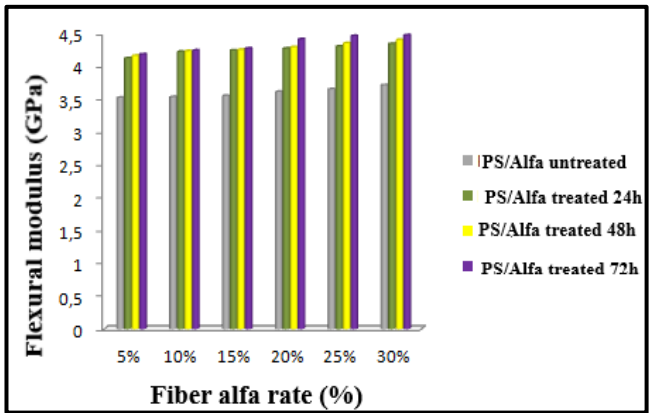

Figure 4. Flexural modulus of untreated Alfa/PS and treated Alfa/PS composites with 3% of NaOH for 24, 48 and 72 h at 25°C.

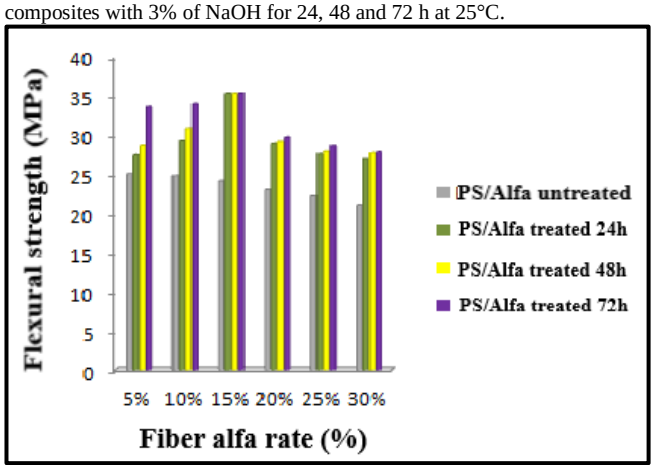

Figure 5. Flexural strength of untreated Alfa/PS and treated Alfa/PS composites with 3% of NaOH for 24, 48 and 72 h at 25°C.

IV. Conclusion

This study examines how the mechanical performance of PS composites is affected by both treated and untreated Alfa fibers. The micrographs showed a modification of the surface fiber including the disappearance of the waxy layer. Furthermore, these micrographs also revealed an increase in the roughness of the treated fibers compared to untreated Alfa fibers (elimination of non-cellulosic components).

Fourier transform infrared (FTIR) spectra revealed the change in the surface structure of the treated where the disappearance of the peak corresponding to the carbonyl groups of hemicellulose was observed. A decrease in the water absorption rate of the treated Alfa fibers was observed depending on the treatment. This is due to the elimination of non-cellulosic substances.

The Alfa fibers were treated by submerging them in a 3% sodium hydroxide solution (NaOH) for 24, 48, and 72 hours at 25°C. The findings demonstrate that the alkali treatment improved the flexural characteristics of their composites. These outcomes are explained by a significant improvement in the fiber's interfacial adhesion to the polystyrene matrix.

References:

1. N M Z Abidin, M T H Sultan, A U M Shah and S N A Safri. Charpy and Izod impact properties of natural fibre composites. *IOP Conf. Series: Materials Science and Engineering 670*, 2019.

2. Rokbi M., Osmani H., Imad A., and Benseddiq N., Effect Chemical treatment on Flexural Properties of Natural Fiber reinforced Polyester Composite. *Procedia Engineering.10* 2092–2097, 2011.

3. Toubal, S., Aribi, C., Chentir, I. *et al.* Synthesis of resin from Alfa stem to applied as an adhesive corrosion-resistant coating. *Proc. Indian Natl. Sci. Acad.* 2025.

4. B. Meghlaoui, M. Ould Ouali and S. Hocine. Effect of chemical treatment of Alfa natural fibers on the mechanical properties of polyethylene matrix composites. *U.P.B. Sci. Bull., Series B (ISSN 1454-2331), Vol. 81(2),* pp. 115-122, 2019.

5. Tserki V., Panayiotou C., Zafeiropoulos N. E. A. study of the effect of acetylation and propionylation on the interface of natural fibre biodegradable composites, *Advanced Composites Letters 14, 65-71,2005.*

6. Ray D., Sarkar B.K., Rana A.K., Bose N.R. Effect of alkali treated jute fibres on composite properties, *Bulletin of Materials Science*, Vol. 24, 129-135,2001.

7. Islam M.S., Pickering K.L., Foreman N.J. Influence of alkali treatment on the interfacial and physico-mechanical properties of industrial hemp fibre reinforced polylactic acid composites, *Composites : Part A*, vol. 41, 596-603,2010.

8. Naik J. B., Mishra S. Esterification effect of maleic anhydride on swelling properties of natural fiber/high density polyethylene composites, *Journal of Applied Polymer Science* 106, 2571-2574,2007.

9. Benyahia A., Merrouche A., Rahmouni Z.E.A., Rokbi M., Serge W., Kouadri Z. Study of the alkali treatment effect on the mechanical behavior of the composite unsaturated polyester-Alfa fibers. *Mechanics & Industry* 1569-73,2014.

10. Mohanty A. K., Misra M., Drzal L. T. Surface modifications of natural fibers and performance of the resulting biocomposites : An overview. *Composite Interfaces*, Vol. 8, No. 5 ,313-343, 2001.

11. Rogge E. Extraction et étude des propriétés physiques et mécaniques des fibres d'alfa (esparto grass) en vue d'applications textiles. Ecole Nationale Supérieure d'Ingénieurs Sud- Alsace (UHA), 2009 -2010.

12. Bessadok A., Marais S., Gouanvé F., Colasse L., Zimmerlin I., Roudesli S., Métayer M. Effect of Chemical Treatments of Alfa (Stipa Tenacissima) Fibres on Water Sorption Properties. *Composites Science and Technology*. Vol. 67, 685-697, 2007.

13. Pasquini D., Teixeira E.M., Silva Curvelo A.A., Belgacem M.N., Dufresne A. Surface esterification of cellulose fibres : Processing and characterisation of low density polyethylene/cellulose fibres composites, *Composites Science and Technology,* 68 : 193- 201,2008.

14. Mijiyawa F. formulation, caractérisation, modélisation et prévision du comportement thermomécanique des pièces plastiques et composites de fibres de bois : application aux engrenages. Thèse de doctorat en ingénierie (PH.D.), université du Québec à trois –rivières, 2017.

Biopolymer Applications Journal
e-ISSN: 2800-1729

Nabila BRAHMI-CHENDOUH et al. Vol 5. N°1, 2026, pp. 22-26

Development of a Stirred Yogurt Enriched with Carob Syrup and Powder.

Nabila BRAHMI-CHENDOUH[1]*, Dihia BABOURI[1]., Nada BOUGRIOU[1]., Roukia BOUIZAR[1]., Asma BOUDRIA[1]., Lila BOULEKBACHE[1].,khodir MADANI[1] .

1. *Laboratory of Biomathematics, Biochemistry, Biophysics and Scientometry, Faculty of Nature and Life Sciences, University of Bejaia, Bejaia 06000, Algeria*.
Corresponding author:* nabila.brahmi@univ-bejaia.dz
Received: 21 November 2025; Accepted: 23 December 2025; Published: 14 January 2026;

Abstract

Yogurt is a widely consumed dairy product appreciated for its taste, nutritional quality, and versatility. Carob (Ceratonia siliqua L.), a naturally gluten-free leguminous fruit, is rich in sugars, dietary fiber, and antioxidant compounds. Its consumption is associated with several health benefits, including weight management, relief from digestive disorders and diarrhea, and potential protective effects in individuals with hypertension or kidney stones. Recognized as safe by the U.S. Food and Drug Administration (FDA), carob represents a valuable functional ingredient.
This study aimed to evaluate the incorporation of carob powder and syrup into yogurt to develop a functional dairy product with improved nutritional and physicochemical properties. Three formulations were prepared: a control E (without carob), E1 (1% powder, 15% syrup), and E2 (3% powder, 9% syrup). E1 showed the highest acidity, °Brix, and viscosity, reflecting the strong structuring effect of combined carob powder and syrup. E2 exhibited intermediate values, while the control had the lowest measurements.
The results demonstrate that carob addition enhances yogurt's nutritional profile, texture, and overall quality. The strategic combination of powder and syrup provides both functional and technological benefits, creating a marketable product that aligns with consumer preferences and health-promoting properties

Keywords: *carob powder, carob syrup, functional yogurt, physicochemical analysis, sensory evaluation*

I. Introduction

The carob tree (Ceratonia siliqua L.) is a leguminous species cultivated throughout the Mediterranean region for its drought tolerance and versatile fruit (Biner et al., 2007; Avallone et al., 1997). In Algeria, it primarily grows in northern areas (Boublenza et al., 2019) and has recently attracted attention in the food industry due to its functional properties. Carob syrup, rich in sugars, serves as an energy source, while carob powder can be used as a caffeine-free cocoa substitute with favorable sensory characteristics (Tetik et al., 2011; Ayaz et al., 2009). Despite its potential, carob remains underutilized in dairy products in Algeria, particularly in the Bejaia region. The fermented yogurt sector,especially stirred yogurt, is expanding rapidly because of its soft, homogeneous texture and widespread consumer acceptance. This texture makes it suitable for incorporating functional ingredients such as carob. Previous studies have mainly focused on carob pods or single ingredients in dairyformulations. The present work aims to develop an innovative stirred yogurt enriched with both carob powder and syrup, evaluating its physicochemical and sensory properties. This approach explores the synergistic effects of combined carob ingredients, offering a new strategy to enhance yogurt's nutritional value, texture, and consumer appeal.

II. Material and methods

1. Preparation of Carob Powder: Carob pods were first cleaned by rinsing with cold water to remove dust and impurities. The pods were then spread on a tray lined with aluminium foil and dried in an oven at 40 °C until brittle, preventing bacterial growth and preserving the nutritional quality of the carob. After drying, the pulp was separated from the seeds and cut into smaller pieces. The pulp was then ground using a mortar and pestle to obtain a fine powder, which was finally sieved through a 250 µm mesh to ensure uniform particle size.

2. Physico-chemical analysis:
Carob powder: Titratable acidity was measured according to NF V 05-101 (1974). The pH was then determined by dissolving 1 g of powder in10 mL of distilled water using a calibrated glass electrode (NF V 05-108, 1970). Moistureand ash content were determined following AACC methods 44-

19.01 and 08-01.01 (2000), respectively. Total sugars were quantified using the method of Dubois et al. (1956), dietary fiber content was measured following AACC method 32-10.01, and lipid content was determined according to ISO 659 (1998).**Carob syrup**: Titratable acidity was assessed as described above. The pH was measured directly using a glass electrode. Soluble solids (°Brix) were determined by refractometry (AFNOR, 1970), and viscosity was measured at 25 °C using a rotary viscometer and expressed in mPa·s.

3. Phytochemical analysis: The total phenolic content (TPC) of carob extracts was determined using the Folin-Ciocalteu colorimetric method (Singleton et al., 1999). Total Flavonoid ContentFlavonoids were quantified using the aluminum chloride method (Bahorun et al., 1996). Condensed tannins were determined using the vanillin-HCl method, based on the formation of a red-violet complex with ferric chloride (Mole and Waterman, 1987; Bate-Smith, 1973).

4. Stirred Yogurt Preparation: Milk used for yogurt preparation corresponded to a standard industrial formulation for stirred yogurt. The milk was enriched with skimmed milk powder to increase total solids and ensure appropriate texture, then homogenized at 150 bar to achieve uniform distribution of solids. Pasteurization was carried out at 85 °C for 5 min, followed by rapid cooling to 42 °C.

The milk was inoculated with a commercial lactic starter culture (*Lactobacillus delbrueckii* subsp. *bulgaricus* and *Streptococcus thermophilus*). Fermentation was conducted in thermostatic tanks at 42 °C for 6 h. After coagulation, the yogurt was gently stirred to obtain a uniform consistency, and carob powder and syrup were added according to the formulations: E (control, without carob), E1 (15 g powder + 1 g syrup per 84 g base), and E2 (9g powder + 3 g syrup per 88 g base).

Finally, the yogurt was rapidly cooled to 4 °C to halt fermentation, portioned into sterile containers, and stored at 4 °C until physicochemical and sensory analyses were performed.

5. Enriched Yogurt Formulations: Three yogurt samples were prepared by incorporating carob powder and syrup into the yogurt base: E (Control) without carob, E1containing 3 g powder and 9 g syrup per 84 g base, and E2 containing 1 g powder and 15 g syrup per 88 g base.

6. Sensory Analysis: A panel of 16 healthy adult volunteers (10 men aged 29–47 and 6 women aged 21–48) evaluated the yogurt samples for overall appearance, texture, aroma, and taste (Lefebvre and Bassereau, 2003).

7. Statistical analysis: All data represent the average of three trials. For data processing, a statistical study was conducted using JMP software. The significance level of the results is taken at a probability of $p < 0.05$.

Theoretical package

Carob (Ceratonia siliqua L.) is rich in bioactive compounds, including polyphenols, flavonoids, and tannins, which contribute to antioxidant activity and potential health benefits. The Folin-Ciocalteu reagent is widely used to quantify total phenolic content because it oxidizes phenolic compounds, producing a blue complex whose intensity is proportional to phenolic concentration (Singleton et al., 1999). Similarly, flavonoids form yellow complexes with aluminum chloride through chelation of Al^{3+} ions, allowing spectrophotometric quantification (Bahorun et al., 1996; Ribéreau-Gayon and Gautheret, 1968).

The physicochemical properties of yogurt, such as viscosity and soluble solids (°Brix), are directly influenced by its composition, including added carob powder and syrup. Viscosity reflects the resistance to flow, affecting texture and mouthfeel, and is measured with a rotary viscometer (Decodts and Flamarion, 1985). Soluble solids measured by refractometry indicate sugar concentration, which is crucial for sweetness and overall sensory quality (AFNOR, 1970).

Understanding these principles provides a scientific basis for enriching yogurt with carob, predicting its impact on nutritional, physicochemical, and sensory properties, and guiding formulation strategies.

III. Results and discussion

1. Carob pulp powder composition: The analysis of carob pulp (Table 1) shows a mildly acidic pH of 5.2 ± 0.01 and titratable acidity of 4.8 ± 0.50%, reflecting its organic acid content. The pulp is rich in dietary fiber (13.97 ± 0.03%) and natural sugars (40.31±1.2), making it suitable for functional food applications. Moisture (10.02 ± 0.3%), ash (2 ± 0.4%), and lipid (1.02 ± 0.14%) contents indicate good stability and low-fat content. Bioactive compounds, including total phenolics (25.30 ± 2.1 mg/g), flavonoids (0.8± 0.06 mg/g), and tannins (2,99 ± 0.2 mg/g), suggest significant antioxidant potential, supporting the use of carob pulp to enhance both nutritional and functional properties in dairy products.

2. Physicochemical quality of carob syrup: The carob syrup exhibited a slightly acidic pH of 5.11 and a low titratable acidity of 0.88 ± 0.01%, indicating mild acidity suitable for food formulations. The °Brix value of 70.3% reflects a high sugar concentration, consistent with its function as a natural sweetener. The syrup viscosity was measured at 413.2 mPa·s, indicating a thick consistency that can influence texture and mouthfeel when incorporated into yogurt or other food products. Overall, these characteristics suggest that carob syrup can enhance sweetness, viscosity, and functional properties in enriched dairy formulations.

Tableau 1. Physicochemical properties of carob powder

Parameter	pH	Titratable acidity %	Fibres %	Moisture %	Ash %	Lipids %	Total sugar %	Polyphenols (mg/g)	Flavonoids (mg/g)	Tannins (mg/g)
Carob pulp	5,2±0,01	4,80±0,40	13,97±0,03	10,02±0,3	2±0,4	1,02±0,14	40,31±1.2	25,30 ± 2,1	0,8 ± 0,06	2,99 ± 0,2

Tableau 2. Physicochemical properties of carob syrup

Paramètre	pH	Acidité titrable %	Brix %	Viscosité CP (m.Pa.s)
Valeur	5,11	0,88±0,01	70,3	413,2

3. The physico-chemical characteristics of yogurt enriched with carob powder and syrup: The results are presented in Table 3. The chemical characteristics of theyogurt formulations differed significantly in pH, titratableacidity (°D**)**, °Brix, and apparent viscosity. The control formulation exhibited the highest pH (4.95 ± 0.05) and the lowest titratable acidity (73 ± 1 °D). Enrichment with carobpowder and syrup resulted in a decrease in pH and an increase in titratable acidity, consistent with the known inverse relationship between these parameters. Specifically, formulation E1 (1% powder, 15% syrup) had the highest titratable acidity (103.5 ± 1.5 °D**)** and a pH of 4.80 ± 0.10, whereas E2 (3% powder, 9% syrup) exhibited intermediate values (98 ± 1 °D, pH 4.79 ± 0.09). The slightly higher pH of enriched yogurts suggests that carob components modulate acid production during fermentation, likely through the buffering effect of its sugars and fibers as well as the activation of lactic cultures (Toker et al., 2013; Tounsi et al., 2019).

Tableau 3. Physicochemical properties of yoghurt enriched with carob powder and syrup.

Formulation	pH	Acidité °D	Brix	Viscosité cp (m Pa s)
E1(15%syrup -1%powder)	4,80±0,1 [b]	103,5± 1,5[a]	28,1±0,1[a]	18800±100[a]
E2 (9%syrup-3%powder)	4,79± 0,09 [ab]	98± 1 [b]	21,5± 0,5 [b]	16720± 120 [b]
E(control)	4,95±0,05[a]	73± 1 [c]	18± 0,1 [c]	3500± 100 [c]

Titratable acidity (°D) followed a similar trend: the increase in acidity of enriched yogurts can be attributed to enhanced growth of lactic acid bacteria promoted by carob fibers and phenolic compounds, which provide fermentable substrates and stimulate microbial activity (Radia et al., 2022; Öncel&Ozdemir, 2023).

The content of soluble solids (°Brix) increased with carob addition, reaching 28.1% in E1 compared to 18% in thecontrol. This increase reflects the contribution of sugars and galactomannans from carob syrup and powder, enhancing both the nutritional value and sensory properties of the yogurt (Tounsi et al., 2021). These carbohydrates also support lactic fermentation, contributing to the characteristic acidity and flavor.

The apparent viscosity increased markedly with carob enrichment: E1 reached 18,800 ± 100 mPa·s, E 16,720 ± 120 mPa·s, while the control had only 3,500 ± 100 mPa·s. This improvement is mainly due to galactomannans and soluble solids in carob syrup and powder, which enhance waterretention, reduce syneresis, and strengthen the yogurt matrix (Tounsi et al., 2021). The higher syrup content in E1 explains its superior viscosity despite E2 containing more powder.

Overall, carob enrichment improves the technological and functional properties of yogurt, including texture, stability, and sensory quality, demonstrating its potential as a natural functional ingredient.

4. The sensory evaluation of yogurts enriched with carob powder and syrup: The sensory evaluation revealed clear differences among the three formulations (E1: 1% powder + 15% syrup, E2: 3% powder + 9% syrup, E: control) in terms of appearance, texture, odor, and taste. In terms of appearance, E exhibited the highest homogeneity and a balanced level of particles and gloss, while E2 was the glossiest but showed lower homogeneity and more visible particles, and E1 appeared uniform and particle-free but less shiny. Texture analysis indicated that E was the creamiest and smoothest sample, E1 slightly less so, and E2 showed a slightly granular mouthfeel, which may be related to the higher addition of

syrup and carob solids. Odor perception was mild in E1, moderate in E2, and strongest in E, reflecting the influence of the different syrup and powder proportions. Regarding taste, all samples showed low acidity, but sweetness was highest in E and E2 andmoderate in E1, while bitterness was negligible overall.

Overall, these results demonstrate that higher syrup content enhances gloss, sweetness, and aroma intensity but may reduce homogeneity and smoothness, whereas higher powder content favors visual uniformity and a milder sensory profile. However, the control formulation (E3) provided the most balanced and harmonious combination of sensory attributes and was generally preferred. This finding highlights a trade-off between the improvement of functional properties through carob enrichment (higher fiber content, increased °Brix and viscosity) and the maintenance of optimal sensory quality, and should be carefully considered in future formulation strategies.To overcome this limitation, future formulations should focus on optimizing the level and ratio of carob syrup and powder, for example by testing intermediate or lower inclusion levels that maintain fiber enrichment while minimizing adverse effects on texture and sweetness. In addition, the use of complementary flavoring strategies (such as vanilla, fruit preparations or natural sweeteners) could help to enhance sweetness perception and mask potential off-flavors associated with carob. Finally, carob-enriched yogurt may be specifically positioned for health-conscious consumer segments who are more willing to accept fewer sweet products in exchange for higher fiber content and additional functional benefits

IV. Conclusions

This study characterized carob powder and syrup and assessed their impact on enriched yogurt. Carob powder, rich in fiber and phenolic compounds, provided structure and bioactive properties, while the syrup, with high °Brix and sugar content, enhanced sweetness, viscosity, and solids content. The combination of powder and syrup allowed modulation of yogurt physicochemical and sensory attributes, demonstrating that their proportions can be adjusted to optimize stability, nutritional value, and consumer acceptability. These results highlight the potential of carob as a functional ingredient in dairy products.

References:

1. A. Aafi. Le caroubier : Caractères botaniques et écologiques, groupements végétaux, techniques d'élevage en pépinière, traitement et soins culturaux, utilisation et production. Centre National de la Recherche Forestière, Maroc 1996, 1-7, 1996..
2. F.A. Ayaz, H. Torun, R.H. Glew, Z.D. Bak, L.T. Chuang, J.M. Presley, R. Andrews. Nutrient content of carob pod (Ceratonia siliqua L.) flour prepared commercially and domestically. Plant Foods for Human Nutrition, 64(4), 286. 2009.
3. T. Bahorun, B. Gressier, F. Trotin, C. Brunete, T. Dine, J. Vasseur, J.C. Gazin, M. Pinkas, M. Luycky, M. Gazin. Oxygen species scavenging activity of phenolic extracts from hawthorn fresh plant organs and pharmaceutical preparations. Arzneimittel-Forschung, 46, 1086-1089. 1996.
4. E.C. Bate-Smith. Ahaemanalysis of tannin: The concept of relative astringency. Phytochemistry, 12, 907-912. 1973.
5. B. Biner, H. Gubbuk, M. Karhan, M. Akus, M. Pekmezei. Sugar profiles of the pods cultivated and wild types of carob bean (Ceratonia siliqua L) in Turkey. Food Chemistry, 100, 1453-1455. 2007.
6. I. Boublenza, S. Ghezlaoui, M. Mahdad, F. Vasaï, F. Chemat. Algerian carob (Ceratonia siliqua L.) populations: Morphological and chemical variability of their fruits and seeds. Scientia Horticulturae, 256, 108537. 2019.
7. M. Dubois, K.A. Gilles, J.K. Hamilton, P.T. Rebers, F. Smith. Colorimetric method for determination of sugars and related substances. Analytical Chemistry, 28(3), 350-356. 1956.
8. FAO. OECD/FAO 2020. OECD-FAO Agricultural Outlook 2020-2029. Dairy and dairy products, , 174-183. 2020.
9. A. Lefebvre, J.F. Bassereau. L'analyse sensorielle, une méthode de mesure au service des acteurs de la conception: Ses avantages, ses limites, ses voies d'amélioration. Application aux emballages, 3, 1-11. 2003.
10. S. Mole, P.G. Waterman. Tonic acid proteolic enzymes: Enzyme inhibition substrat derivation. Photochemistry, 26, 99-102. 1987.
11. B. Öncel, Y. Ozdemir. Investigation of the effect of using carob molasses pulp (CMP) on physicochemical, functional and sensory properties of yogurt. Toros University Journal of Food, Nutrition and Gastronomy 2023, 2.
12. A. Radia, C. Hano, D. Oomah, F. Yous, S. Ayouaz, K. Madani, L. Boulekbache-Makhlouf. Impact of carob (Ceratonia siliqua L.) pulp flour supplementation on probiotic viability, milk fermentation and antioxidant capacity during yogurt storage.North African Journal of Food and Nutrition Research, 6(14), 154–164. Retrieved from https://www.ajol.info/index.php/najfnr/article/view/266271
13. M.N. Rejeb. Le caroubier en Tunisie: Situation et perspectives d'alimentation en Quel avenir pour l'amélioration des plantes? Ed AUPELF URGF, John IbbeyEurotext, Paris 1995, 79..

14. J. Ribéreau-Gayon, R. Gautheret. Les composés phénoliques des végétaux. Ed Dunod, Paris 1968, 5-7, 10-13, 55-86..
15. V.L. Singleton, R. Orthofer, R.M. Lamuela-Raventos. Analyse des phénols totaux et autres substrats d'oxydation et antioxydants par le réactif de Folin-Ciocalteu. Methods in Enzymology 1999, 299, 152-178..
16. N. Tetik, I. Turhan, H.R. Oziyci, M. Karhan. Determination of d-Pinitol in Carob Syrup.International Journal of Food Sciences and Nutrition 62, 572-576, 2011.
17. O.S. Toker, M. Dogan, N.B. Ersöz, M.T. Yilmaz. Optimization of the content of 5-hydroxymethylfurfural (HMF) formed in some molasses types: HPLC-DAD analysis to determine effect of different storage time and temperature levels. Industrial Crops and Products, 50, 137-144, 2013.
18. L. Tounsi, I. Ghazala, N. Kechaou. Physicochemical and phytochemical properties of Tunisian carob molasses. Journal of Food Measurement and Characterization, 14, 20-30. 2021.
19. L. Tounsi, H. Kchaou, F. Chaker, S. Bredai, N. Kechaou. Effect of adding carob molasses on physical and nutritional quality parameters of sesame paste. Association of Food Scientists &Technologists, 56(3), 1502-1509. 2019.
20. L. Tounsi, N. Kechaou. Le caroubier (Ceratoniasiliqua L.) et ses fruits: Descriptions, intérêts et applications. Éditions UniversitairesEuropéennes, Sarrebruck, Allemagne 2017..

Biopolymer Applications Journal
e-ISSN : 2800-1729
Rebiha BELLACHE et al. Vol 5. N°1, 2026, pp. 27-32

Development and Characterization of Prickly Pear Seed Oil Microcapsules in a Biopolymeric Alginate-Gelatin Matrix for Controlled Release

Rebiha BELLACHE[1,2*]; Dalila HAMMICHE[2]; Aicha DEHANE[2,3]

[1]*Université M'Hamed Bougara de Boumerdès, Faculté de Technologie, Département de Génie des Procédés, Boumerdès 35000, Algérie*
[2]*Université de Bejaia, Faculté de Technologie, Laboratoire des Matériaux Polymères Avancés Route De Targa- Ouzemmour, Bejaia 06000, Algérie*
[3]*Department of Chemistry, Dr. B.R. Ambedkar National Institute of Technology, Jalandhar 144 027,Punjab- India*
**Corresponding author email: rebiha.bellache@univ-bejaia.dz*
Received: 25 October 2025; Accepted: 13 December 2025; Published: 10 January 2026;

Abstract

This study aimed to encapsulate the sensitive bioactive compounds of Prickly Pear Seed Oil (PPSO) (Opuntia ficus-indica) using a biopolymeric matrix composed of sodium alginate and gelatin. PPSO, which is rich in essential fatty acids and antioxidants, is highly susceptible to degradation caused by light, oxygen, and heat. Microcapsules were prepared using the complex coacervation technique to enhance oil stability and ensure controlled release under physiological conditions. The physicochemical, structural, and thermal properties of the microcapsules were evaluated using UV–Visible spectroscopy, FTIR, thermogravimetric analysis (TGA), and differential scanning calorimetry (DSC). The results confirmed successful oil encapsulation and improved thermal stability compared to pure PPSO. The formulation containing 0.75 g of oil exhibited the highest encapsulation efficiency (93.51%) and the most favorable controlled release behavior. Release studies demonstrated low oil release in simulated gastric fluid (pH 1.2), followed by a sustained and controlled release in simulated intestinal media (pH 6.8 and 7.4). These findings highlight the effectiveness of the alginate–gelatin system for stabilizing PPSO, offering promising potential for applications in food, cosmetic, and pharmaceutical industries.

Keywords: *Alginate, Gelatin, Controlled Release, Encapsulation, Prickly Pear Seed Oil*

I. Introduction

Microencapsulation is a widely used technique in the food, cosmetic, and pharmaceutical industries for the protection, stabilization, and controlled delivery of sensitive bioactive compounds. This approach involves enclosing an active core material within a protective polymeric matrix, thereby reducing its exposure to environmental factors such as oxygen, light, moisture, and temperature fluctuations. As a result, microencapsulation enhances the stability, bioavailability, and shelf life of high-value natural ingredients, particularly oils rich in polyunsaturated fatty acids [01-03].

The successful application of microencapsulation is pivotal for preserving the functional integrity and extending the shelf life of high-value compounds, thereby enhancing product quality and efficacy [04]. Among the diverse methods available for microencapsulation, complex coacervation is recognized for its operational simplicity, high encapsulation efficiency, and ability to produce robust, high-density microcapsules using food-grade biopolymers [05]. This phase separation technique is fundamentally driven by the electrostatic attraction between two oppositely charged polymeric materials in an aqueous medium. A highly effective and industrially relevant coacervation system utilizes the positively charged protein, gelatin, and the negatively charged polysaccharide, sodium alginate [06]. By precisely controlling critical parameters, notably pH and temperature, the interaction between the carboxyl groups of alginate and the protonated amino groups of gelatin leads to the formation of an insoluble coacervate complex. This dense, biopolymeric liquid phase preferentially precipitates around the dispersed core material, forming a continuous microcapsule wall that is subsequently stabilized, often through cross-linking, to yield a solid, protective structure [07]. The present study focuses on the stabilization of Prickly Pear Seed Oil (PPSO), extracted from the seeds of Opuntia ficus-indica. PPSO has garnered significant global

attention for its superior composition, which is characterized by an exceptionally high content of polyunsaturated fatty acids, primarily linoleic acid (up to 70%), and potent lipophilic antioxidants, including a rich profile of tocopherols and phytosterols [08]. These bioactive components confer remarkable nutritional, anti-inflammatory, and skin-regenerating properties, positioning PPSO as one of the most valuable vegetable oils in the cosmetic and functional food markets [09].

However, the chemical profile responsible for PPSO's high value specifically its high degree of unsaturation also dictates its inherent instability. The numerous double bonds in the fatty acid chains are highly susceptible to autoxidation, a chain reaction drastically accelerated by exposure to light and atmospheric oxygen [10]. This oxidative degradation leads to the rapid depletion of beneficial antioxidants, the formation of undesirable volatile off-compounds (rancidity), and a significant loss in the oil's functional and sensory quality. Consequently, the commercial application of PPSO is severely limited by its short shelf life under ambient conditions.

Therefore, the primary objective of this work was to employ the gelatin-sodium alginate complex coacervation method for the efficient microencapsulation of PPSO. The goal is to construct a resilient biopolymeric shell that functions as an effective barrier to protect the oil from photo- and thermo-oxidative degradation. Through comprehensive physicochemical characterization, morphological analysis, and an assessment of the release kinetics in simulated media, this research seeks to demonstrate a viable strategy for stabilizing Prickly Pear Seed Oil, ensuring the preservation of its bioactivity for long-term industrial and consumer use.

II. Material and methods

2.1. Materials

The natural extract used was Prickly Pear Seed Oil (PPSO) (Opuntia ficus-indica), commercialized as Golden Brand Herbal Oil. The biopolymeric matrix was formed using Sodium Alginate (Alg) and Gelatin (Gel). Other chemicals included Polyethylene Glycol (PEG 6000), Polysorbate 80 (Tween 80), and various reagents used for pH control and solution preparation, such as Sodium Hydroxide (NaOH), Sodium Chloride (NaCl), Monopotassium Phosphate (KH_2PO_4), Hydrochloric Acid (HCl), and n-hexane.

2.2. Microcapsule Preparation

The microcapsules containing Prickly Pear Seed Oil (PPSO) Prickly pear seed oil (PPSO) microcapsules were prepared using the complex coacervation technique with sodium alginate (Alg) and gelatin (Gel) as wall materials. Sodium alginate was dissolved in deionized water at a concentration of 2% (w/v) under continuous magnetic stirring at 40 °C until complete solubilization. Gelatin was dissolved separately in deionized water at 2% (w/v) under the same conditions. The two polymer solutions were then mixed at an Alg/Gel mass ratio of 1:1. The pH of the biopolymeric mixture was carefully adjusted to pH 4.0 ± 0.1 using 0.1 M HCl, corresponding to the optimal pH range for electrostatic interaction between the negatively charged carboxylate groups of alginate and the positively charged amino groups of gelatin, thus inducing complex coacervation. Prickly pear seed oil was incorporated into the polymeric mixture at three different concentrations (0.5 g, 0.75 g, and 1 g) under high-speed mechanical stirring at 10,000 rpm for 10 minutes to form a stable oil-in-water emulsion. Tween 80 (1% w/v) was added as an emulsifying agent to enhance oil dispersion, while PEG 6000 (1% w/v) was used as a plasticizer to improve the flexibility and integrity of the microcapsule wall. Cross-linking of the formed coacervates was achieved by the dropwise addition of calcium chloride ($CaCl_2$, 0.2 M) under gentle stirring for 30 minutes, allowing ionic gelation of the alginate chains and stabilization of the microcapsules. The resulting microcapsules were collected by filtration, washed thoroughly with deionized water to remove unencapsulated oil and residual reagents, and then dried at 40 °C for 24 h. The dried microcapsules were stored in airtight containers at room temperature until further characterization.

Solutions buffered at controlled pH were prepared to assess the release in simulated physiological environments.

- **Simulated Gastric Fluid (SGF)**: pH 1.2, prepared using NaCl and HCl.
- **Simulated Intestinal Fluid (SIF, duodenum)**: pH 6.8, prepared using KH_2PO_4 and NaOH.
- **Phosphate Buffer Solution (PBS)**: pH 7.4, simulating other physiological fluids.

2.3. Characterization Techniques

The prepared microcapsules were characterized using several analytical techniques:

- **UV-Visible Spectroscopy:** by SpectroScan 50, used to establish the calibration curve of the PPSO and determine the **Encapsulation Efficiency (EE)** and concentration.

$$EE\% = 100 * \frac{Ccp}{Ci} \qquad (1)$$

- **Infrared Spectroscopy (FTIR):** using SHIMADZU FTIR-8400S in the range of 4000-400 cm-1 with a resolution of 4 cm-1. Used to identify the functional groups of the oil and the biopolymers, confirming the

successful encapsulation and interactions within the matrix.

- **Thermal analysis: Thermogravimetric Analysis (ATG) and Differential Scanning Calorimetry (DSC):** using a LINSEIS STAPT 1600 type thermogravimetric apparatus, in the temperature range from 20 -700 °C and a heating rate of 10 °C/min. Performed to evaluate the **thermal stability** and behavior of the raw materials and the final microcapsules.
- **Controlled Release Kinetics:** A volume of 100 mL of each buffered solution at pH1.2 (SGF), pH 6.8 (SIF), and pH 7.4 (PBS) was transferred into separate Erlenmeyer flasks. Subsequently, three microcapsule samples, each weighing 1g and corresponding to the optimal formulation prepared with 0.75g of oil, were introduced into the respective solutions.

The objective of this procedure was to initiate the controlled release study of the encapsulated oil under simulated physiological conditions (gastric, intestinal, and colonic) to evaluate the gastroprotective capacity and targeted delivery performance of the alginate-gelatin microcapsule system.

III. Results and discussion

3.1. UV-Visible Spectroscopy and Encapsulation Efficiency

UV-Visible spectroscopy was used to establish the calibration curve of the Prickly Pear Seed Oil at the maximum absorption wavelength of λ=278nm (Figure 1). Analysis of the supernatant allowed for the determination of the Encapsulation Efficiency (EE) (Table 1). The microcapsule formulation prepared with 0.75g of PPSO demonstrated the best encapsulation yield. The optimal encapsulation efficiency achieved with the 0.75g formulation was 93.51%. This high efficiency confirms the suitability of the alginate-gelatin system for retaining the oil. The same result was observed by Chen et al. (2022), who noted that the combination of isolated soybean proteins (SPI) and soy polysaccharides (SPS) as wall materials offered a high encapsulation efficiency (63.55%) for seabuckthorn seed oil, highlighting the importance of choosing appropriate encapsulation materials [11].

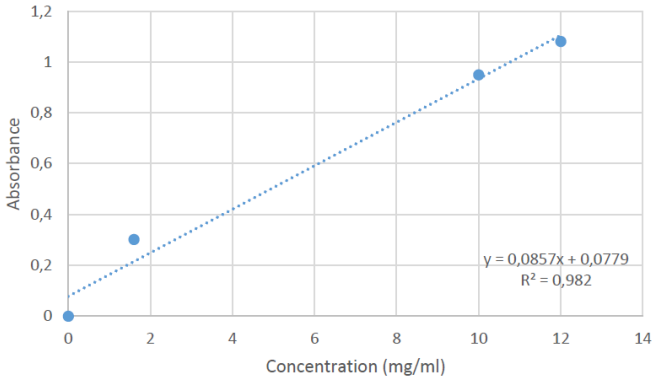

Figure 1. Calibration Curve of Prickly Pear Seed Oil (PPSO) at λ= 278 nm.

Table: Influence of PPSO concentration on encapsulation efficiency

Ci PPSO (mg/ml)	25	37,5	50
Ccp PPSO (mg/ml)	23,37	33,28	49,36
EE%	88,76 ±2	93,51 ±2	98,73 ±2

3.2. **Fourier-Transform Infrared Spectroscopy (FTIR)**

FTIR spectroscopy was employed to confirm the successful encapsulation of Prickly Pear Seed Oil (PPSO) within the alginate–gelatin matrix and to investigate possible intermolecular interactions between the core and wall materials (Figures 2 and 3). The FTIR spectrum of sodium alginate exhibited a broad absorption band in the range 3200–3400 cm^{-1}, attributed to O–H stretching vibrations, and a band at 2920 cm^{-1} corresponding to C–H stretching. The characteristic asymmetric and symmetric stretching vibrations of carboxylate groups ($–COO^-$) were observed at 1602 cm^{-1} and 1415 cm^{-1}, respectively, confirming the polysaccharide structure of alginate.[12]. The gelatin spectrum displayed typical protein-related bands, including a broad O–H/N–H stretching band at 3294 cm^{-1}, the Amide I band at 1641 cm^{-1} (C=O stretching), Amide II at 1544 cm^{-1} (N–H bending and C–N stretching), and Amide III at 1230 cm^{-1}, which are characteristic of peptide bonds.[13]. The FTIR spectrum of PPSO revealed the typical features of triglyceride-based oils. A strong absorption band at 1740 cm^{-1} was assigned to the ester carbonyl (C=O) stretching vibration, while bands at 2850–2950 cm^{-1} corresponded to symmetric and asymmetric stretching of aliphatic C–H groups. A weak band around 3006 cm^{-1} indicated the presence of unsaturated C=C–H stretching, and bands in the region 1160–1090 cm^{-1} were associated with C–O ester linkages.[14]. The FTIR spectra of the PPSO-loaded microcapsules (0.5 g, 0.75 g, and 1 g) showed the presence of characteristic peaks of both the biopolymeric matrix and the oil, confirming successful encapsulation. Notably, the ester

C=O band of PPSO at 1740 cm^{-1} was preserved in all formulations, indicating that the chemical structure of the oil remained intact after encapsulation.[15]. A slight shift of the alginate carboxylate asymmetric stretching band from 1602 cm^{-1} (pure alginate) to approximately 1594–1597 cm^{-1} in the microcapsules suggests electrostatic interactions between alginate carboxyl groups and protonated amino groups of gelatin. Additionally, changes in the intensity of the O–H/N–H stretching band (3200–3400 cm^{-1}) indicate the formation of hydrogen bonding interactions within the alginate–gelatin–oil system. Among the three formulations, the microcapsules containing 0.75 g of PPSO exhibited the highest intensity of oil-related bands (2920 cm^{-1} and 1740 cm^{-1}), suggesting a more homogeneous oil distribution and improved encapsulation efficiency. In contrast, the 1 g formulation showed comparatively lower relative intensity, which may indicate partial matrix saturation and less uniform dispersion of the oil at higher loading levels. Overall, the FTIR results confirm the successful encapsulation of PPSO within the alginate–gelatin matrix through physical interactions, without chemical degradation of the oil. The 0.75 g formulation provides the most favorable interaction balance.[16] and [17].

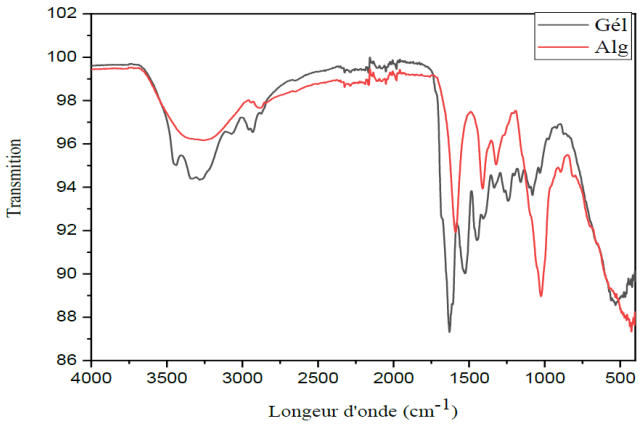

Figure 2. Infrared spectrophotometer analysis of Alginate (Alg) and Gelatin (Gel)

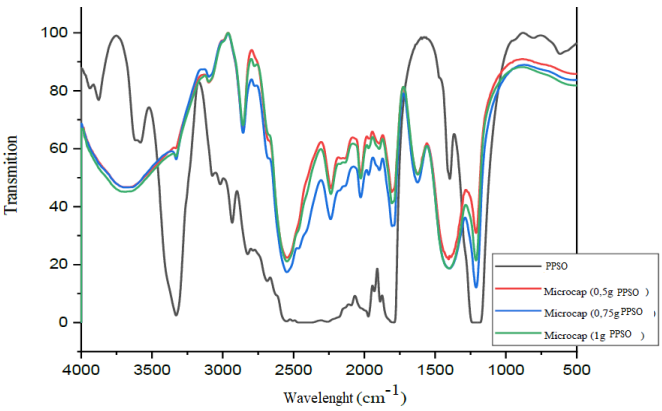

Figure 3. Infrared spectra of PPSO (oil), Alg (alginate), Gel (gelatin), and microcapsules containing 0.5 g, 0.75 g, and 1 g of PPSO.

3.3. Thermal Stability (ATG/DSC)

Thermogravimetric analysis was performed to evaluate the thermal stability and degradation behavior of pure PPSO, the individual wall materials (alginate and gelatin), and the PPSO-loaded microcapsules containing 0.5 g, 0.75 g, and 1 g of oil (Figure 4).The TGA curves of sodium alginate and gelatin exhibited an initial mass loss of approximately 8–12% between 30 °C and 150 °C, which can be attributed to the evaporation of physically and chemically bound water. The main degradation stage of both biopolymers occurred between 230 °C and 380 °C, corresponding to the decomposition of the polymer backbone. Pure PPSO showed a single major degradation step starting at an onset temperature (Tonset) of approximately 300 °C, with rapid mass loss up to 450 °C, indicating its high susceptibility to thermal degradation. In contrast, the PPSO-loaded microcapsules exhibited enhanced thermal stability compared to pure oil. The onset degradation temperatures were shifted to lower but more gradual degradation profiles, with Tonset values of approximately 225 °C, 239 °C, and 245 °C for microcapsules containing 0.5 g, 0.75 g, and 1 g of PPSO, respectively. This behavior indicates that the polymeric matrix effectively delays and moderates oil degradation by acting as a thermal barrier. Moreover, the residual mass at 700 °C increased with increasing oil content, reaching its highest value for the 1 g PPSO formulation, which suggests improved char formation and enhanced structural stability due to stronger polymer–oil interactions. Although the 1 g formulation exhibited the highest thermal resistance, the 0.75 g formulation presented a favorable balance between thermal stability and encapsulation homogeneity. These results confirm that encapsulation within an alginate–gelatin matrix significantly improves the thermal resistance of PPSO, making the system suitable for applications involving moderate thermal processing.[18].

DSC analysis of the microcapsules

Differential scanning calorimetry was employed to further investigate the thermal transitions and stability of the PPSO-loaded microcapsules (Figure 5).

All formulations exhibited a first endothermic peak between 50 °C and 100 °C, which is attributed to the evaporation of residual moisture entrapped within the biopolymeric matrix. This endothermic event was less intense for the microcapsules containing 1 g of PPSO, indicating reduced water affinity due to increased hydrophobicity. A major exothermic transition was observed between 350 °C and 470 °C for all microcapsule formulations, corresponding to the thermal decomposition of the alginate–gelatin network and the encapsulated oil. The position and intensity of this peak varied with oil

concentration. The microcapsules containing 1 g of PPSO exhibited the highest peak temperature, indicating superior thermal stability, whereas the 0.5 g formulation showed a broader and less intense peak, suggesting lower resistance to thermal stress. The 0.75 g PPSO formulation displayed intermediate thermal behavior, with a well-defined exothermic peak and moderate enthalpy change, reflecting a stable and homogeneous microcapsule structure. This formulation combines sufficient hydrophobicity, high encapsulation efficiency (93.51%), and satisfactory thermal resistance, making it the most suitable candidate for controlled release applications.,Overall, DSC analysis corroborates the TGA results and demonstrates that increasing PPSO content enhances the thermal stability of the microcapsules. However, an intermediate oil loading (0.75 g) provides the optimal compromise between thermal performance and encapsulation efficiency [19].

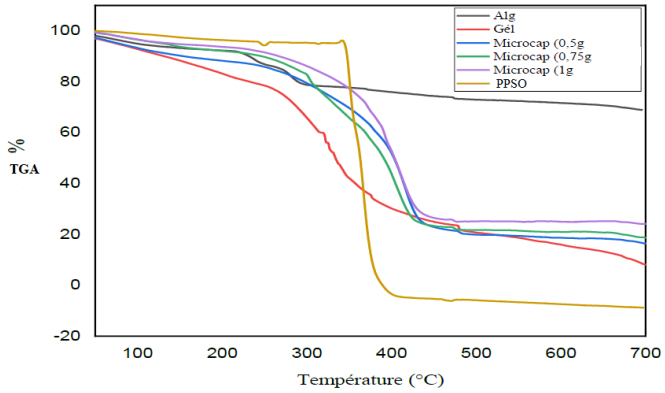

Figure 4. TGA thermal analysis of PPSO (oil), Alg (alginate), Gel (gelatin), and microcapsules (0.5, 0.75, and 1 g PPSO)

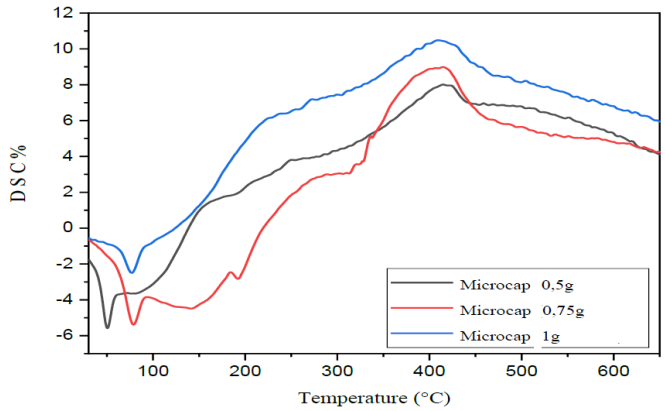

Figure 5. DSC analysis curves of microcapsules containing 0.5, 0.75, and 1 g of PPSO.

3.4. Controlled Release Kinetics

Figure 6 presents the release profile of the encapsulated oil from microcapsules containing 0.75g of oil in three media simulating different physiological conditions: an acidic pH (pH 1.2– Simulated Gastric Fluid, SGF), an intestinal pH (pH 6.8– Simulated Intestinal Fluid, SIF), and a colonic pH (pH 7.4– Phosphate Buffer Solution, PBS). The release kinetics show two distinct phases: Initial Phase (0 to 200 minutes): A rapid burst release is observed at pH 6.8 and 7.4, primarily attributed to the diffusion of loosely retained or surface-adsorbed oil from the polymeric matrix. This behavior is typical of biopolymeric systems encapsulating essential oils, as reported by Abd El-Mageed et al. (2022), who observed an initial rapid release due to weak surface interaction between the oil and the polymers [18]. Prolonged Phase (400 to 1440 minutes): The release becomes slower and more controlled, particularly at pH 6.8 and 7.4. This is explained by a gradual disintegration of the alginate-gelatin network under the influence of the physiological pH, enabling a more targeted and sustained release of the encapsulated oil. This mechanism is consistent with the work of Arfat et al. (2021), who showed that alginate-gelatin-based systems ensure protection in the gastric environment and adapted release under intestinal conditions [20]. At pH 1.2, the release remains relatively low throughout the experiment, highlighting the gastroprotective capacity of the matrix, which remains compact and poorly permeable in the acidic medium. This stability is reinforced by the high encapsulation efficiency observed (93.51%), indicating that the encapsulating system is suitable for protecting the oil in the gastric environment while permitting a controlled release in the intestinal and colonic areas, as desired for targeted oral applications.

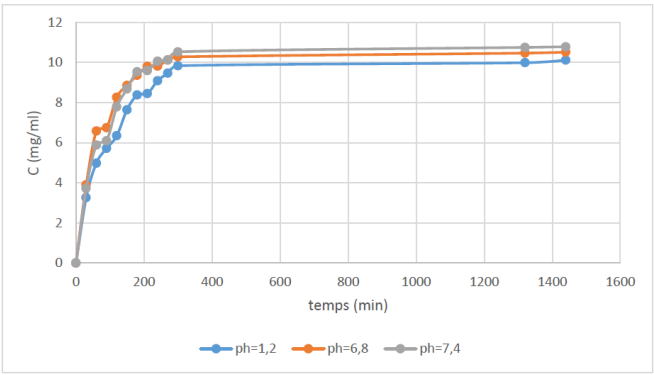

Figure 6. Release profile of the 0.75 g microcapsules in different pH media

IV. Conclusions

This study demonstrated the successful encapsulation of prickly pear seed oil using an alginate–gelatin biopolymeric matrix through the complex coacervation technique. The encapsulation process effectively protected the oil's sensitive bioactive compounds and significantly improved its thermal stability. Among the tested formulations, the microcapsules containing 0.75 g of PPSO exhibited the best compromise between encapsulation efficiency, thermal performance, and

controlled release behavior. Release studies confirmed the gastroprotective nature of the matrix under acidic conditions and its ability to provide sustained release in intestinal environments. These results suggest that alginate–gelatin microcapsules represent a promising strategy for stabilizing and controlling the delivery of PPSO in functional food, cosmetic, and pharmaceutical applications.

***References**:*

1. Ghosh, S., & Basu, S. (2020). Microencapsulation: A novel approach for food ingredient protection and delivery. Food Bioscience, 33, 100494.
2. Jafari, S. M. (2017). Microencapsulation Technologies for the Food Industry. Academic Press.
3. McClements, D. J. (2015). Nanoparticle- and microparticle-based systems for encapsulating and delivering bioactive components: structural design and functional performance. Advanced Materials, 27(38), 5894-5909.
4. Fang, Z., et al. (2022). Biopolymer microencapsulation: A review on the recent advances in preparation and applications. Journal of Applied Polymer Science, 139(25), 52277.
5. Turabi, P., et al. (2018). Complex coacervation as an encapsulation technique for delivery of functional components. Trends in Food Science & Technology, 77, 104-114.
6. Ye, Q., & George, P. (2021). Gelatin-alginate based microcapsules for drug and bioactive delivery. International Journal of Biological Macromolecules, 182, 1904-1915.
7. Ahmed, T. A., et al. (2022). Structural and thermal behavior of oil-loaded gelatin–alginate microcapsules for oral delivery. Food Hydrocolloids, 134, 108021.
8. Alimi, H., et al. (2023). Chemical composition and biological activities of prickly pear (Opuntia ficus-indica) seed oil: A review. Industrial Crops and Products, 198, 116670.
9. Ennouri, M., et al. (2020). Nutritional and therapeutic interest of prickly pear (Opuntia ficus-indica) oil. European Journal of Lipid Science and Technology, 122(7), 1900138.
10. Erçelebi, E. A., & Uslu, M. K. (2021). Oxidative stability of vegetable oils: A review of mechanisms, influencing factors, and protection strategies. LWT - Food Science and Technology, 148, 111660.
11. Rahim. M.A, Imran. M, Khan. M.K, Ahmad. M.H, Ahmad. R.S. Impact of spray drying operating conditions on encapsulation efficiency, oxidative quality, and sensorial evaluation of chia and fish oil blends, Journal of food processing and preservation, 45(12),16248,2021.
12. Le, N. T. A. Upcycling of fruit processing byproducts for enhancing food Preservation and delivery, thèse de doctorat, Nanyang Technological University, Singapore, 2024. https://hdl.handle.net/10356/183067
13. Roy. S, Min. S.J, Rhim. J. W. Essential Oil-Added Chitosan/Gelatin-Based Active Packaging Film: A Comparative Study. Journal of composite Materials, 57(7), 126-136, 2023.
14. Bellache. R, Hammiche .D, Boukerrou .A et al. Prickly pear seed oil (PPSO) encapsulated by biodegradable polymer Poly-hydroxy-butyrate-co-valerate (PHBV).Materials Today: Proceedings, 78(3), 2022.
15. Figueroa-Enriquez. C, Rodríguez-Félix. F, Castro. D, Nunez. D. Coating of Sodium Alginate with gelatin Nanoparticles and Pitaya Extract (Stenocereus thurberi): Physicochemical and Antioxidant Properties. Wiley, Journal of Food Quality, 2025.
16. Susiany. L, Lucciano. B, Preparation and characterization of alginate and gelatin microcapsules containing Lactobacillus Rhamnosus. Anais da Academia Brasileira de Ciências 89(AHEAD), 2017.
17. Martinović, J.; Ambrus, R.; Planinić, M.; Šelo, G.; Klarić, A.-M.; Perković, G.; Bucić-Kojić, A. Microencapsulation of Grape Pomace Extracts with Alginate-Based Coatings by Freeze-Drying: Release Kinetics and In Vitro Bioaccessibility Assessment of Phenolic Compounds. Gels 2024, 10, 353. https://doi.org/10.3390/gels10060353
18. Otálora. M. C, Wilches-Torres. A, Gómez Castaño. J.A. Spray-Drying Microencapsulation of Andean Blueberry (Vaccinium meridionale Sw.) Anthocyanins Using Prickly Pear (Opuntia ficus indica L.) Peel Mucilage or Gum Arabic: A Comparative Study. Foods, 12, 1811, 2023.
19. Abd El-Mageed. M. M, et al. Encapsulation of essential oils using biopolymeric systems for controlled release in gastrointestinal tract. Journal of Molecular Liquids, 357, 119102, 2022.
20. Arfat. Y. A, et al. Biopolymer-based encapsulation of natural bioactives for targeted delivery in the gut: A review. Food Hydrocolloids, 113, 106461,2021.

Biopolymer Applications Journal
e-ISSN : 2800-1729

Kaci CHALAH et al. Vol 5. N°1, 2026, pp. 33-38

Rheological Behavior of Polymeric Drilling Fluids: A Comparative Study of Carboxymethyl Cellulose, Polyanionic Cellulose, Hydroxyethyl Cellulose, and Xanthan Gum.

Kaci CHALAH[1*]; Imed BENNOUI[1]; Imed BEGHOURA[1]; Dalila HAMMICHE[2]; Abdelbaki BENMOUNAH[3]

1: National Centre for Integrated Studies and Research in Building, 16097 Souidania, Algiers, Algeria.
2: Université de Bejaia, Faculté de Technologie, Laboratoire des Matériaux Polymères avancés, 06000 Bejaia, Algérie.
3: University of Boumerdes, Materials, Processes and Environment Research Unit, 26000 Boumerdes, Algeria.
**Corresponding author: kaci.chalah@yahoo.fr*
Received: 28 October 2025; Accepted: 17 December 2025; Published: 15 January 2026;

Abstract

The use of water-soluble polymers has increased significantly in many industrial fields. Cellulosic polymers such as carboxymethyl cellulose high viscosity (CMC HV), polyanionic cellulose (PAC R), and hydroxyethyl cellulose (HEC), along with the biopolymer xanthan gum (XG), are widely used to increase the viscosity of drilling fluids. This study analyzes and compares the rheological behavior of aqueous solutions based on these viscosifiers at a concentration of 0.4 wt. %. The results showed that only the XG solution exhibited viscoplastic behavior. While the CMC HV, PAC, and HEC solutions exhibited pseudoplastic (shear-thinning) behavior, the HEC solution displayed a high degree of shear thinning. The apparent viscosities measured at a shear rate of 10 1/s were 0.526, 0.268, 0.153, and 0.050 Pa.s for XG, HEC, PAC and CMC HV, respectively. At a high shear rate of 500 1/s, the apparent viscosities were comparable: 0.026 Pa.s for XG, 0.054 Pa.s for HEC, 0.029 Pa.s for PAC, and 0.025 Pa.s for CMC.

Keywords: *Biopolymer drilling fluids, Rheological models, Apparent viscosity, yield stress.*

I. Introduction

Water-soluble polymers (WSPs), whether natural or synthetic, dissolve in water and modify the physical properties of aqueous systems. WSPs are often used in small quantities as thickeners, stabilizers, and flocculants in numerous applications [1]. For example, polyacrylamides are commonly used as flocculants in wastewater treatment and in the oil recovery industry, while polyacrylic acids are used as cement modifiers [2]. Polymers such as polyethylene glycol, polypropylene glycol and polyvinylpyrrolidone are used in the pharmaceutical industry [3] and as emulsion stabilizers and thickeners [4, 5].

Polymer viscosifiers are widely used in water-based drilling fluid (WBDF) and for enhanced oil recovery (EOR) operation to increase the viscosity of fluids. Various types, such as methylcellulose, carboxymethyl cellulose (CMC), Polyanionic cellulose (PAC) hydroxyethyl cellulose (HEC), partially hydrolyzed polyacrylamide (PHPA) hydroxypropyl methyl cellulose, and xanthan gum (XG) [6] are used in the oil industry. In WBDFs, WSPs are often used to replace bentonite or as a supplement to improve fluid viscosity. For instance, XG and HEC have been used to improve the rheological properties of WBDFs [7]. Ouaer and Gareche [8], Benyounes et al. [9] investigated the effect of HEC concentration on the rheological properties of WBDF. In another study, de Aguiar et al. [10] confirmed the potential use of polymer (PHPA) as viscosifying agent for EOR.

Polymeric viscosifiers differ from each other in their origin (natural, modified, synthetic), ionic nature (charged and uncharged), molecular mass, structure (linear, branched, cross-linked), etc. The molecular mass influences properties like viscosity, chain entanglement, and solution stability.

Structurally, polymers are classified as linear, branched, or cross-linked networks [11]. Linear polymers, which consist of a single chain of monomers, include natural rubber, elastomers, CMC, PHPA, and HEC, and are often characterized by high elasticity [12-14]. A chain of branched-chain links has side branches, for example, amylopectin, starch, and xanthan gum [15].

Even though the viscosifying polymers have high molecular weight, many differences exist: some are linear, others are branched, some are charged, others are not charged, some have functional groups, others do not have. Previous investigations into the rheology of WSP solutions have not included a direct comparison of the key polymers used in WBDFs. Therefore, to facilitate appropriate polymer selection and to better understand the performance of WSPs in drilling fluid applications, a rheological characterization is necessary. This investigation, therefore, aims to study the effect of water-

soluble polymer type (XG, HEC, PAC R and CMC HV) on the rheological properties. Then, a comparative analysis between these different polymers will be established.

II. Material and methods

Water-soluble polymers

Xanthan gum (XG) is a biopolymer produced by the bacterium Xanthomonas campestris through a fermentation process. XG is a water-soluble polymer with high molecular weight, and serves as a thickener, stabilizer, and viscosity modifier.

Hydroxyethyl cellulose (HEC) is a synthetic polymer derived from cellulose, created by chemically reacting insoluble cellulose with ethylene oxide. HEC is as a water-soluble polymer derived from cellulose, used as a binder and thickening agent. HEC is a biodegradable polymer, known for its biocompatibility and non-toxicity. The HEC used in this study is a commercial product, which is used by the oil companies.

Both carboxymethyl cellulose high viscosity (CMC HV) and Polyanionic Cellulose premium-grade (PAC R) are modified polymers derived from cellulose. CMC HV and PAC R are obtained by treating the insoluble cellulose with chloroacetic acid, to introduce carboxymethyl groups onto the cellulose backbone. Both of cellulose-derived products differ from each other in their degree of modification and specific applications. PAC R is an anionic cellulose ether with a high degree of polymerization and substitution. The Table 1 provides information on the properties of polymers, such as their physical and chemical characteristics.

Preparation and measurement

WSPs solutions were prepared according to the method described in a previous study [16]. Solutions were prepared by gradually adding biopolymer powder to water while agitating to prevent the formation clumps and ensure proper dispersion. According to the WSP type, four suspensions were prepared with a concentration of 0.4 wt. %; this concentration is commonly used to formulate water-based fluid formulations [17].

The rheological measurements were performed at 20°C using a controlled stress rheometer AR 2000 (Figure 2) from TA instruments using the concentric cylinder measuring system. The rheometer equipped with Couette geometry measures fluid properties by rotating the bob coaxial cylinder, while the cup cylinder remains stationary.

In order to avoid any memory effect, the sample was pre-sheared at 100 1/s for 60 s after loading in the measuring device. The sample was then kept at rest for 600 s before measurements to allow the material to recover its initial structure. The imposed shear rate ranges from 0 to 700 1/s. A ramp of 0.2 Pa to 300 Pa during 600 s has been applied.

Rheological models

The Herschel-Bulkley (H-B) model is a generalized equation characterized by three parameters: consistency (k), flow index (n), and yield shear stress (τ_0). H-B fluid requires an initial yield stress to be exceeded before flow starts. Classically, the model of Herschel-Bulkley was used to fit the shear rate dependence of the shear stress of WBDF [7, 18]. Moreover, this model can well simulate the rheological properties of cement paste [19]. Therefore, experimental data were fitted to the classical model of Herschel–Bulkley (Eq. 1):

$$\tau = \tau_0 + \mathrm{K}.\dot{\gamma}^n \qquad \text{(Eq. 1)}$$

where τ_0 is the yield stress, if τ_0 is equal to 0, this equation is equivalent to the Power Law model. The consistency index is designed by K letter, the higher value represents the more viscous material, and n is the flow behavior index (power law exponent) giving a measure of the pseudoplasticity. this parameter (n) indicates a degree of dependence of viscosity on the shear rate.

Table 1. Physicochemical properties of the water-soluble polymers studied.

Characteristics	Xanthan gum	HEC	PAC R	CMC HV
Origin	natural	Modified	Modified	Modified
Structure	branched	linear	linear	linear
Nature	charged	uncharged	charged	charged
R groups	$-COO^-$ $-COCH_3$	H/CH_2CH_2OH	H/CH_2COONa	H/CH_2COONa
Stiffness of chains	semi-rigid	rigid	semi-rigid	flexible
molecular weight [g/mol]	1×10^6 to 2×10^6	$9.5x10^5$	$7x10^5$	$7x10^5$
functional groups	acetyl groups carboxylic groups	hydroxyethyl	carboxymethyl groups	carboxymethyl groups
Solubility	Water	Water	Water	Water
degree of substitution	/	1	07 – 1.2	0.65 - 0.75
pH (1 % solution)	6-7	6-8.5	6.0 to 8.0	6.0 - 8.0

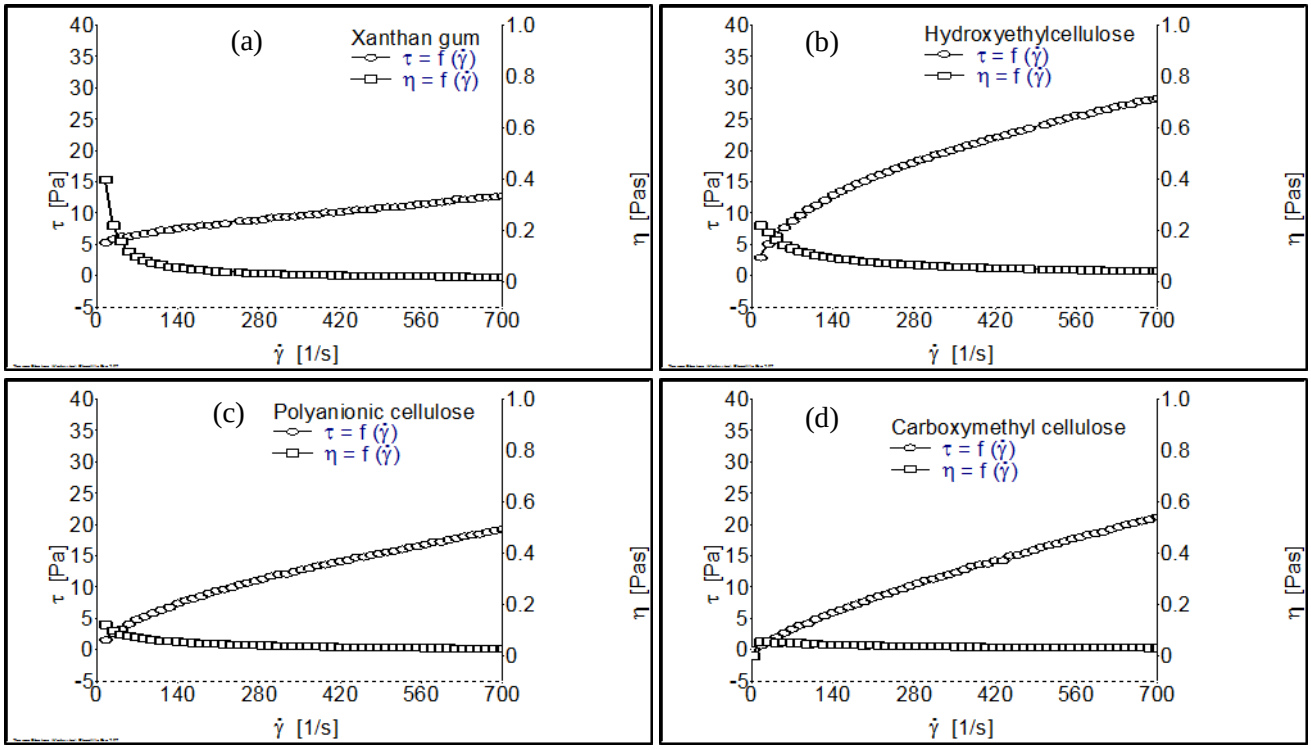

Figure 1. Shear stress (τ) and apparent viscosity (η) as a function of shear rate (γ̇): (a) xanthan gum solution, (b) hydroxyethyl cellulose solution, (c) polyanionic cellulose solution and (d) carboxymethyl cellulose solution.

III. Results and discussion

Rheological behavior

The rheological curves of WSPs (XG, HEC, PAC and CMC HV) are shown in Figure 1. The shear stress and apparent viscosity as a function of shear rate of XG mixture at 0.4 wt. % is presented in Figure 1-a.

In contrast to the XG solution, the shear stress as a function of shear rate curve (Figure 1-b) displays the pseudoplastic behavior of the HEC-water system. This figure shows that the solution based on HEC exhibits pseudoplastic behavior. Therefore, experimental data were fitted to the model of Ostwald–De Waele Model [20]. In addition, the flow curve for the studied mass concentrations of CMC HV and PAC R clearly shows a non-Newtonian behavior without a yield stress (pseudoplastic behavior) as shown in in Figure 1-c and 1-d.

The flow curves of WSPs are exhibited in Figure 2. The H-B and Ostwald-de Waele models ($\tau_0 = 0$) were used to fit the shear rate dependence of the shear stress curves of WSPs solutions at 0.4 wt. % to verify the existence of the yield stress. The flow curves of PAC R, CMC HV and HEC show that these solutions behave as pseudoplastic fluids. A pseudoplastic fluid is a non-Newtonian fluid whose viscosity decreases with increasing shear rate. This behavior is characteristic of fluids without a yield stress. This property causes pseudoplastic fluids to exhibit lower viscosity at higher shear rates and higher viscosity at lower shear rates.

Table 2 presents the parameters as results of the fitting process by the H-B model of flow curves. In the case of the XG solution, the fitted parameter yield stress (τ_0) was 4.6 Pa. The flow curve of XG solution was found to be well fitted by H–B model (r = 0.999). On the contrary, the flow behavior of HEC, PAC R and CMC HV solutions did not indicate yield stress. Thus, flow curves were fitted by the Ostwald–de Waele equation.

With regard to the flow behavior index (n), the XG, HEC, PAC R and CMC HV solutions presented values of 0.623 [Pa.s^n], 0.496 [Pa.s^n], 0.589 [Pa.s^n], and 0.780 [Pa.s^n], respectively. It is obvious that WSPs show a pseudoplastic behavior with a flow behavior index less than 1 ($n < 1$). The pseudoplasticity of PAC R (n = 0.589) was greater than that of CMC HV (n = 0.780). Thus, CMC HV's chains are the easiest to orient under the effect of shearing compared to other HSPs (HEC and PAC R). McMullen et al. [20] confirmed that the CMC HV and HEC aqueous systems displayed shear-thinning behavior without yield stress.

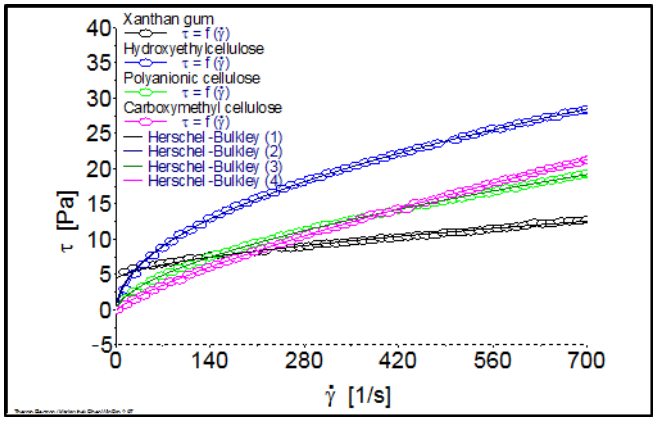

Figure 2. Shear stress (τ) of water-soluble polymers, the continuous solid lines correspond to the curve fitting to the H-B model.

Table 2. Rheological parameters values according to H-B and Ostwald-de Waele models.

water-soluble polymer	Rheological model	Parameters values
Xanthan gum	Herschel-Bulkley	$\tau_0 = 4.6$ [Pa] K = 0.134 [Pa.s^n] n = 0.623
HEC	Ostwald-de Waele	$\tau_0 = 0$ K = 1.103 [Pa.s^n] n = 0.496
PAC R	Ostwald-de Waele	$\tau_0 = 0$ K = 0.405 [Pa.s^n] n = 0.589
CMC-HV	Ostwald-de Waele	$\tau_0 = 0$ K = 0.130 [Pa.s^n] n = 0.780

Edali et al [21] confirmed that pseudoplasticity is higher in both high molecular weight and DS (when the DS is 0.9 to 1.2). On the other hand, the HEC solution was more pseudoplastic compared to the CMC HV and PAC R solutions. The pronounced shear-thinning behavior of the HEC solution is attributed to its rigid chains.

The XG solution is known for its viscoplastic behavior. The existence of the yield stress (τ_0 = 4.6 Pa), as pointed out in the table 2 (XG solution), indicates that the XG solution is viscoplastic. Yield stress refers to the minimum shear force at which the polymer structure is destroyed, initiating flow. This behavior can reflect the strength of the network structure and is related to the network density of the XG [22].

the HEC solution showed the highest consistency index (k = 1.103 Pa·s^n) which relatively indicates high viscosity. The consistency index of XG, PAC R and CMC HV were 0.134, 0.405 and 0.130 Pa.s^n, respectively.

Apparent viscosity

This section discusses the relationship between apparent viscosity and shear rate, the Cross rheological model is used to provide a more comprehensive understanding of the rheological properties of WSPs. The apparent viscosity as a function of shear rate for polymer solutions are presented in Figure 3. The Cross model demonstrated a good fit with high correlation coefficient (r-value) to the observed apparent viscosity/ shear rate data of WSPs solutions.

Chalah et al. [16] reported that the Ostwald-de Waele and Cross models are in good agreement with experimental data for concentrations ranging from 0.7 to 1.7 % CMC-HV. The correlation coefficient value is greater than 0.999 for both the Ostwald-de Waele and Cross models. However, Salehi et al. [23] showed that the Ostwald–de Waele model is suitable to explain the rheological behavior of CMC HV solution. They indicated that the Power law equation demonstrated a good fit. On the other hand, Ouaer and Gareche [8] reported that the flow curves of HEC solutions are well fitted by the Cross model. The Cross model gave good ability to predict the flow behavior of HEC.

The apparent viscosities measured at low shear rate (10 1/s) were 0.526, 0. 0.268, 0.153 and 0.050 Pa.s for XG, HEC, PAC R and CMC HV, respectively. Subsequently, the apparent viscosities evaluated at a high shear rate (500 s^{-1}) were 0.026, 0.054, 0.029 and 0.025 Pa.s for XG, HEC, PAC R and CMC HV, respectively. Results showed that the apparent viscosities of XG and HEC solutions decreased rapidly with increasing shear rate. However, the phenomenon is less pronounced in the case of solutions based on PAC R and CMC HV. It is clear that the apparent viscosity of PAC R was significantly higher than that of CMC HV at low shear rates (> 100 1/s). Indeed, the functional properties of CMC HV depend on the degree of substitution of the cellulose structure, as well as the chain length of the cellulose backbone structure and the degree of clustering of the carboxymethyl substituents. From this point of view, the degree of substitution of PAC R is higher than that of CMC, which ensures better viscosity. Thus, PAC R macromolecules are generally considered to be stiffer than CMC HV macromolecules. In addition, the apparent viscosity of HEC solution was found to be significantly higher than PAC R and CMC-HV aqueous systems.

At high shear rates (210-700 1/s), XG, CMC HV, and PAC R all exhibit similar flow behavior where their flow curves are superimposed, indicating similar viscosity levels under these specific shear conditions. In contrast, Hydroxyethyl Cellulose (HEC) shows a higher flow curve, suggesting it maintains a higher viscosity compared to XG, CMC HV, and PAC R at the same high shear rates.

The rheological differences between WSPs determine their effectiveness and application in fluids. The anionic modified CMC HV and PAC R identified as pseudoplastic polymers, are used mainly in drilling muds in low-temperature drilling applications. Although PAC R is superior to CMC HV in filtration reduction, anti-salt, anti-collapse and high temperature resistance [24, 25]. PAC R have a higher and more uniform DS than CMC HV, resulting in better water solubility and more stable performance in solution. Economically, CMC HV and PAC R are generally more cost-effective than XG, known as an anionic natural polymer. However, XG offers superior thickening and stabilizing properties due to its viscoplastic behavior. From its neutral nature, HEC behavior is less affected by the salt content, which makes it stable in high salinity fluids. In addition, the choice of viscosifier

depends strongly on the shear rate, especially at low shear rates. XG exhibits a very high viscosity at shear rates ranging from 0 to 40 1/s due to intermolecular forces like ionic interactions and macromolecular entanglement. While, thanks to the rigidity of its chains, the HEC solution showed high viscosity at low shear rate.

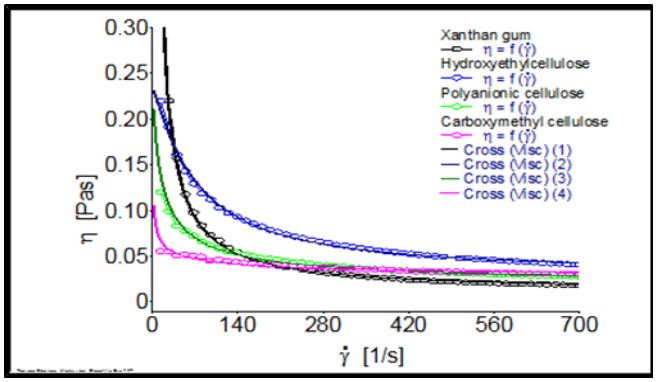

Figure 3. Apparent viscosity (η) of water-soluble polymers, the solid continuous lines correspond to the curve fitting.

IV. Conclusions

The rheological properties of four different water-soluble polymers were investigated. The experimental data were well fitted using the H-B and Ostwald-de Waele models. Knowledge of rheological properties such as rheological behavior, degree of shear-thinning, and viscosity is crucial for the selection and application of viscosifying polymers. The obtained results confirmed that:

1. The HEC, PAC R and CMC HV solutions showed pseudoplastic behavior at a concentration of 0.4 wt. %. However, even at a relatively low concentration (0.4 wt. %) XG solution behaved as a viscoplastic material, with a yield stress of 4.6 Pa.

2. The HEC solution (n = 0.496) is characterized by a higher degree of shear-thinning than PAC R (n = 0.589) and CMC HV (n = 0.780) solutions; the pseudoplasticity of HEC is highly pronounced.

3. At low shear rates, XG and HEC solutions showed higher apparent viscosity than CMC HV and PAC R solutions.

4. At high shear rates (200 to 700 1/s), the apparent viscosity of the WSPs is relatively low. Nevertheless, it should be noted that the HEC flow curve remains higher than the other curves (XG, CMC HV and PAC R).

References:

1. E.C. Tarring, I. Durance, M.J. Harbottle, R. Lucas, D.S. Read, B.D. Ward Water-soluble polymers: emerging contaminants detected, separated and quantified by a novel GPC/MALDI-TOF method. Environmental Pollution 340, 122888, 2024.

2. K. Chalah, A. Benmounah, M. H. Mahdad, A. Akkouche, A. Hammas. Compatibility of Slag-Blended Cement with Polycarboxylate Ether Superplasticisers: Rheological Properties Study. Journal of Materials and Engineering Structures, 8 (3), 315-324, 2021.

3. V.G. Kadajji, G.V. Betageri. Water soluble polymers for pharmaceutical applications. Polymer Journal 3(4), 1972–2009, 2011.

4. A.K. Badawi, R.S. Salama, M.M.M. Mostafa. Natural-based coagulants/flocculants as sustainable market-valued products for industrial wastewater treatment: a review of recent developments. RSC advances, 13(28), 19335-19355, 2023.

5. U. Rozman, G. Kalčíková. The first comprehensive study evaluating the ecotoxicity and biodegradability of water-soluble polymers used in personal care products and cosmetics. Ecotoxicology and environmental safety 228, 113016, 2021.

6. A. Wang, W. Wang. Gum-g-copolymers: synthesis, properties, and applications. In Polysaccharide based graft copolymers. Berlin, Heidelberg: Springer Berlin Heidelberg; pp. 149-203; 2013.

7. K. Chalah, A. Benmounah, K. Benyounes. Effect of anionic polyelectrolytes on the flow of activated sodium bentonite drilling mud. In MATEC Web of Conferences, EDP Sciences, 149, 01082, 2018.

8. H. Ouaer, M. Gareche. The rheological behaviour of a water-soluble polymer (HEC) used in drilling fluids. Journal of the Brazilian Society of Mechanical Sciences and Engineering 40(8), 380, 2018.

9. K. Benyounes, S. Remli, A. Benmounah. Rheological behavior of hydroxyethylcellulose (HEC) solutions. In Journal of Physics: Conference Series, IOP Publishing, 1045(1), 012008, 2018.

10. K. L. N. P. de Aguiar, L. C. M. Palermo, C. R. E. Mansur. Polymer viscosifier systems with potential application for enhanced oil recovery: A review. Oil & Gas Science and Technology–Revue d'IFP Energies nouvelles, 76, 65, 2021.

11. M. Steube, T. Johann, R. D. Barent, A. H. Mueller, H. Frey. Rational design of tapered multiblock copolymers for thermoplastic elastomers. Progress in Polymer Science,124, 101488, 2022.

12. S. B. Hamed, M. Belhadri. Rheological properties of biopolymers drilling fluids. Journal of Petroleum Science and Engineering 67(3-4), 84-90, 2009.

13. J. Liu, Z. Dai, K. Xu, Y. Yang, K. Lv, X. Huang, J. Sun. Water-based drilling fluid containing bentonite/poly(sodium 4-styrenesulfonate) composite for ultrahigh-temperature ultradeep drilling and its field performance. SPE Journal 25(03), 1193-1203, 2020.

14. S. Xia, L. Zhang, A. Davletshin, Z. Li, J. You, S. Tan. Application of poly-saccharide biopolymer in petroleum recovery. Polymers 12(9), 1860, 2020.

15. J.K.M. William, S. Ponmani, R. Samuel, R. Nagarajan, J.S. Sangwai. Effect of CuO and ZnO nanofluids in xanthan gum on thermal, electrical and high pressure rheology of water-based drilling fluids. Journal of Petroleum Science and Engineering, 117, 15-27, 2014.

16. K. Chalah, A. Benmounah, M.H. Mahdad, R. Kheribet. Rheological study of sodium carboxymethylcellulose: Effect of concentration and molecular weight. Materials Today: Proceedings 53(1), 185-190, 2022.

17. H. Ouaer, M. Gareche. Hydroxyethyl cellulose as a rheology modifier for water-based drilling fluids formulated with Algerian bentonite. Journal of the Brazilian Society of Mechanical Sciences and Engineering 41(3), 123, 2019.

18. A. Akkouche, A. Benmounah, A. Gueciouer and K. Chalah. Valorization of mixed metal hydroxide on Algerian Na-Bentonite suspensions: Application to water-based drilling fluid. Egyptian Journal of Petroleum 29(2), 127–131, 2020.

19. K. Chalah, A. Benmounah, R. Kheribet, A. Akouche. Effect of silica fume on cement rheology properties in presence of superplasticisers. Materials Today: Proceedings 58, 1246-1250, 2022.

20. R.L. McMullen, S. Ozkan, T. Gillece. Physicochemical Properties of Cellulose Ethers. Cosmetics 9(3), 52, 2022.

21. M. Edali, M.N. Esmail, G.H. Vatistas. Rheological properties of high concentrations of carboxymethyl cellulose solutions. Journal of Applied Polymer Science 79(10), 1787-1801, 2001.

22. Sun, Y., Wang, Y. Study on Rheological Properties of Different Brands of Grease. In Journal of Physics: Conference Series 1300(1), 012113, IOP Publishing 2019.

23. F. Salehi, M. Inanloodoghouz, M. Karami. Rheological properties of carboxymethyl cellulose (CMC) solution: Impact of high intensity ultrasound. Ultrasonics Sonochemistry 101, 106655, 2023.

24. P. Yang, T. B. Li, M. H. Wu, X. W. Zhu, X. Q. Sun. Analysis of the effect of polyanionic cellulose on viscosity and filtrate volume in drilling fluid. Materials Research Innovations 19(sup5), S5-12-S5-16, 2015.

25. Z. Ganghui. Preparation of polyanionic cellulose with excellent performance. Petroleum Drilling Techniques 33(3), 36, 2005.

Biopolymer Applications Journal **Youcef MEHIR et al. Vol 5. N°1, 2026, pp. 39-51**
e-ISSN : 2800-1729

Orthotropic Elastic Characterization of FDM PLA via Multi-axial Mechanical Testing

Youcef MEHIR [1*]; Abdelkader BENAOUALI [1]; Yacine BENABID [1]; Adel BELATTAR [1]; Ahmed SALMI [1]; Iskander Med Aimen BELHOUT [1]

1: Mechanical Systems Design Laboratory, Ecole Militaire Polytechnique, Algiers, Algeria
Corresponding author: mehir.youcef.emp@gmail.com*
Received: 4 November 2025; Accepted: 19 December 2025; Published: 18 January 2026;

Abstract

This study investigates the orthotropic elastic behavior of Polylactic Acid (PLA) manufactured using Fused Deposition Modeling (FDM). According to ISO 527-2 and ASTM standards, standardized tensile and shear specimens were printed along the X, Y, and Z axes. A Box–Behnken Design of Experiments (DoE) was employed to investigate the influence of three key process parameters on the mechanical response: layer thickness, raster width, and printing speed. Directional Young's moduli (Ex, Ey, Ez) and shear moduli (Gxy, Gyz, Gzx) were obtained through mechanical testing. The results revealed a pronounced anisotropy induced by the layer-by-layer deposition process. We used the experimental data to make the full elastic stiffness matrix for the PLA, which is an orthotropic material. Statistical analysis (ANOVA) confirmed that process parameters had the biggest effect on changes in stiffness. The results give us a lot of information that we can use to model printed PLA parts in finite element simulations and help us come up with better ways to design 3D printed parts that work well mechanically.

Keywords: *Additive Manufacturing, Anisotropy, Design of Experiments, FDM, Polylactic Acid.*

I. Introduction

Additive manufacturing (AM) has emerged as one of the most transformative manufacturing technologies of the past two decades. It is used in the aerospace, automotive, and biomedical fields[1]. In contrast to traditional subtractive methods, which take material away from a solid block, AM makes parts by adding material layer by layer. This method makes it feasible to make very complicated shapes that are hard or even impossible to make with machining, casting, or other standard manufacturing methods. Fused Deposition Modeling (FDM) is the most popular of the different AM technologies, such as Stereolithography (SLA) and Selective Laser Sintering (SLS). This popularity is attributed to its cost-effectiveness, process flexibility, ease of implementation, and compatibility with a wide range of thermoplastic polymers [2]. The layer-by-layer deposition method, However, the layer-by-layer deposition process inherently induces anisotropic mechanical, which means that the mechanical characteristics change depending on how the object is oriented [3].

The increasing use of AM has also changed how designs are made, especially by adding topology optimization (TO) to the design-for-additive-manufacturing (DfAM) technique [4]. TO's goal is to create structures that are both lightweight and mechanically efficient by spreading out the material in the best way possible within a particular design space. In this regard, numerous studies have underscored the significance of considering the anisotropic behavior of additive manufacturing (AM) materials during TO. Xu et al[5] illustrated the advantages of hybrid deposition strategies in enhancing the strength of FDM-manufactured structures, whereas Zou and Xia[6] underscored the necessity of incorporating anisotropic strength constraints to more accurately represent the actual performance of printed components. In the same way, Zhou et al [7] added the effects of build orientation to multi-component TO frameworks, which made AM constructions more mechanically reliable. These advancements exemplify the convergence of AM and TO, since AM's ability to produce intricate geometries inherently complements the advanced designs created by TO [8, 9].

In addition to design factors, the mechanical properties of FDM products are quite sensitive to process parameters such as layer thickness, raster width, and printing speed. Changes in these factors have a direct effect on the final product's stiffness, strength, and level of anisotropy. This dependence has spurred significant research initiatives aimed at quantifying and modeling the relationship between printing conditions and material properties [10-12]. Establishing predictive correlations is particularly advantageous since it allows designers to foresee the performance of printed structures and adjust process settings accordingly. In this respect, the current study examines the elastic orthotropy of FDM-manufactured PLA, aiming to deliver a comprehensive characterization of its mechanical behavior under varying

loading situations. The goal is to improve the accuracy and reliability of FDM materials by combining experimental testing and modeling methods. This will help create predictive models that are specific to DfAM applications.

II. General Methodology

1) Orthotropy hypothesis: modeling filament orientation

Parts manufactured by FDM exhibit intrinsically anisotropic mechanical behavior, resulting from the layered nature of the process and the inherent directionality of the material deposition. To accurately capture this behavior, an orthotropic material assumption is commonly adopted, assuming the existence of three orthogonal planes of material symmetry associated with distinct mechanical properties[13,14].

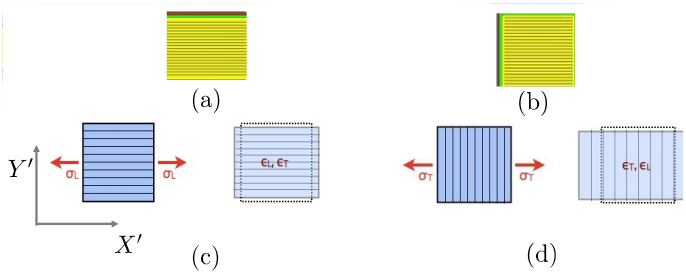

Figure 1 Analogy underlying the orthotropic material assumption: (a) and (b) FDM printing along X' and Y' directions, respectively;

Figure 1 illustrates this analogy by comparing RDs with their equivalent fiber-reinforced composite representations: subfigures Figure 1(a)–(b) show printing along the longitudinal \(X'\) and transverse \(Y'\) directions, while subfigures Figure 1(c)–(d) depict the corresponding composite systems with fibers aligned parallel or perpendicular to \(X'\). This observation confirms that the raster direction (RD) governs the principal axes of orthotropy in FDM-manufactured materials.

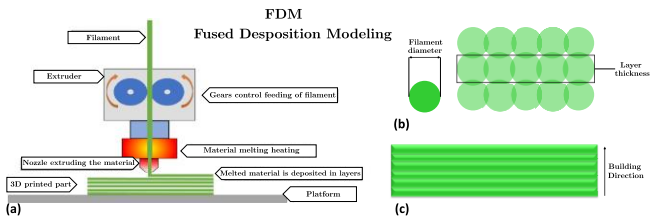

Figure 2(a) FDM process (b) Filament arrangement (c) Layered structure

Accordingly, the material is characterized by three principal directions: the **longitudinal direction** *X'*, aligned with RD and providing the highest stiffness; the **transverse in-plane direction** *Y'*, lying within the layer plane and perpendicular to *X'*; and the **build direction** *Z'* (see **Erreur ! Source du renvoi introuvable.**(c)), normal to the layers and mainly governed by interlayer bonding.

Erreur ! Source du renvoi introuvable. further illustrates the layer-by-layer deposition along Z', where the extruded filament acts as an oriented fiber. This layered architecture produces the anisotropic behavior of FDM components, as confirmed by the microstructures shown in subfigures **Erreur ! Source du renvoi introuvable.**(b)–(c).

Building upon this characterization, the proposed TO formulation incorporates the PSP relationships through a orthotropic model linking the mechanical properties to the RD and the printing parameters.

2) The element stiffness matrix $K_e(\theta, \alpha, \chi)$

The integration of the 3D orientations of the filaments (θ_e, α_e) and the process parameters (χ) as design variables has a direct impact on the element stiffness matrix K_e.

$$K_e = \int_{\Omega_e} B_e^T D_e(\theta_e, \alpha_e, \chi)\, B_e d\Omega_e \qquad (1)$$

The integral presented in Equation (1) is generally not analytically solvable, especially for elements with complex shapes or when the terms of the integrand $(B_e \text{or } D_e)$ vary within the element.

Therefore, numerical integration methods are used, the most common in Finite Element Method being the Gauss–Legendre quadrature.

This method approximates the integral by a weighted sum of the values of the integrand evaluated at specific points, called Gauss points (ξ_i, η_i, ζ_i) in the natural coordinate system of the element, and associated with weights W_i, W_j, W_k.

$$\begin{aligned} K_e = & \\ & \sum_{p=1}^{n_{gp}} \sum_{q=1}^{n_{gp}} \sum_{r=1}^{n_{gp}} W_p W_q W_r \cdot \\ & B_e(\xi_p, \eta_q, \zeta_r)^T \cdot \\ & D_e(\theta_e, \alpha_e, \chi) \cdot \\ & B_e(\xi_p, \eta_q, \zeta_r) \cdot \\ & \det\left(J(\xi_p, \eta_q, \zeta_r)\right) \end{aligned} \qquad (2)$$

where n_{gp} is the number of Gauss points in each direction of the natural coordinate system, and represents the application of this quadrature.

The term $\det\left(J(\xi_p, \eta_q, \zeta_r)\right)$ is the determinant of the Jacobian matrix of the transformation between global and natural coordinates, evaluated at the Gauss point, which appears in the change of variables $d\Omega_e = \det(J) d\xi d\eta d\zeta$. Gauss–Legendre quadrature offers high numerical accuracy while requiring a limited number of integration points, by exactly integrating polynomials up to a certain degree. For example, an n_{gp} point rule exactly integrates a polynomial of degree $2n_{gp} - 1$. The

Gauss points and weights are optimally chosen to achieve this accuracy[15].

a) Orthotropic Material Elasticity Law

With the introduction of a three-dimensional orientation, the full orthotropic model, characterized by three mutually orthogonal planes of material symmetry, is more appropriate to describe the behavior of FDM parts, where the properties may differ significantly along the extrusion direction, the transverse direction in the deposition plane, and the direction perpendicular to the deposition plane (build direction)[15].

- **2D case:**
  For an orthotropic material under plane stresses, the elasticity matrix is given by:

$$D_{2D} = \begin{bmatrix} \frac{1}{E_{X'}} & \frac{-\nu_{X'Y'}}{E_{X'}} & 0 \\ \frac{-\nu_{X'Y'}}{E_{X'}} & \frac{1}{E_{Y'}} & 0 \\ 0 & 0 & \frac{1}{G_{X'Y'}} \end{bmatrix} \quad (3)$$

where $E_{X'}$ and $E_{Y'}$ are the Young's moduli in the principal directions, $\nu_{X'Y'}$ is the principal Poisson's ratio, and $G_{X'Y'}$ is the shear modulus in the plane.

- **3D case:**
  In 3D, the complete orthotropic elasticity matrix is:

$$D_{3D} = \begin{bmatrix} \frac{1}{E_{X'}} & & & & & \\ \frac{-\nu_{X'Y'}}{E_{X'}} & \frac{1}{E_{Y'}} & & & sym & \\ \frac{-\nu_{X'Z'}}{E_{X'}} & \frac{-\nu_{Y'Z'}}{E_{X'}} & \frac{1}{E_{Z'}} & & & \\ & & & \frac{1}{G_{Y'Z'}} & & \\ & 0 & & & \frac{1}{G_{X'Z'}} & \\ & & & & & \frac{1}{G_{X'Y'}} \end{bmatrix} \quad (4)$$

  There are nine independent coefficients: Young's three moduli, Poisson's three coefficients, and the three shear moduli. It is therefore easy to verify that the orthotropic model.

Accurately modeling these dependencies lies at the core of the PSP (χ) relationships $E_i(\chi), G_{ij}(\chi)$.

b) Transformation matrices

- **Transformation for rotation around the z-axis (angle θ)}**

The transformation matrix for a rotation of angle $\boldsymbol{\theta}$ around the $\boldsymbol{Z'}$ axis is:

$$T_\theta = \begin{bmatrix} (\cos\theta)^2 & (\sin\theta)^2 & 0 & 0 & 0 & -2\cos\theta\sin\theta \\ (\sin\theta)^2 & (\cos\theta)^2 & 0 & 0 & 0 & 2\cos\theta\sin\theta \\ 0 & 0 & 1 & 0 & 0 & 0 \\ 0 & 0 & 0 & \cos\theta & \sin\theta & 0 \\ 0 & 0 & 0 & -\sin\theta & \cos\theta & 0 \\ \cos\theta\sin\theta & -\cos\theta\sin\theta & 0 & 0 & 0 & cos^2\theta - sin^2\theta \end{bmatrix} \quad (5)$$

- **Transformation for rotation around the $X'Y'$ plane (angle α)**

Similarly, for a rotation of angle $\boldsymbol{\alpha}$ around the X' axis:

$$T_\alpha = \begin{bmatrix} 1 & 0 & 0 & 0 & 0 & 0 \\ 0 & (\cos\alpha)^2 & (\sin\alpha)^2 & -2\cos\alpha\sin\alpha & 0 & 0 \\ 0 & (\sin\alpha)^2 & (\cos\alpha)^2 & 2\cos\alpha\sin\alpha & 0 & 0 \\ 0 & \cos\alpha\sin\alpha & -\cos\alpha\sin\alpha & (\cos\alpha)^2 - (\sin\alpha)^2 & 0 & 0 \\ 0 & 0 & 0 & 0 & \cos\alpha & \sin\alpha \\ 0 & 0 & 0 & 0 & -\sin\alpha & \cos\alpha \end{bmatrix} \quad (6)$$

The correct combined transformation depends on the order of rotations and the exact definition of the coordinate systems see **Erreur ! Source du renvoi introuvable.**. The strains $\varepsilon'' = T_\alpha \varepsilon'$ and $\varepsilon' = T_\theta \varepsilon$, then $\varepsilon'' = T_\alpha T_\theta \varepsilon$. The global stress–strain relationship $\sigma = D_e \varepsilon$ is obtained from the local law $\sigma'' = D_e \varepsilon''$ via:

$$D_e(\theta_e, \alpha_e) = T_{\alpha_e} T_{\theta_e} D_e {T_{\theta_e}}^T {T_{\alpha_e}}^T \quad (7)$$

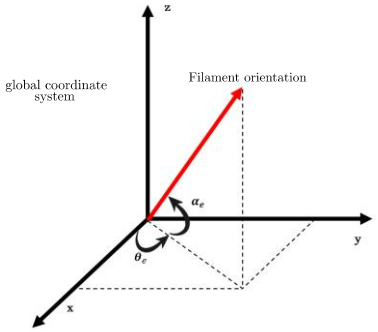

Figure 3 Three-dimensional coordinate transformation

The methodology employed in this study is on capturing and simulating the orthotropic elastic behavior resulting from the layer-by-layer deposition process in FDM. Because printing characteristics like layer thickness, raster width, and printing speed have a big effect on the final part's anisotropy, a combined experimental-numerical framework was set up to study these effects. The method uses mechanical testing with multiple loading setups and numerical simulations to find the orthotropic elastic constants that best describe how the material behaves. This iterative approach facilitates the creation of predictive models that connect printing parameters to the actual mechanical performance of the manufactured components. Figure 4 shows how the technique works as a whole. It is set up like this:

- **Selection of FDM printing parameters:** taking into account other AM parameters, such as printing speed, raster width, and infill rate, etc.;

- **Application of a Design of Experiments (DoE):** developing a structured experimental design to examine the impact of the selected parameters;
- **Printing of specimens:** manufacturing standardized specimens in accordance with specific requirements (tensile, shear tests);
- **Conducting mechanical tests:** standardized mechanical tests are used to characterize the mechanical properties of the specimens;
- **Creation of prediction models:** to obtain mathematical models based on the process parameters.

The main goal of this research is to improve the understanding of the influence of printing parameters on the characteristics of parts manufactured by AM, as well as to develop useful methods for anticipating and improving manufacturing processes.

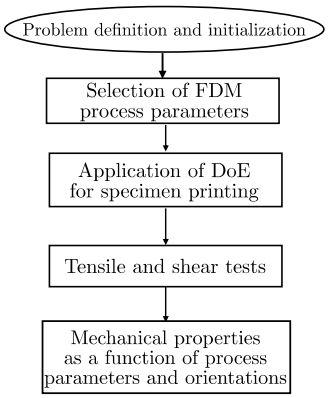

Figure 4 Methodological flowchart of the experimental approach to develop predictive models

3) Factors of the Design of Experiments

Parameters influencing mechanical properties

In this research, the FDM process parameters were selected considering their significant impact on the mechanical characteristics of the produced components, as well as the technical limitations of the equipment used. Their choice was guided by recommendations from the scientific literature and established industrial practices, with the aim of ensuring the quality and reproducibility of the manufactured samples.

According to studies conducted by Phillips[16], various FDM process parameters have a significant influence on the mechanical characteristics of manufactured parts. Taking into account these recommendations as well as the specific constraints of this study, the following parameters were selected:

- **Build orientation:** determines the alignment of the layers relative to the axes of mechanical stress. It directly influences the inter-layer strength and the overall stiffness of the part;
- **Raster width:** raster width affects the printing precision, the flow rate of extruded material, and the thickness of the deposited lines;
- **Layer thickness:** influences the surface quality, precision, and adhesion between layers. An appropriate height helps to limit porosity and ensure better material homogeneity;
- **Number of perimeters:** the peripheral contours reinforce the edges of the part and improve structural cohesion at the periphery;
- Extrusion temperature: controls the fluidity of the extruded material. A good compromise allows for good fusion between layers without degrading the polymer;
- **Printing speed:** affects the manufacturing time and the quality of the deposits. A stable speed contributes to a homogeneous and precise print;
- **Infill pattern and density:** the infill pattern (e.g., rectilinear, hexagonal, or gyroid) determines the internal structure of the part, while the infill density controls the proportion of material deposited inside. These parameters influence the lightness, stiffness, and overall strength of the part.

These choices were made to ensure reliable, reproducible, and well-controlled printing conditions for the subsequent experimental study.

4) Parameters selected as factors for the design

In order to propose a new Topology Optimization (TO) method that integrates FDM printing parameters, three main parameters were studied and carefully selected (Layer thickness (t), Raster width (w), and printing speed (S))

III. Experimental Methodology

1) Choice of the Design of Experiments

Designs of experiments are procedures that allow for the optimal organization[17] of experiments conducted within a research method, or particularly in the study of an industrial process or product. The design of experiments can be a tool to model the relationship linking a response y to a set of factors x_i.

One should consider designs of experiments if interested in a function of the type:

$$y = f(x_i) \quad (8)$$

With:

y: quantity of interest to the experimenter; this quantity is called the response or the quantity of interest;

x_i: variables on which the experimenter can act; these variables can be continuous or discontinuous; they are called factors;

f : mathematical function that best explains the variations of the response according to the different values given to the x_i[18];

It is necessary to list all factors likely to influence the studied phenomenon without excluding any. It has been shown that the number of factors is not a constraint for conducting experiments, and that the use of fractional designs can reduce the number of experiments required. It is necessary to overcome the bad habits acquired through the traditional "one factor at a time" approach and to comprehensively examine all factors likely to influence the responses. It is necessary to abandon dead ends and restrictive assumptions[17].

The selection of one or more responses is of crucial importance. The entire analysis and all conclusions are based on this decision. A response that is inadequate for the problem risks compromising the validity of the experiment or leading to irrelevant conclusions. The chosen response must be clear and unambiguous to accurately answer the question posed. This choice is not as trivial as it might seem, which is sometimes the main obstacle one faces. For example, we have devoted considerable time and exceptional creativity to develop a precise method for measuring the effervescence of mineral water or assessing the stress level of air traffic controllers[17].

When studying a factor x_i, such as temperature for example, it is not significantly modified. A lower value and an upper value are always defined according to the requirements of the study. The variations of the factor are thus constrained by two limits. The experimenter retains the lower bound as the "low level" and the upper bound as the "high level". It is common to identify the low level of a factor with a minus sign (-) and its high level with a plus sign (+)[18].

Designs of experiments allow obtaining a maximum of information by carrying out a minimum number of tests. For this, it is necessary to know the basic mathematical principles to use them well and to adopt a methodical approach[18].

The selected printing parameters were defined based on material supplier recommendations and commonly adopted values reported in the literature for FDM-processed PLA. An extrusion temperature of 200 °C was chosen to ensure sufficient melt flow and interlayer bonding without inducing thermal degradation. A build plate temperature of 60 °C, close to the glass transition temperature of PLA, was adopted to improve first-layer adhesion and reduce warping. These conditions represent a well-established compromise between print quality, dimensional stability, and mechanical performance in standard FDM environments.

Presentation of the Box-Behnken Design

The experimental approach derived from Box-Behnken is crucial for the study of complex phenomena affected by several quantitative factors, thus allowing for an optimal exploration of the main effects and interactions between variables.

The experimental design was developed to establish several levels of study in order to evaluate quadratic effects and to integrate central points to adjust the variance and serve the model, which makes it a tool for supporting non-linearities and interactions between variables[19].

In this work, we discuss the factors affecting the mechanical performance of printed parts such as layer thickness, raster width (nozzle diameter), and printing speed. Tests were organized according to a DoE with three levels for each parameter, making the tests precise and reliable. For each factor, a DoE was carried out and allowed for interaction studies and the highlighting of non-linear effects. Finally, in order to better model the phenomena influencing the test results and to be able to accurately predict the performance of the manufactured parts, intermediate tests were added.

The following Table 1 presents the studied factors as well as the levels chosen for each:

Table 1 Levels of the parameters for the design of experiments

Parameter	Symbol	Level 1	Level 2	Level 3
Width (mm)	w	0.3	0.4	0.5
Speed (mm/s)	S	50	65	80
Thickness (mm)	t	0.08	0.14	0.20

2) Design Construction

The Box-Behnken method was used with Minitab software to organize the experimental tests. This experimental design was chosen for its ability to model quadratic effects while reducing the total number of required tests.

The Box-Behnken design produced 13 combinations of tests, considering the three study factors (layer thickness, raster width (nozzle diameter), and printing speed), each at three

levels. While maximizing experimental resources, this method allows for a rapid examination of the individual influence of the parameters as well as their interactions.

The following Table 2 illustrates the combinations obtained for the different tests:

Table 2 Table of test parameters

Order	w (mm)	T (mm)	S (mm/s)
1	0.3	0.08	65
2	0.5	0.08	65
3	0.3	0.20	65
4	0.5	0.20	65
5	0.3	0.14	50
6	0.5	0.14	50
7	0.3	0.14	80
8	0.5	0.14	80
9	0.4	0.08	50
10	0.4	0.20	50
11	0.4	0.08	80
12	0.4	0.20	80
13	0.4	0.14	65

3) Printing of the Samples

a) Description of Specimen Standards

To comprehensively evaluate the influence of printing parameters on mechanical properties, each combination from the Box-Behnken design of experiments was used to manufacture two types of specimens:

- **Specimens for tensile tests**
  The tensile tests will be carried out in accordance with the **ISO 527-2** standard[20]. Although this standard was initially developed for conventional polymers, it is perfectly applicable to materials manufactured by FDM 3D printing. In the absence of a specific standard dedicated to printed parts, the use of ISO 527-2 remains justified, as confirmed by the study of Spoerk et al[16]. The dimensions of the type 1BA specimen, specifically dedicated to tensile tests according to this standard, are illustrated in detail in Figure 5.

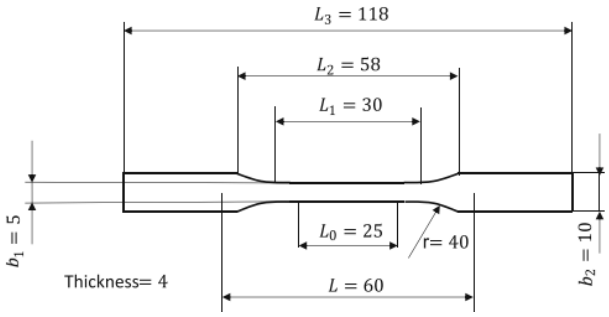

Figure 5 Specimen according to ISO 527-2 type 1BA "tensile strength" test sample (dimensions in mm)

- **specimens for shear tests**
  For this test, a cylindrical specimen with a **diameter** of 6 mm and a **length** of 60 mm was used. Its geometry is inspired by the **ASTM E8 – Method C** standard, which defines the standard dimensions of specimens for tensile tests, even for a shear test protocol.

b) Experimental Conditions for Printing

To account for the effect of the build orientation, each model was printed in three main directions, printing along the *X'*-axis, *Y'*-axis, and *Z'*-axis.

The mechanical specimens were produced by FDM using a Creality Ender 3-V2 printer (Figure 6) and PLA (polylactic acid) filament.

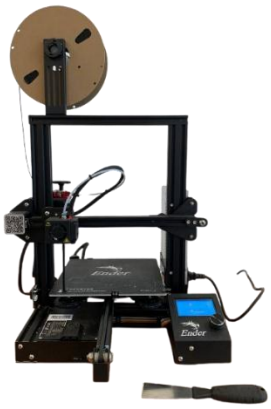

Figure 6 Creality Ender 3-V2

Several printing parameters were intentionally maintained constant throughout the manufacturing process to ensure experimental reproducibility. These parameters were chosen to ensure optimal print quality while minimizing sources of variability:

- Material: PLA (diameter 1.75 mm). PLA is a thermoplastic polymer widely used in 3D printing for its good mechanical properties;
- Extrusion temperature: 200\degree C. This temperature is in the optimal range recommended for PLA;
- Bed temperature: 60\degree C. Maintaining this temperature improves the adhesion of the first layer to the bed, thus reducing the risk of detachment or warping;
- Infill density: 100\%. A full infill was chosen to simulate a nearly dense and homogeneous material to minimize internal voids. This allows obtaining mechanical results representative of the solid material and limiting the influence of porosity on the measured properties;
- Infill pattern: rectilinear. The rectilinear pattern promotes a uniform distribution of mechanical loads during tests, while facilitating control of the printing path;
- Number of perimeters: 1 perimeter. A single peripheral contour was defined to ensure continuity with the infill area and to maintain the nominal dimensions of the specimens.

All prints were made from standardized digital models exported in STL format, then sliced using dedicated software respecting the mentioned parameters. To preserve the integrity of the parts printed directly to the final size, no machining or post-processing operations were performed.

Each specimen was rigorously identified and stored to ensure proper tracking during the mechanical testing campaigns.

The printing of specimens is shown in Figure 7.

Figure 7 Printing of a specimen along the Z-axis

4) Tensile Tests

The tensile tests were carried out in accordance with the ISO 527-2 standard. Figure 8(a), (b) and (c) show printing along the *X'*-axis, *Y*'-axis and *Z'*-axis respectively.

(a) (b) (c)

Figure 8 Tensile test specimens

c) Equipment and Test Conditions

The tests were carried out using a MTS universal testing machine Figure 9, equipped with a 10 KN load cell suitable for the low stresses characteristic of polymer materials.

Figure 9 Tensile test

The main test conditions are:

- Specimen shape}: see Figure 5 ISO 527-2;
- Test speed: 0.25 mm/min according to ISO 527-1;
- Area for Young's modulus calculation: defined between 0.05\% and 0.25\% of deformation.

5) Shear Tests

The shear tests were carried out according to an adapted protocol based on the principles of the ASTM E8 standard (Method C)[21].

Although this standard was originally intended for tensile testing of metallic materials, its methodology was adapted here for the evaluation of the shear behavior of printed polymer materials. Figure 10 show printing along the *X'*-axis, *Y*'-axis and *Z'*-axis respectively

Figure 10 Shear test specimens

The tests were performed on the MTS universal testing machine (Figure 11), using a specific clamping device to apply a pure shear force.

Figure 11 Shear test

The main test conditions are as follows:

- Specimen shape: specimens adapted for shear tests, inspired by the geometric specifications recommended for simple shear type tests;
- Dimensions: diameter 6 mm and total length 60 mm;
- Test speed: 1 mm/min, a rate used for tensile tests to ensure consistent comparison.

IV. Results & Discussion

1) Presentation of Raw Data

The material characterization step involved exhaustive mechanical testing campaigns, specifically tensile and shear tests. These tests were conducted on meticulously 3D printed (FDM) specimens, whose manufacturing followed a rigorous Box-Behnken design of experiments.

This design allowed for the systematic exploration of the influence of three key printing parameters (w, t, and S) on the intrinsic elastic properties of the material. Table 3 and Table 4, presented below, record all the raw results from these investigations.

They detail, for each unique combination of tested printing parameters, the measured values of the longitudinal and transverse Young's moduli ($E_{X'}$, $E_{Y'}$, $E_{Z'}$) as well as the corresponding shear moduli ($G_{X'Y'}$, $G_{Y'Z'}$, $G_{X'Z'}$). This primary data, obtained experimentally, constitutes the essential foundation on which subsequent statistical analyses and, ultimately, the construction of predictive models will be based.

Table 3 Experimental results for Young's moduli

w (mm)	t (mm)	S (mm/s)	$E_{X'}$ (GPa)	$E_{Y'}$ (GPa)	$E_{Z'}$ (GPa)
0.3	0.08	65	1.57200	1.27150	0.98910
0.5	0.08	65	1.53930	1.20280	0.90009
0.3	0.20	65	1.53080	1.10270	0.86710
0.5	0.20	65	1.26180	1.03190	0.74084
0.3	0.14	50	1.50460	1.26660	0.95280
0.5	0.14	50	1.32549	1.08628	0.81850
0.3	0.14	80	1.50820	1.25501	0.92980
0.5	0.14	80	1.14060	1.04730	0.82433
0.4	0.08	50	1.40030	1.21030	0.89238
0.4	0.20	50	1.31250	1.14130	0.87275
0.4	0.08	80	1.22900	1.04700	0.79224
0.4	0.20	80	1.11550	0.98540	0.74462
0.4	0.14	65	1.33040	1.13490	0.81552

Table 4 Experimental results for shear moduli

w (mm)	t (mm)	S (mm/s)	$E_{X'}$ (GPa)	$E_{Y'}$ (GPa)	$E_{Z'}$ (GPa)
0.3	0.08	65	0.77460	0.66575	0.79560
0.5	0.08	65	0.69190	0.49595	0.58755
0.3	0.20	65	0.73535	0.48285	0.60425
0.5	0.20	65	0.56985	0.46985	0.58895
0.3	0.14	50	0.71110	0.67450	0.76325
0.5	0.14	50	0.52415	0.64145	0.69215
0.3	0.14	80	0.68925	0.58080	0.65870
0.5	0.14	80	0.47385	0.52190	0.52190
0.4	0.08	50	0.60585	0.69860	0.77530
0.4	0.20	50	0.63910	0.63530	0.70610
0.4	0.08	80	0.58185	0.63675	0.72805
0.4	0.20	80	0.30995	0.37650	0.50860
0.4	0.14	65	0.55980	0.42930	0.69095

2) Stress-Strain Curves (Tensile + Shear)

To thoroughly analyze and visually interpret the complex effects of printing parameters on the mechanical properties of FDM-manufactured parts, several types of graphical representations were used. These visual tools are essential for understanding not only the overall behavior of the material but also the nuances induced by variations in manufacturing conditions.

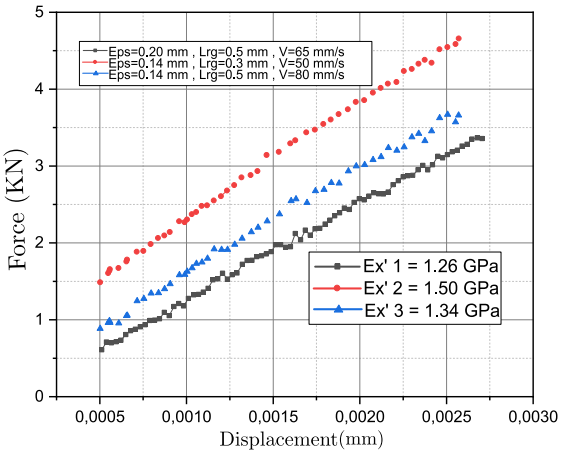

Figure 12 Force–displacement curves and elastic moduli: Effect of process parameters on EX'

Data from tensile tests systematically conducted along the three orthogonal axes (*X'*, *Y'*, and *Z'*) were utilized. These tests are fundamental because they allow for a detailed examination of the influence of key printing factors—such as raster width, layer thickness, and printing speed—on the directional mechanical characteristics of 3D components. The raw force-displacement curves, recorded during each tensile test, are the primary source of information for evaluating the Young's modulus under various parameters.

The results demonstrate a significant influence of printing orientation on the elastic stiffness of the material. Reflecting good mechanical behavior, the moduli in the X'-direction, shown in Figure 12, range from 1.26 to 1.50 GPa.

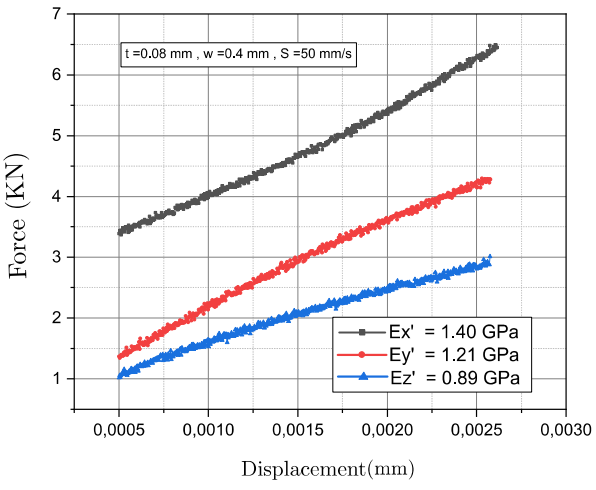

Figure 13 Force–displacement curves and elastic moduli: Comparison of orthotropic moduli for a fixed parameter set

A comparison with constant parameters, shown in Figure 13, confirms the orthotropic behavior of the material: stiffness is maximal in X', intermediate in Y', and minimal in Z'.

Ultimately, the mechanical behavior of FDM components is strongly influenced by the printing direction and associated parameters; the process's anisotropy must be taken into account in the design.

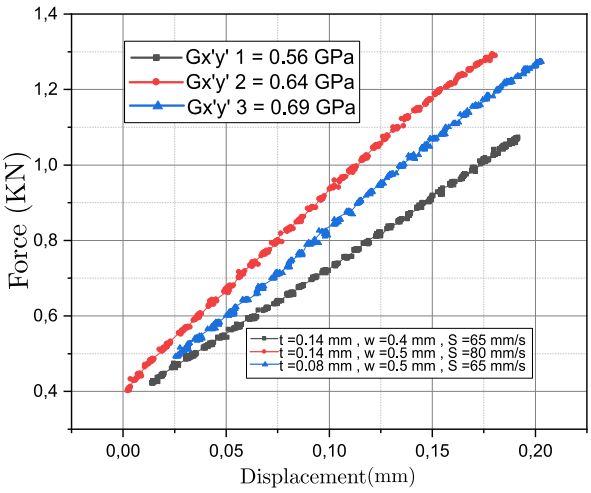

Figure 14 Force-displacement curves and shear moduli: Parameter effect on GX'Y'

Figure 14shows the shear response in the *X'Y'* plane for three printing configurations. The obtained moduli vary from 0.56 GPa to 0.69 GPa, demonstrating a marked sensitivity to manufacturing parameters.

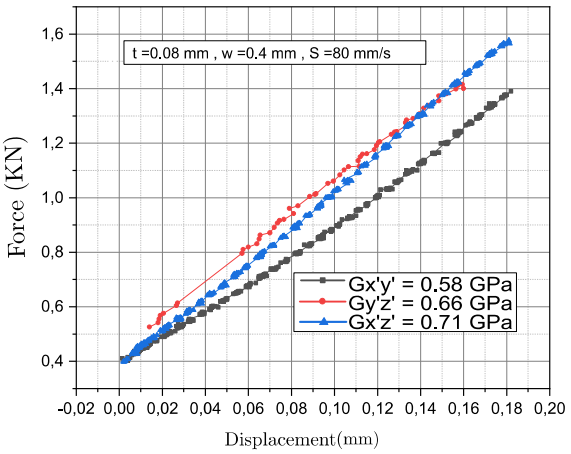

Figure 15 Force-displacement curves and shear moduli: Comparison of orthotropic shear moduli for a fixed parameter set

Figure 15 summarizes the results by directly comparing the three shear moduli for the same set of printing parameters. Anisotropy is clearly visible: $G_{X'Z'}$ = 0.71 GPa is the highest, followed by $G_{Y'Z'}$ = 0.66$ GPa, then $G_{X'Y'}$ = 0.58 GPa.

Overall, these experimental results clearly highlight the pronounced anisotropic behavior of FDM-manufactured PLA in shear, strongly influenced by the loading direction and by

printing parameters, especially the orientation of intra-layer deposition.

In the linear elastic regime, force–displacement measurements can be directly used to derive stress–strain responses through standard mechanical relationships. Specifically, the applied force is converted into stress using the nominal cross-sectional area, while the measured displacement is converted into strain using the initial gauge length of the specimen.

Since all tests were conducted within the elastic domain and under controlled boundary conditions, the resulting stress–strain curves are mechanically equivalent representations of the experimentally recorded force–displacement data. This approach is commonly adopted in experimental mechanics and does not affect the validity of the extracted elastic moduli.

The corresponding stress and strain values were calculated as follows:

Axial tests (Young's modulus):

$$\sigma = \frac{F}{A} \quad , \qquad \varepsilon = \frac{\Delta L}{L_0} \tag{9}$$

where:

- σ : axial stress (Pa)
- ε : axial strain (dimensionless)
- F : applied force (N)
- A : cross-sectional area of the specimen (m²)
- ΔL : measured elongation (m)
- L_0 : initial length of the specimen (m)

Shear tests (Shear modulus):

$$\tau = \frac{F}{2A} \quad , \qquad \gamma = \frac{\Delta D}{D_0} \tag{10}$$

where:

- τ : shear stress (Pa)
- γ : shear strain (dimensionless)
- F = applied shear force (N)
- A = shear area ($A = \pi \frac{D^2}{4}$) of the specimen (m²)
- ΔD = measured shear displacement (m)
- D_0 = initial diameter in shear (m)

The Young's modulus E and the shear modulus G were then obtained from the slope of the linear region of the stress-strain curves:

$$E = \frac{\sigma}{\varepsilon} \quad , \qquad E = \frac{\tau}{\gamma} \tag{11}$$

3) Predictive Models for Elastic Moduli

Quadratic polynomial models were established from the experimental results and the statistical analysis of the design of experiments to estimate the elastic moduli ($E_{X'}$, $E_{Y'}$, $E_{Z'}$) and shear moduli ($G_{X'Y'}$, $G_{Y'Z'}$, $G_{X'Z'}$) as a function of three printing parameters (w (mm), t (mm), and S (mm/s)).

The analysis of variance (ANOVA) allows for the evaluation of the influence of these parameters on the mechanical properties of the printed parts, by identifying the significant effects of the factors and their interactions.

a) Model for Young's Modulus $E_{X'}$

The analysis of variance (ANOVA) Table 5 indicates that the prediction model for the Young's modulus $E_{X'}$ is globally significant, with a p-value of 0.006 for the entire model. This means that the considered factors reliably explain the variation in the mechanical response.

Therefore, raster width is the dominant factor in the variation of $E_{X'}$, followed by layer thickness and printing speed. The quadratic effects and interactions enhance the quality of the model, although their contribution varies in different cases.

Table 5 Analysis of Variance Table for EX'

Source	DF	Adj SS	Adj MS	F-Value	p-Value
Model	7	0.274490	0.039213	13.35	0.006
Linear	3	0.161531	0.053844	18.33	0.004
w	1	0.089975	0.089975	30.63	0.003
t	1	0.033800	0.033800	11.51	0.019
S	1	0.037756	0.037756	12.85	0.016
Square	2	0.090118	0.045059	15.34	0.007
w^2	1	0.038249	0.038249	13.02	0.015
S^2	1	0.025149	0.025149	8.56	0.033
Interaction	2	0.022842	0.011421	3.89	0.096
w.t	1	0.013959	0.013959	4.75	0.081
w.S	1	0.008882	0.008882	3.02	0.143
Error	5	0.014686	0.002937		
Total	12	0.289176			

The resulting equation for $E_{X'}$ is as follows (results are given in GPa):

$$E_{X'} = 0.95 - 6.99w + 2.85\,t + 0.0627\,S + 11.69\,w^2 - 0.000421\,S^2 - 9.85\,w.t - 0.0314\,w.S \tag{12}$$

b) Model for Young's Modulus $E_{Y'}$

The ANOVA Table 6 shows that the prediction model for the transverse Young's modulus $E_{Y'}$ is globally significant, with a p-value of 0.008 for the complete model. This indicates that the studied parameters satisfactorily explain the variation in the mechanical response $E_{Y'}$.

Table 6 Analysis of Variance Table for EY'

Source	DF	Adj SS	Adj MS	F-Value	p-Value
Model	4	0.088574	0.022144	7.42	0.008
Linear	3	0.079525	0.026508	8.88	0.006
w	1	0.034786	0.034786	11.65	0.009
t	1	0.027648	0.027648	9.26	0.016
S	1	0.017091	0.017091	5.72	0.044
Square	1	0.009049	0.009049	3.03	0.120
w^2	1	0.009049	0.009049	3.03	0.120
Error	8	0.023887	0.002986		
Total	12	0.112462			

The resulting equation for $E_{Y'}$ is as follows (results are given in GPa):

$$E_{Y'} = 2.573 - 5\,w + 0.98\,t + 0.00308\,S + 5.42\,w^2 \quad (13)$$

c) Model for Young's Modulus $E_{Z'}$

The analysis of variance for the prediction model of $E_{Z'}$ Table 7 (vertical Young's modulus) indicates that the model is globally significant, with a p-value of 0.004. This confirms that the selected input variables satisfactorily explain the variation in the response.

Table 7 Analysis of Variance Table for EZ'

Source	DF	Adj SS	Adj MS	F-Value	tp-Value
Model	4	0.057671	0.014418	9.38	t0.004
Linear	3	0.048593	0.016198	10.54	t0.004
w	1	0.025882	0.025882	16.83	t0.003
t	1	0.015181	0.015181	9.87	t0.014
S	1	0.007530	0.007530	4.90	t0.058
Square	1	0.009078	0.009078	5.90	t0.041
w^2	1	0.009078	0.009078	5.90	t0.041
Error	8	0.012300	0.001537		
Total	12	0.069970			

The resulting equation for $E_{Z'}$ is as follows (results are given in GPa):

$$E_{Z'} = 2.155 - 4.91\,w - 0.726\,t - 0.002045\,S + 5.43\,w^2 \quad (14)$$

d) Model for Shear Modulus $G_{X'Y'}$

The prediction model for modulus $G_{X'Y'}$ is globally significant (shown in ANOVA Table 8) (F = 9.34, p = 0.008), confirming that the studied parameters satisfactorily explain the variation of $G_{X'Y'}$.

Table 8 Analysis of Variance Table for GX'Y'

Source	DF	Adj SS	Adj MS	F-Value	p-Value
Model	6	0.16931	0.028218	9.34	0.008
Linear	3	0.09551	0.031836	10.54	0.008
w	1	0.05290	0.052902	17.51	0.006
t	1	0.02000	0.019995	6.62	0.042
S	1	0.02261	0.022610	7.48	0.034
Square	2	0.05052	0.025260	8.36	0.018
w^2	1	0.02011	0.020111	6.66	0.042
S^2	1	0.01533	0.015328	5.07	0.065
Interaction	1	0.02328	0.023279	7.71	0.032
t.S	1	0.02328	0.023279	7.71	0.032
Error	6	0.01813	0.003021		
Total	12	0.18743			

The resulting equation for $G_{X'Y'}$ is as follows (results are given in GPa):

$$G_{X'Y'} = 0.466 - 7.59\,w + 0.4.68\,t + 0.0511\,S + 8.47\,w^2\ 0.000329\,S^2 - 0.0848\,t.S \quad (15)$$

e) Model for Shear Modulus $G_{Y'Z'}$

The prediction model for modulus $G_{Y'Z'}$ is highly significant (shown in ANOVA Table 9) (F = 14.97, p = 0.010), demonstrating an excellent fit to the experimental data.

Table 9 Analysis of Variance Table for GY'Z'

Source	DF	Adj SS	Adj MS	F-Value	p-Value
Model	8	0.128171	0.016021	14.97	0.010
Linear	3	0.080518	0.026839	25.08	0.005
w	1	0.009436	0.009436	8.82	0.041
t	1	0.035451	0.035451	33.13	0.005
S	1	0.035631	0.035631	33.29	0.004
Square	3	0.031809	0.010603	9.91	0.025
w^2	1	0.007846	0.007846	7.33	0.054
t^2	1	0.003789	0.003789	3.54	0.133
S^2	1	0.031169	0.031169	29.12	0.006
Interaction	2	0.015844	0.007922	7.40	0.045
w.t	1	0.006147	0.006147	5.74	0.075
t.S	1	0.009697	0.009697	9.06	0.040
Error	4	0.004281	0.001070		
Total	12	0.132452			

The resulting equation for $G_{Y'Z'}$ is as follows (results are given in GPa):

$$G_{Y'Z'} = 4.231 - 5.95\,w + 3.33\,t - 0.0643\,S + 5.86\,w^2 + 11.31\,t^2 + 0.000519\,S^2 + 6.53\,w.t - 0.0547\,t.S \quad (16)$$

f) Model for Shear Modulus $G_{X'Z'}$

The prediction model for modulus $G_{X'Z'}$ is highly significant (shown in ANOVA Table 10) (F = 11.31, p = 0.003), explaining 89.0% of the total variance (R^2= 0.076623/0.086110).

The resulting equation for $G_{X'Z'}$ is as follows (results are given in GPa):

$$G_{X'Z'} = 1.259 - 1.52\,w - 1.5\,t + 0.00247\,S + 8.03\,w.t - 0.0417\,t.S \quad (17)$$

Table 10 Analysis of Variance Table for GX'Z'

Source	DF	Adj SS	Adj MS	F-Value	p-Value
Model	5	0.076623	0.015325	11.31	0.003
Linear	3	0.061691	0.020564	15.17	0.002
w	1	0.012545	0.012545	9.26	0.019
t	1	0.028632	0.028632	21.12	0.002
speed	1	0.020513	0.020513	15.13	0.006
Interaction	2	0.014932	0.007466	5.51	0.037
w.t	1	0.009288	0.009288	6.85	0.035
t.S	1	0.005644	0.005644	4.16	0.081
Error	7	0.009488	0.001355		
Total	12	0.086110			

The robustness of the proposed regression models was evaluated using the coefficient of determination (R^2). High R^2 values were obtained for all predicted elastic properties, indicating strong agreement between experimental results and model predictions. The remaining discrepancies are primarily attributed to the intrinsic variability of the FDM process. Overall, the models provide reliable predictive capability within the investigated parameter space.

V. Conclusion

This study developed a comprehensive methodology to predict the mechanical properties of FDM printed parts. Through a Box-Behnken design of experiments, we analyzed the impact of three key parameters: raster width, layer thickness, and printing speed.

The results reveal a marked anisotropy, with longitudinal moduli ($E_{X'}$) significantly higher than transverse moduli ($E_{Z'}$), due to the limitations of interlayer adhesion. Statistical analysis allowed for the establishment of predictive models highlighting complex relationships including non-linear effects and interactions between parameters.

The generated response surfaces identify optimal combinations of parameters, offering valuable tools for optimization. These models, statistically significant ($p<0.05$) and predictive ($R^2>89\%$), open up prospects for integration into topology optimization algorithms.

In conclusion, this research provides both a fundamental understanding of the parameter-property relationships and practical tools for optimizing printed parts, while emphasizing the crucial importance of considering the inherent anisotropy of the FDM process.

Future work can further develop these methods to optimize the performance of 3D-printed materials, making AM a crucial element of contemporary engineering. Additionally, TO optimization, in conjunction with PSP relationships, can address other design constraints, such as stress and overhanging features.

References:

1. B. Sanderson, F. Diba, H. Kishawy, et A. Hosseini, « Finite element analysis of additive manufacturing of polymers using selective laser sintering », *Int. J. Adv. Manuf. Technol.*, vol. 129, nº 3-4, p. 1631-1647, nov. 2023, doi: 10.1007/s00170-023-12370-5.

2. M. Daly, M. Tarfaoui, M. Chihi, et C. Bouraoui, « FDM technology and the effect of printing parameters on the tensile strength of ABS parts », *Int. J. Adv. Manuf. Technol.*, vol. 126, nº 11-12, p. 5307-5323, juin 2023, doi: 10.1007/s00170-023-11486-y.

3. A. Bellini et S. Güçeri, « Mechanical characterization of parts fabricated using fused deposition modeling », *Rapid Prototyp. J.*, vol. 9, nº 4, p. 252-264, 2003.

4. Z. H. U. Jihong, Z. Han, W. Chuang, Z. Lu, et Y. Shangqin, « A review of topology optimization for additive manufacturing: Status and challenges », *Chin. J. Aeronaut.*, vol. 34, nº 1, p. 91-110, 2021.

5. S. Xu, J. Huang, J. Liu, et Y. Ma, « Topology optimization for FDM parts considering the hybrid deposition path pattern », *Micromachines*, vol. 11, nº 8, p. 709, 2020.

6. J. Zou et X. Xia, « Topology optimization for additive manufacturing with strength constraints considering anisotropy », *J. Comput. Des. Eng.*, vol. 10, nº 2, p. 892-904, 2023.

7. Y. Zhou, T. Nomura, et K. Saitou, « Anisotropic multicomponent topology optimization for additive manufacturing with build orientation design and stress-constrained interfaces », *J. Comput. Inf. Sci. Eng.*, vol. 21, nº 1, p. 011007, 2021.

8. J.-H. Zhu, W.-H. Zhang, et L. Xia, « Topology Optimization in Aircraft and Aerospace Structures

Design », *Arch. Comput. Methods Eng.*, vol. 23, nº 4, p. 595-622, déc. 2016, doi: 10.1007/s11831-015-9151-2.

9. J. Plocher et A. Panesar, « Review on design and structural optimisation in additive manufacturing: Towards next-generation lightweight structures », *Mater. Des.*, vol. 183, p. 108164, 2019.

10. J. Liu *et al.*, « Current and future trends in topology optimization for additive manufacturing », *Struct. Multidiscip. Optim.*, vol. 57, nº 6, p. 2457-2483, juin 2018, doi: 10.1007/s00158-018-1994-3.

11. G. Allaire, C. Dapogny, R. Estevez, A. Faure, et G. Michailidis, « Structural optimization under overhang constraints imposed by additive manufacturing technologies », *J. Comput. Phys.*, vol. 351, p. 295-328, 2017.

12. L. Cheng, J. Liu, X. Liang, et A. C. To, « Coupling lattice structure topology optimization with design-dependent feature evolution for additive manufactured heat conduction design », *Comput. Methods Appl. Mech. Eng.*, vol. 332, p. 408-439, 2018.

13. Y. Mehir, A. Benaouali, et Y. Benabid, « Integration of FDM process-structure relationship in topology optimization formulation », *Int. J. Adv. Manuf. Technol.*, vol. 136, nº 3-4, p. 1483-1499, janv. 2025, doi: 10.1007/s00170-024-14929-2.

14. E. J. Barbero, *Introduction to composite materials design*. CRC press, 2010. Consulté le: 26 octobre 2025. [En ligne]. Disponible sur: https://www.taylorfrancis.com/books/mono/10.1201/9781439894132/introduction-composite-materials-design-ever-barbero

15. D. Jiang, « Three dimensional topology optimization with orthotropic material orientation design for additive manufacturing structures. », PhD Thesis, 2017. Consulté le: 16 décembre 2025. [En ligne]. Disponible sur: https://baylor-ir.tdl.org/items/a519894b-d709-4d20-9376-7a744237f67c

16. C. Phillips, M. Kortschot, et F. Azhari, « Towards standardizing the preparation of test specimens made with material extrusion: Review of current techniques for tensile testing », *Addit. Manuf.*, vol. 58, p. 103050, 2022.

17. J. Goupy et L. Creighton, *Introduction aux plans d'expériences-3ème édition-Livre+ CD-Rom*. Hachette, 2006.

18. B. ATSAMENIA, « Etude de l'effet des paramètres de synthèse sur les propriétés des dépôts de Nickel en utilisant la méthode des plans d'expériences », 2019, Consulté le: 26 octobre 2025. [En ligne]. Disponible sur: https://dspace.univ-guelma.dz/jspui/handle/123456789/4141

19. G. E. P. Box et D. W. Behnken, « Some New Three Level Designs for the Study of Quantitative Variables », *Technometrics*, vol. 2, nº 4, p. 455-475, nov. 1960, doi: 10.1080/00401706.1960.10489912.

20. G. CCS, « Plastics–determination of tensile properties–part 2: test conditions for moulding and extrusion plastics », 2013, Consulté le: 26 octobre 2025. [En ligne]. Disponible sur: https://www.chinesestandard.net/PDF-EN/GBT1040.2-2022EN-P07P-H5544H-436703.pdf

21. I. Astm, « ASTM E8/E8M-16a: standard test methods for tension testing of metallic materials », *West Conshohocken PA USA ASTM Int.*, 2016.